UNIVERSITY OF COPENHAGEN
FACULTY OF SCIENCE

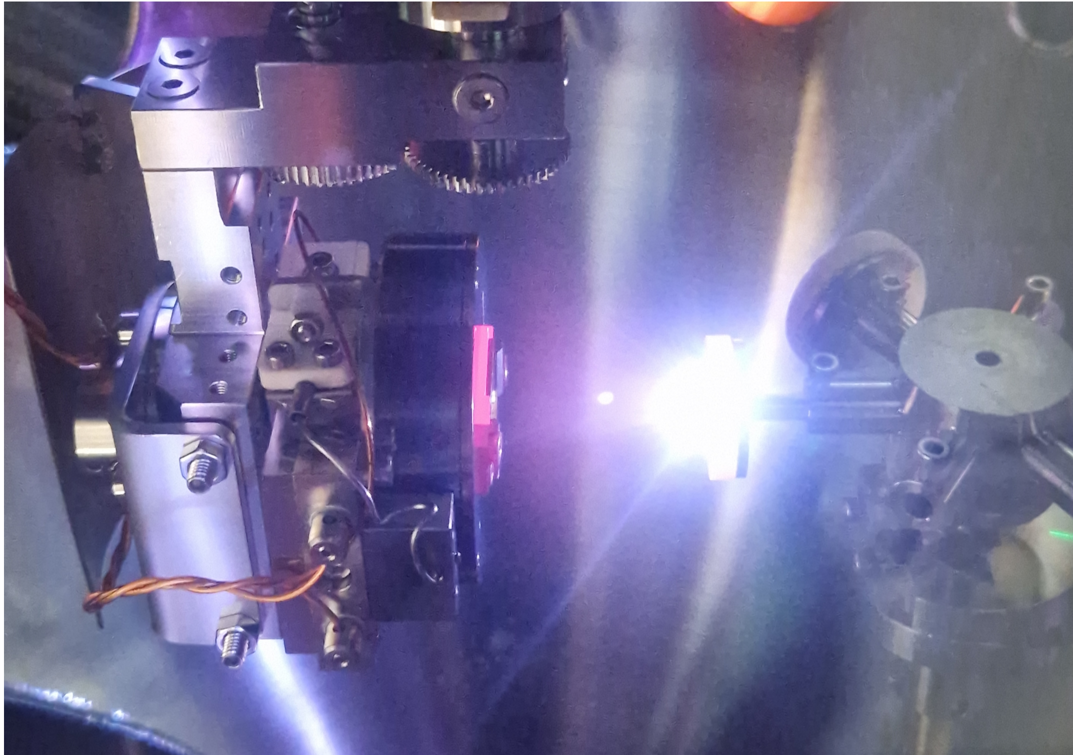

Master Thesis

A High Mobility Oxide Heterointerface

Structural and magneto-electrical characterization of γ-Al_2O_3/$SrTiO_3$ grown by Pulsed Laser Deposition

Christina Høgfeldt Christoffersen

Supervisor: Professor Jesper Nygaard and Associate Professor Felix Trier

Handed in: June 12, 2023

Abstract

The quest for high mobility interfaces has gained momentum due to the growing demand for faster and more energy-efficient devices in today's technology-driven world. To meet the needs of high-performance computing, telecommunications, and data storage, there is an urgent requirement for devices capable of operating at higher speeds and processing larger data volumes. High mobility oxide interfaces hold promise in addressing these challenges. γ-$Al_2O_3/SrTiO_3$ heterostructures has shown to exhibit carrier mobilities up towards 140,000 cm^2/Vs. which combined with a tunable carrier density can make way for new device applications. This master thesis tend to produce high mobility γ-$Al_2O_3/SrTiO_3$ heterostructures in a pursue to find the correlation between charge carrier density, optimum in mobility and growth parameters. Through structural characterization including Scanning probe microscopy techniques, x-ray crystallography and reflection high energy diffraction, the as-grown γ-$Al_2O_3/SrTiO_3$ heterostructures undergo structural analysis to gain insights on the crystallinity and strain effects. Through electrical characterization, magnetotransport is measured through the Hall effect and magnetoresistance, and sheet resistances provides an insight into the electrical conductivity and resistance of the γ-Al_2O_3 thin film. From this, it was found that the as-grown γ-$Al_2O_3/SrTiO_3$ heterostructures were epitaxially grown and of high mobility showing signs of the anomalous Hall effect, 2-band contributions to charge transfer, Extraordinary magnetoresistance and possibly Kondo effect for one sample. The findings show that a conducting interface can emerge between two insulting oxides with an electron mobility exceeding what is common amongst transition metal oxide-based heterostructures. It opens up the possibilities of controlling and manipulating the charge carrier density and electron mobility for a desired application, which may include spin electronics and ultra-sensitive bio-magnetometers.

Acknowledgements

I would like to express my deepest gratitude to my external supervisor Associate Professor Felix Trier. He has given me the necessary tools and guidance needed for this masters thesis to become a reality. He has throughout the year never hesitating in giving me advise, always being able to help explain whatever I could not understand, refer me to interesting papers or know who I should talk to for additional discussions. He has welcomed me into the world of functional oxides which has proved to be a research field that sparks my interests like nothing has done it before. I owe him and the Functional Oxides research group my greatest acknowledgements for welcoming me and making me feel like a part of the group. A special thanks is in its place to Professor Jesper Nygård for standing by as the main supervisor representing the University of Copenhagen, as this would not have an option without him. I think it is important to highlight that this project and all work presented here would not have been possible without the help, guidance and daily teamwork that I was gifted. I would therefore like to acknowledge my daily supervisor and lab partner pd.d. student Thor Hvid-Olsen. This project would not have caught my eye if not introduced by him. The many months of hard work spending all day by the PLD doing one deposition after the other would not have been the same, if doing them alone. It is true that scientific research is never only as a result of one person, but the teamwork and daily discussions as well as drawing on each others skills was how this project came to exist. I would also like to thank ph.d. and post docs. contributing with discussions on data and techniques. It is such a gift to be in an academic environment with so many diverse and intelligent people, of which I could learn how to combine my interests of structural characterization and investigating the electronic properties of a mostly interesting heterointerface.

List of Abbreviations

Acronym	Definition
TMO	Tranisition metal oxide
STO	Strontium titanate, $SrTiO_3$
GAO	Gamma alumina, γ-Al_2O_3
LAO	Lanthanum aluminate, $LaAlO_3$
BSO	Bismuth silicon oxide, $BaSnO_3$
LSO	Lanthanum scandate, $LaScO_3$
LSMO	Lanthanum strontium manganite, LSMO
2DEG	Two-dimensional electron gas
VB	Valence band
CB	Conduction band
E_F	Fermi energy
MR	Magnetoresistance
VdP	Van der Pauw
CHE	Classical Hall effect
AHE	Anomalous Hall effect
Technique	
PLD	Pulsed laser deposition
AFM	Atomic force microscopy
SEM	Scanning electron microscopy
RHEED	Reflection high-energy electron diffraction
XRD	X-ray diffraction
XRR	X-ray reflectometry
Variables	
n_s	Charge carrier density
μ	Electron mobility
σ	Conductivity
ρ	Resistivity
R_S	Combined sheet resistance
R_S^a	Sheet resistance of permutation a
R_S^b	Sheet resistance of permutation b

Contents

1 Introduction **8**

1.1 Motivation for high-mobility oxide interfaces 8

1.2 Thesis outline 9

2 General Theory **10**

2.1 Transition metal oxides and $SrTiO_3$-based electronics 10

2.1.1 $SrTiO_3$ and origin of electronic properties 11

2.1.2 $SrTiO_3$-based heterostructures 13

2.1.3 γ-Al_2O_3/ $SrTiO_3$ two-dimensional electron system 15

2.2 Charge transport at the γ-Al_2O_3/$SrTiO_3$ heterointerface 18

2.2.1 The concept of charge carrier density and electron mobility in devices 18

2.2.2 The origin of high electron mobility in γ-Al_2O_3/$SrTiO_3$ heterpstructures . . 20

3 Methods **25**

3.1 Sample preparation 26

3.1.1 Substrate treatment 26

3.1.2 Pulsed laser deposition 28

3.2 Structural characterization and growth rate determination 29

3.2.1 Scanning probe microscopy 29

3.2.2 Reflection High Energy Electron Diffraction 31

3.2.3 X-ray crystallography 35

3.3 Electrical characterization 40

3.3.1 Wire bonding 40

3.3.2 Van der Pauw method 41

3.3.3 Magnetoresistance and Hall effect 41

4 Results and discussion **46**

4.1 Pulsed laser deposition growth parameters 48

4.2 Structural characterization and growth rate estimation 51

4.2.1 Atomic force microscopy 52

4.2.2 Reflection high energy electron diffraction 56

4.2.3 X-ray crystallography 61

4.2.4 Scanning electron microscopy . . . 68
4.3 Transport properties of high mobility GAO/STO heterointerfaces . . . 70
4.3.1 The first high mobility GAO/STO heterostructure: Shin12_6 . . . 71
4.3.2 Initial resistance measurements . . . 75
4.3.3 Magnetotransport in γ-Al_2O_3/$SrTiO_3$ heterostructures . . . 80
4.3.4 Charge Carrier Densities and Hall Mobilities of GAO/STO heterostructures . 84

5 Conclusion and outlook **90**
5.1 Conclusion . . . 90
5.2 Outlook . . . 92

6 Appendices **93**
6.1 Tube furnace and annealing procedure . . . 93
6.1.1 Protocol . . . 93
6.1.2 Example of data . . . 95
6.2 Pulsed laser deposition . . . 96
6.2.1 Deposition and growth parameters . . . 96
6.2.2 Protocol . . . 98
6.3 Atomic force microscopy protocol . . . 102
6.3.1 Protocol . . . 102
6.3.2 Substrate images . . . 104
6.3.3 Sample images . . . 107
6.4 Scanning electron microscopy . . . 112
6.4.1 Protocol . . . 112
6.4.2 Images . . . 112
6.5 X-ray crystallography . . . 114
6.5.1 Protocol . . . 114
6.5.2 Supplementary data . . . 114
6.6 Electrical characterization . . . 117
6.6.1 Protocol . . . 117
6.6.2 Suplementary Hall data . . . 119
6.7 Fluence and pressure dependency supplementary data . . . 126
6.8 Maintenance . . . 128

6.8.1 Furnace room 128
6.8.2 Window polishing 128
6.8.3 Laser beam spot size management 128

References **130**

1 Introduction

1.1 Motivation for high-mobility oxide interfaces

The pursuit of high mobility interfaces has gained significant momentum in response to the ever-increasing demand for faster and more energy-efficient devices in today's technological landscape. In order to meet the requirements of high-performance computing, telecommunications, and data storage, there is a pressing need for devices that can operate at higher speeds and handle larger volumes of data. High mobility interfaces play an important role in device technology, offering substantial advantages and unlocking new possibilities across various fields. Achieving high carrier mobility in interfaces is crucial for the development of efficient electronic devices, such as transistors, sensors, and integrated circuits. These interfaces serve as fundamental components in advanced electronic systems, enabling enhanced performance, improved functionality, and reduced power consumption. Furthermore, high mobility interfaces hold the potential for greater device miniaturization and integration, a vital aspect as electronic devices continue to shrink in size.[1–4]

Traditionally, silicon-based components have formed the backbone of electronic devices, with silicon-germanium alloys being used in the first interconnected circuits developed in the 1950s.[5–8] However, the increasing demands for faster computers, smaller devices, and more energy-efficient electronics have pushed silicon-based devices to their fundamental limits. Silicon-based semiconductors are no longer capable of keeping up with the ongoing technological evolution that requires devices to decrease in size and power consumption.[9,10]

As devices continue to shrink, the presence of impurities and defects in silicon-based materials increases, leading to higher resistance and compromised device performance. Moreover, downsizing semiconductor dimensions exacerbates power consumption, resulting in increased heat dissipation. Given silicon's temperature sensitivity and relatively small band gap of 1.12 eV, downscaled devices struggle to maintain control over electricity flow and withstand extreme temperature changes.[11] Consequently, silicon-based transistors fail to meet the demand for high-performance devices that require low power consumption, temperature insensitivity, and an intrinsic wide band gap to efficiently control electronic properties and electrical flow.

Transition metal oxides (TMOs) have emerged as a promising class of materials that meet these requirements.[12–14] TMOs exhibit a range of exceptional properties, making them attractive for next-generation electronic devices. Of particular interest is the heterointerface of γ-$Al_2O_3/SrTiO_3$, which has demonstrated electron mobilities of up to 140,000 cm^2/Vs.[15] The unique electronic

characteristics of this heterointerface have sparked significant research interest and exploration.

Motivated by the exceptional properties and potential of the γ-$Al_2O_3/SrTiO_3$ oxide heterointerface, this masters thesis aimed to address the challenges of growing reproducible high-mobility γ-$Al_2O_3/SrTiO_3$ heterostructures using Pulsed Laser Deposition. The objective was to establish a reliable deposition protocol that consistently yielded high-mobility γ-$Al_2O_3/SrTiO_3$ heterostructures. In this thesis, I will present my work on growing and characterizing γ-$Al_2O_3/SrTiO_3$ oxide heterostructures, focusing on their growth parameters, structural and electrical properties. By a systematic investigation of the growth process and optimization of the deposition conditions, I aimed to establish a robust and reproducible methodology for fabricating high-mobility γ-$Al_2O_3/SrTiO_3$ interfaces. The obtained insights and findings will contribute to the understanding of interface physics and assist in the development of high-performance electronic devices.

1.2 Thesis outline

Chapter 2 introduces the necessary background theory on transition metal oxides, in particularly the γ-$Al_2O_3/SrTiO_3$ heterostructure and the origin of its remarkable high electron mobility. The chapter touch upon charge transfer and the origin of the two-dimensional electron system located at the interface of γ-$Al_2O_3/SrTiO_3$.

Chapter 3 presents and explains the methods and techniques employed in this masters project. The chapter includes a thorough examination on the sample preparation, structural and electrical characterization.

Chapter 4 presents the results obtained during the experimental work and proceeds to discuss the results in a comparative strategy.

Chapter 5 concludes the thesis, describing the central information gained as a result the experimental work. It further presents an outlook for future work in relation to the results achieved in this masters project.

2 General Theory

This section aims to establish and justify the motivation for studying γ-$Al_2O_3/SrTiO_3$ interfaces providing the necessary background by introducing novel research within the field of transition-metal oxides and oxide-based electronics.

2.1 Transition metal oxides and $SrTiO_3$-based electronics

TMOs are a class of functional oxides, characterized by their wide range of electric, magnetic, mechanical and optical properties extending from magnetoresistance similar to conventional semiconductors to multiferroicity and high-temperature superconductivity.[12,14,16,17] TMOs consist of one or more transition metal cations (such as Al, Fe, Cu, Sr etc.) combined with oxygen anions, and may show intrinsic insulating properties in the bulk.[17] Remarkable electronic and magnetic properties arise when TMO materials are combined into so-called heterostructures where the TMO composition changes along e.g. the vertical crystal orientation, allowing for a conducting interface to emerge between, what appear to be, two intrinsic insulating materials.[18] This enhancement of aforementioned physical properties has been found for many TMO heterostructures such as $LaAlO_3/SrTiO_3$ (LAO/STO)[19–21] and $BaSnO_3/LaScO_3$ (BSO/LSO)[22] to mention a few. A very popular platform for thin film growth is Strontium Titanate, $SrTiO_3$, due to its high compatibility with other functional oxides as well as its stable nature in the bulk.[23–26] While STO is by far one of the most popular substrates to use in oxide heterostructures, LAO/STO is the most intensively-studied oxide heterostructure since its discovery in 2004 by Ohtomo and Hwang.[27] Here Ohtomo and Hwang found that when growing $LaAlO_3$ epitaxially on $SrTiO_3$ a two-dimensional electron-gas emerged at the interface between the two oxides, which was a remarkable finding due to the intrinsic insulating nature of both oxides.

The wide range of electronic properties found in TMOs and TMO-based heterostructures have been proved to be the result of partially filled d-orbitals, that upon thin film growth or by applying strain, will be occupied by free electrons causing enhanced conductivity and increased electron mobility.[13,28] The origins of conducting properties in $SrTiO_3$-based heterostructures will be further described in the subsequent section.

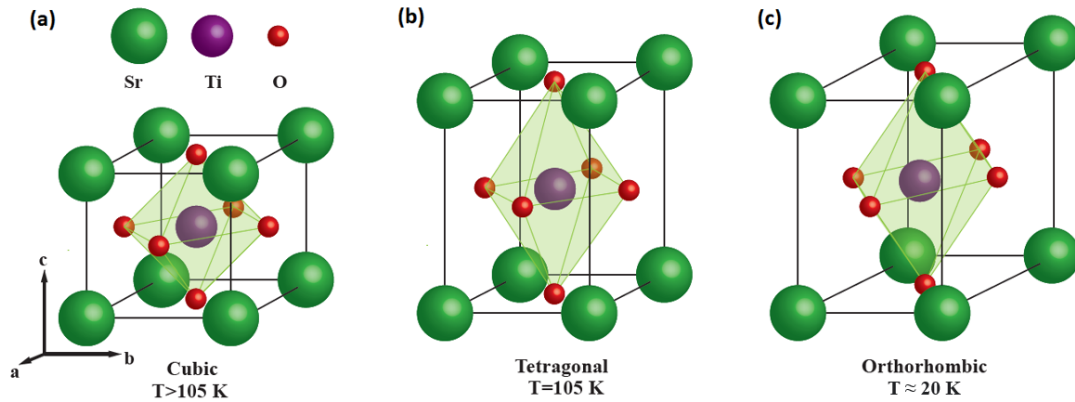

Figure 2.1: $SrTiO_3$ perovskite crystal structure. a) The cubic structure of the STO unit cell as it is at room temperature (above 105K) b) At T≈105K the unit cell of STO is elongated in the [001] direction, taking the tetragonal shape. c) At T≈20K the unit cell of STO is elongated even further in the [100] direction, giving it the shape of an orthorombic. Adapted from the master thesis of Rasmus T. Dahm and Ricci Erlandsen.[32]

2.1.1 $SrTiO_3$ and origin of electronic properties

Strontium titanate, $SrTiO_3$ (STO), was first discovered in the 1950's where it was synthesized and thought to only exist as an artificial material until its natural counterpart, tausonite, was found in Siberia in 1982. The oxide has since then been used as a substitute for diamond in precision optics and advanced ceramics due to its strength, insulating nature and optically transparent properties, along with increasingly being of interest in the development of new electronic components.[29,30]

STO belongs to the class of perovskites. Its crystal structure is characterized by the cubic arrangement of atoms with the general chemical formula ABO_3.[24] Figure 2.1a illustrates the perovskite crystal structure of STO with Sr (A) cations occupying the corners of the cubic lattice and Ti (B) cations occupying the center of the lattice, while oxygen anions occupy the face centers of the lattice. Each Ti^{4+} ion is bonded to 6 oxygen which form the TiO_6 octahedra characteristic for Ti-based perovskites. Furthermore, STO has, as typical for TMOs, strong cation-oxygen ionic bonds leading to the high chemical and thermal stability displayed by the material as it can endure strong acid treatments and high temperatures well exceeding 1000°C.[31]

STO is a well-known dielectric featuring a high dielectric constant ranging from 300 at room temperature to above 20.000 below 10K at static field.[33] A dielectric is an insulator that, through applying an electric field, can be polarized thereby alternating the electric properties of the material.

The dielectric constant, also referred to as the relative permittivity, is a measure of a material's ability to store electrical energy in an electric field, as compared to vacuum. In STO, the increase in relative permittivity observed with decreasing temperature originates from crystal phase transitions as illustrated in Figure 2.1.[23,34] At room temperature, the STO unit cell has the familiar cubic perovskite structure as first presented in Figure 2.1a. As STO is cooled down to 105K, the cube is elongated in either the [001], [010] or [100] crystallographic direction resulting in a cubic-to-tetragonal phase transition as illustrated in Figure 2.1b. When the cooling temperature approach $\sim$ 20K, STO becomes a quantum paraelectric due to the displacement of titanium ions relative to the oxygen ions giving the orthorombic shape illustrated in Figure 2.1c. The large enhancement of the dielectric constant at temperatures towards 2K occurs as STO is on the verge of becoming ferroelectric (also sometimes referred to as an insipid ferroelectric), but due to quantum oscillations this ferroelectric transition is prevented.[35,36]

The aforementioned high dielectric constant in STO-based heterostructures leads to electron mobility surpassing 20,000 cm^2/Vs at low temperatures. This enhanced mobility can be attributed to effective charge screening and has even been observed to reach as high as 120,000 cm^2/Vs in a few instances.[37,38] The correlation between dielectric constant and electron mobility is further elaborated in section 2.2.2. The high mobility found in STO is due to the electronic structure of the perovskite, particularly the vacant d-orbitals located on the titanium ion. Partially filled d-orbitals is another common feature in TMOs and is where the many conductive properties arise from.[28] Figure 2.2 illustrate the atomic band splitting experienced by the titanium ion inside the oxygen octahedron.

Figure 2.2a shows the fivefold-degenerate d-orbitals of the titanium atom. When placed in the oxygen octahedron, the degeneracy is lifted which splits the energy levels into a high energy doublet, the e_{g} states, and a low-energy triplet, the $t_{2\mathrm{g}}$ states. This splitting of energy levels is known as the crystal field effect.[39] The $t_{2\mathrm{g}}$ states remain near the Fermi level and are composed of the d_{XY}, d_{XZ} and d_{YZ} orbitals. These orbitals are identical to the ones found on neighboring titanium atoms and will couple through the p-orbitals of the oxygen atoms that lie in between. The coupling enables hopping between in plane orbitals. This means that for the d_{XY} orbital hopping is much stronger along the X and Y directions compared to the Z direction as illustrated in Figure 2.2b. This results in a lower effective mass along the X and Y direction and lead to a non-spherical Fermi surface along the k_{Z} direction, which is shown in Figure 2.2c.[28,40,41]

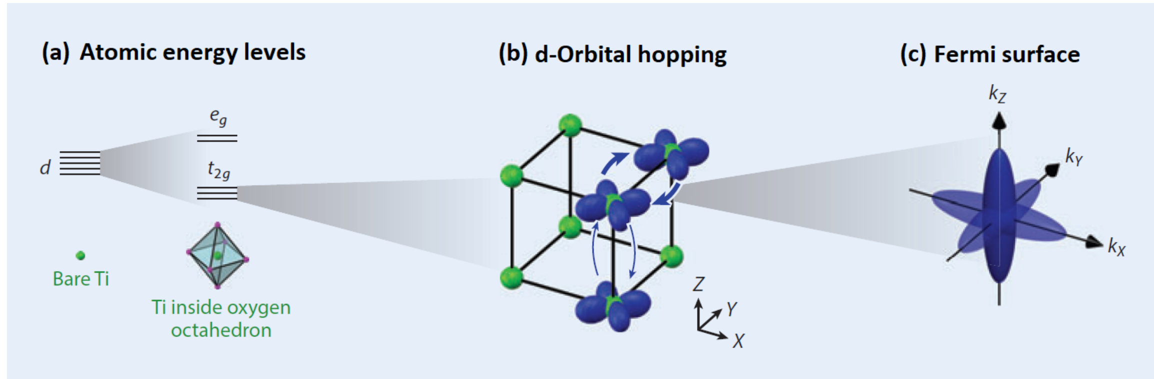

Figure 2.2: Illustration of the electronic structure of $SrTiO_3$. a) The band splitting of the fivefold-degenerate 3d-orbitals happens as a consequence of the crystal field splitting. The degeneracy of the titanium ion is lifted when placed in the oxygen octahedron resulting in a splitting of energy bands into the e_g and t_{2g} states. b) This enables hopping between the in plane d-orbitals. c) The resulting low effective mass along the X and Y direction results in the electronic band structure near the Fermi level to be more strongly curved in the Z direction. This leads to a non-spherical (cigar shaped) Fermi surface along the k_Z direction. Adapted from Sulpizio et al.[28]

The crystal field splitting of the Ti 3d-orbitals enables the t_{2g} d_{XY} orbital to be lowered such that it is favorable for charge carriers, free electrons, to occupy this state. To summarize, the lifting of the degeneracy of the Ti 3d orbital is directly associated with the structural transformations of STO as it transitions from a cubic to tetragonal and then to orthorhombic symmetry when the temperature decreases. This connection establishes a link between the breaking of crystal symmetry and the electronic structure of STO.

2.1.2 $SrTiO_3$-based heterostructures

Lanthanum aluminate, $LaAlO_3$ (LAO), is an intrinsic insulating perovskite oxide with similar structural characteristics as STO. With a lattice mismatch of 3%, epitaxial growth of LAO on STO is relatively easily achieved. The pioneering LAO/STO conductive interface discovered by Othomo and Hwang was an exciting finding with its high electron mobility measuring 10,000 cm^2/Vs and afterwards proved to be highly multifunctional. In 2010 Caviglia et al.[42] found the electron mobility in the LAO/STO 2DEG to exceed 6000 cm^2/Vs and was already in 2013 increased to 20,000 cm^2/Vs by Irwin et al.[43] when c-AFM lithography was used to write a nanoscale device, a nanowire, at the interface between LAO and STO. Figure 2.3 illustrates the crystal structure of the LAO/STO heterostructure. Both oxides have similar crystal structures and lattice parameters (3.79Å for LAO, 3.905Å for STO), allowing them to form a high quality interface which with a small lattice mismatch

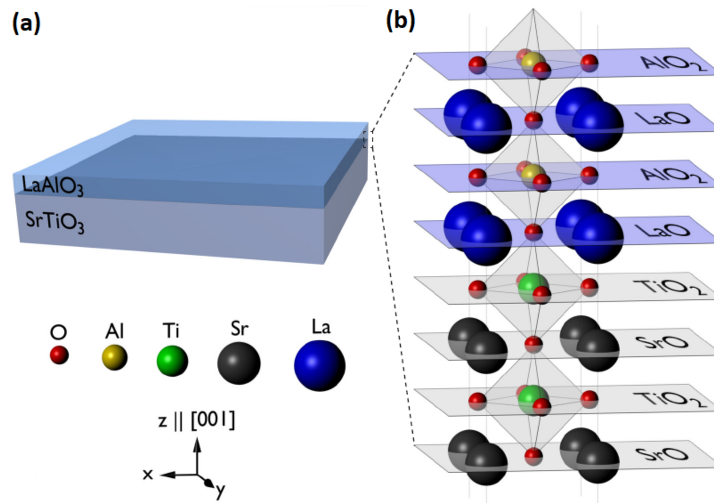

Figure 2.3: Illustration of the $LaAlO_3/SrTiO_3$ heterostructure. a) The typical LAO/STO heterostructure involves depositing a thin film of LAO onto a substrate of STO, with both materials adopting the perovskite structure in their cubic phase. b) Perovskites can be conceptualized as alternating planes of AO and BO2 along the [001] direction. In the case of LAO and STO, this translates to LaO and AlO_2, and SrO and TiO_2, respectively. Adapted from the Ph.d. thesis of F. Trier.[44]

allows for the emergence of a 2DEG.

At present, the origins of the conductive interface cannot be fully explained by one single mechanism but has been suggestively assigned, through experimental observations, to three main mechanisms: Oxygen vacancies, polar discontinuity and Polarity-induced defect formation.[45–48]

The first mechanism that can give rise to conductivity is inducing oxygen vacancies. Oxygen have a strong attraction for electrons from neighbouring atoms due to its intrinsic high electronegativity. This results in an oxidation state of O^{2-}. When a neutral oxygen is removed from STO, leaving behind an oxygen vacancy, the excess electrons can either localize around neighboring titanium ions or contribute to conductivity by delocalizing over the titanium 3d conduction band. Oxygen vacancies can be induced in STO by annealing in vacuum at high temperatures, thereby inducing conductivity as it transform STO from being an insulator to become 3D bulk conductive hence a metallic conductor. In the case of LAO/STO, and in fact also GAO/STO as well as other heterostructures where STO is combined with another TMO, low oxygen background pressure (<1.00E-04 mbar) combined with high deposition temperatures above 500°C can lead to the formation of oxygen vacancies in STO, either due to vacuum heat-treatment alone or due to the deposition of the as mentioned TMO.[15,26,48–51]

The second mechanism mentioned that may induce conductivity is polar discontinuity. Polar discontinuity refers to a mismatch in the polarization across the interface between two materials. This can occur when two materials with different crystal structures and/or lattice parameters are brought into contact with each other. This is the case for LAO/STO where STO have no net charge while the planes in LAO have an alternating charge density of ± 1 elementary charge per surface unit cell. This mismatch leads to a built-in electric field at the interface and can result in the formation of a 2DEG, if the net charge is not balanced out. The built-up of a electric field results in a continuously increasing electrostatic potential which increases the energy of the electrons of LAO, in the case of LAO/STO. This cause an electron transfer to STO when the electrons occupy electronic states of higher energy than the STO conduction band. Note that electron donation from LAO is thickness depended and is only expected when the thickness exceeds a critical value consistent with experimental observations.[48]

The final mechanism found to induce conductivity is polarity-induced defect formation. This mechanism is based on oxygen vacancies and includes the critical thickness mentioned in the latter mechanism. The polarity of LAO leads to the spontaneous creation of oxygen vacancies at the LAO surface, but only when the LAO thickness exceeds the critical value of approximately 4 unit cells. These vacancies enables the transfer of electrons to STO since the oxygen defect level is higher than the conduction band of STO. This transfer counters the potential buildup in LAO. Currently, this mechanism is considered the most widely accepted explanation for the conductivity in LAO/STO.[48]

In the search of oxide heterointerfaces where large concentrations of oxygen vacancies accumulates as a consequence of the interface composition, one such oxide heterostructure, the γ-Al_2O_3/STO heterostructure, has been found to be particularly interesting. Since the discovery of the high mobility heterointerface, the mechanism of the mobility boost has been widely discussed and studied. This Spinel/Perovskite interface and the origin of its remarkable high mobility will be described in the following sections.

2.1.3 γ-Al_2O_3/ $SrTiO_3$ two-dimensional electron system

Now that the structural characteristics and the origin of the electronic properties of STO has been introduced, the focus will be on the structural characteristics and electronic properties of γ-Al_2O_3 and the γ-Al_2O_3/STO heterointerface.

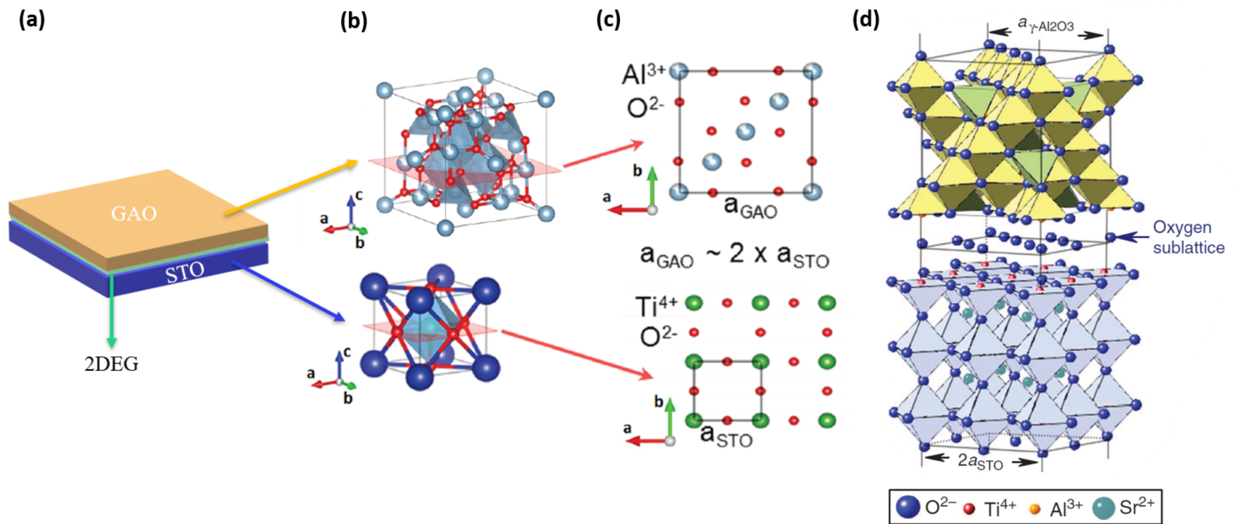

Figure 2.4: Illustration of the γ-$Al_2O_3/SrTiO_3$ heterostructure. a) A simple illustration of the GAO/STO heterostructure (GAO: orange, STO: blue) with the 2DEG (light green) generated at the interface. b) and c) Shows the three dimensional crystal structure of GAO (top) and STO (bottom) along with a cross section of the lattice planes. d) Another three dimensional illustration of the crystal structure of GAO/STO showing the formation of the oxygen superlattice. Figures adapted from Chikina et al.[15] and Mardegan et al.[52]

As stated in previous sections, multifunctional oxide devices differ from semiconductors by their strongly correlated electrons and partly filled d-orbitals. They require a large electron mobility for the mean free path of the system to become sizable with respect to the typical dimensions of a quantum device. In 2013, Chen et al. found the γ-Al_2O_3/STO heterostructure to exhibit an electron mobility up to 140,000 cm^2/Vs.[15] Comparing this to the typical LAO/STO heterostructures that may exhibit an electron mobility of 1000 cm^2/Vs,[15] the very high mobility qualifies γ-Al_2O_3/STO as the highest mobility seen in TMO structures, after ZnO-based structures.[53]

The spinel crystal structure, which gamma alumina γ-Al_2O_3 (GAO) belongs to, has the general chemical formula AB_2O_4 and consists of aluminium cations (Al^{3+}), that are partially tetrahedrally coordinated (A) and partially octahedrally coordinated (B), and oxygen anions ($O^{2}-$) arranged in a cubic close-packed lattice. The spinel crystal structure typically comprises stacked layers of tetrahedrally and octahedrally coordinated aluminum ions along the z-direction, forming 8 alternating layers. Consequently, the complete spinel unit cell consists of 8 tetrahedrally coordinated aluminum ions, 16 octahedrally coordinated aluminum ions, and 32 oxygen ions. However, the actual GAO unit cell is slightly more intricate as it also incorporates aluminum vacancies to maintain charge

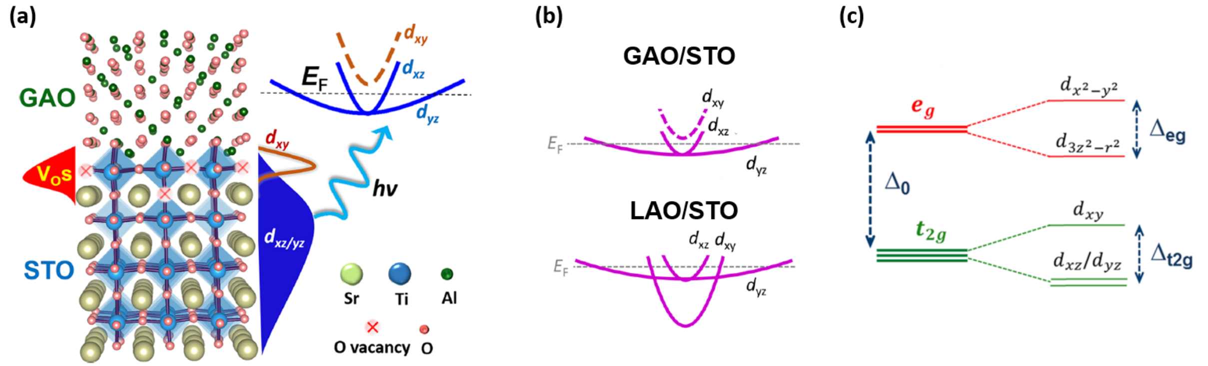

Figure 2.5: The crystal structure and band splitting of epitaxially grown γ-Al_2O_3 on $SrTiO_3$. a) The crystal structure of GAO/STO as presented by Chikina et al. showing oxygen vacancies at the interface and the band splitting of the 3d orbitalt. b) The band order for GAO/STO and LAO/STO follows two separate band orders. c) The band diagram of GAO/STO showing the splitting of the t_{2g} into d_{XY} and d_{XZ}/d_{YZ}. Figures adapted from Chikina et al.[57] and Mardegan et al.[52]

neutrality.[54,55]

Figure 2.4a-d illustrates the GAO/STO heterostructure, the crystal structures and lattice planes of GAO and STO, respectively. The lattice planes of GAO and STO, illustrated in Figure 2.4c, emphasize the difference between the spinel and perovskite crystal structure. Despite the structural differences between spinels and perovskites, the lattice mismatch between GAO and STO is only $\sim 1\%$ and can be attributed to the GAO lattice parameter ($a_{\text{GAO}} \sim 7.911$) being almost twice as large as the STO lattice parameter ($a_{\text{STO}} \sim 3.905$). This favors the emergence of an oxygen sublattice, as highlighted in Figure 2.4d.[52] The oxygen sublattice at the Spinel/Perovskite interface emerge when the two oxides are combined and additionally facilitates the favorable epitaxial growth of GAO on STO, despite their different crystal structures.[56] Figure 2.4a is a simple illustration of a GAO/STO structure in which the two-dimensional electron gas (2DEG) is generated at the interface. The origin of the Spinel/Perovskite 2DEG and the high electron mobility will be further discussed in section 2.2.2.

In section 2.1.1, the fivefold-degenerate d-orbitals of STO was described. Here Figure 2.2a showed the splitting of e_g and t_{2g} states that due to the crystal field splitting lower the t_{2g} d_{XY} orbital in energy such that it becomes more accessible for charge carriers to occupy. This means that the band order follows $d_{XY} < d_{XZ}/d_{YZ}$ and is universal across a wide range of systems based on TiO_2 terminated STO. This is not the case for GAO/STO where the band order has been described as an anomalous band order that follows $d_{XY} > d_{XZ}/d_{YZ}$ as shown in Figure 2.5a-c.[48,52,57] Similarly to

the crystal field induced band splitting seen in STO (and showed in Figure 2.2a), the 3d-orbital splits into a high energy doublet, the e_g states, and a low energy triplet, the t_{2g} states. Figure 2.4b shows the difference between the band splitting in LAO/STO and GAO/STO. The Fermi energy (E_F) is marked with a dashed line. In the case of LAO/STO are all bands, d_{XY}, d_{XZ} and d_{YZ}, below E_F with d_{XY} being lowest in energy and therefore the band with highest accessibility for charge carriers. In the case of GAO/STO are only two out of three bands, d_{XZ} and d_{YZ}, below E_F. However, this shifting of the d_{XY} state above the d_{XZ}/d_{YZ} ones results in a depopulation of the d_{XY} state and thus are the charge carriers solely populating the d_{XZ}/d_{YZ} states.

Chikina et al[57] used resonant soft-X-ray angle-resolved photoemission (ARPES) to study the fundamental physics behind the band-order anomaly and its connection with the high electron mobility seen in GAO/STO. Here they revealed that the band-order anomaly shifts the overall electron density away from the STO top layer, thereby promoting the spatial separation of electrons and donors resulting in a mobility boost. Figure 2.5a is the scheme presented by Chikinia et al. illustrating the GAO/STO interface probed with ARPES and show the spatial separation of the oxygen vacancies from the 2DEG to boost electron mobility. In subsequent sections will the concept of electron mobility and charge carriers be discussed, together with a further discussion of the origin of the high mobility in GAO/STO and the emergence of the 2DEG.

2.2 Charge transport at the γ-$Al_2O_3/SrTiO_3$ heterointerface

2.2.1 The concept of charge carrier density and electron mobility in devices

The performance of electrical devices is strongly influenced by two key properties: the charge carrier density and the electron mobility.[58] The charge carrier density (n) refers to the concentration of charge carriers, usually electrons or holes, that are free to move and contribute to electrical conductivity within a material. By increasing the concentration of either electrons or holes, the electrical conductivity of the material can be enhanced, in some cases leading to improved device performance. The electron mobility (μ) is a fundamental physical property that describes the speed with which electrons can move through the material when subjected to an electric field. The ability of electrons to move freely through the material is a critical factor in determining the performance of a device. For mobility optimization of the γ-$Al_2O_3/SrTiO_3$ 2DEG, the challenging aspect lies in finding the optimal point at which the charge carrier concentration is maximizing the highest possible electron mobility. Such an optimum is achievable at the 2D charge carrier densities, just

before the $SrTiO_3$ sample turns 3D conducting.[38] Both properties can be controlled and enhanced by careful control of growth parameters and subsequently, further enhanced by applying an external electric field to the device.

Due to the quantum mechanical nature of electrons, accurately simulating conduction (i.e. movement of electrons in a solid) would involve accounting for all interactions between positive ion cores and electrons as well as all electron-electron interactions. Despite advanced models, this complexity makes it impractical to model materials at a macroscopic scale. The Drude model reduces complexity by employing classical mechanics and through several basic key assumptions treats the solid as a fixed array of nuclei surrounded by a "sea" of unbound electrons.[38,58,59] The assumptions are as following:

- The electrons follow the independent electron approximation: electrons in metals behave much like particles in an ideal gas excluding Coulomb interactions and collisions between particles.
- The electrons do not experience coulombic interactions with ions but can still collide with the ions as well as change direction and velocity due to collisions.
- The collisions between electrons and ions result in the electrons reaching thermal equilibrium.
- And lastly, the mean free time (i.e. scattering time τ) between collisions is independent of the velocity and position of the electron. The mean free time is the average time between collisions.

Therefore according to Drude theory, when the oxide material is subjected to an electric field it causes the acceleration of charge carriers. However, this acceleration is impeded by elastic or inelastic scattering events, resulting in the charge carriers traveling with an average drift velocity. The relation between drift velocity, electric field and mobility is given by

$$v_d = \frac{e\,\tau}{m_e} E \tag{2.1}$$

and shows that the drift velocity increases linearly with the applied field. Here v_d is drift velocity, τ is mean time between scattering events, e is the elementary charge, m_e is the electron mass in free space and E is the electric field.

Going back to the definition of electron mobility, the constant in front of the electric field in eq. 2.1 is in fact the drift mobility i.e. the electron mobility. When studying the electronic transport

and optical properties of oxides, the goal is to gain insight into the eigenfunction and total energy of the electrons in the material. This information can be achieved through the effective mass approximation. In this method, electrons are treated as free particles, but with a modified mass, allowing for a better understanding of their behavior in the investigated material. Therefore, it is beneficial to use this new modified mass, the effective mass, instead of the electron mass.

$$\mu_d = \frac{e\,\tau}{m*} \tag{2.2}$$

where μ_d is the drift mobility and m* is the effective mass. It should be noted, however, that here τ is assumed to be independent of field.

To reiterate, the mean time between scattering events (τ) is directly related to the processes of which scattering events occur, i.e. lattice vibrations, crystal imperfections, and impurities to name a few. Additionally, is the mobility directly linked to the current density and the conductivity through Ohm's law.

$$J \;=\; \sigma\, E \tag{2.3}$$

and

$$\sigma \;=\; e\, n\, \mu_d \tag{2.4}$$

where J is the current density, σ is the material conductivity and n is the charge carrier density. This is, of course, to be expected and shows that the conductivity of a material is dependent of both the electron mobility and the charge carrier density. The electron mobility is hence a measure of how fast electrons drift when driven by an electric field. If the electrons are not highly scattered, meaning that the time between scattering events is long, then by eq. 2.2, the mobility will be large. Hence, the electrons will be highly mobile and can contribute to a high conductivity. However, as seen in eq. 2.4 is the conductivity just as dependent on the concentration of charge carriers and thus must both variables be carefully controlled if one wish to gain highly conducting materials.

2.2.2 The origin of high electron mobility in γ-$Al_2O_3/SrTiO_3$ heterpstructures

Now that the relationship between electron mobility and charge carrier density has been established, it is time to explore the origin of the high electron mobility found in γ-$Al_2O_3/SrTiO_3$ heterostructures.

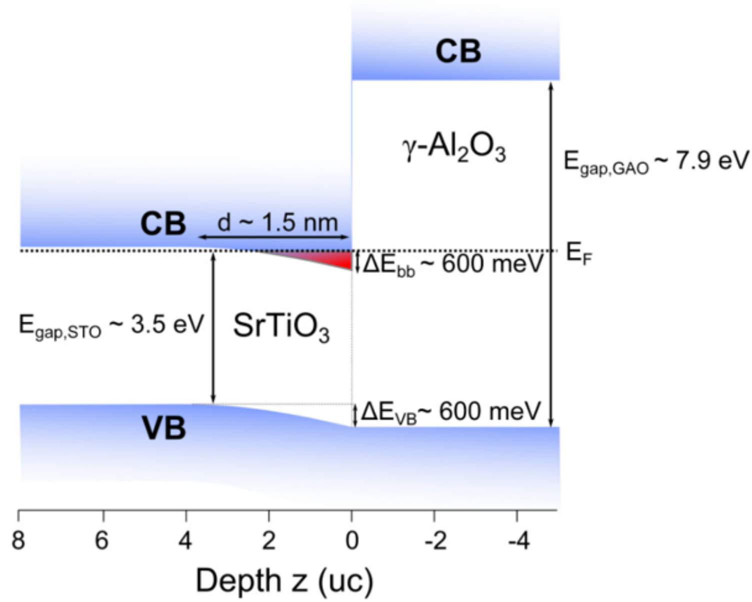

Figure 2.6: Band diagram of γ-Al_2O_3/$SrTiO_3$ In 2015 Schütz et al. investigated the GAO/STO heterointerface using hard x-ray photoelectron spectroscopy (HAXPES). They proposed the band diagram as showed in this figure. The 2DEG is highlighted as the red triangular shaped area between the conduction bands of GAO and STO. Figure adapted from Schütz et al.[60]

To do so, one need to understand the band diagram and electron confinement of the Spinel/Perovskite system. The band gap of STO and GAO is 3.5 eV and 7.9 eV, respectively.[60] The large band gap exhibited by GAO is a distinguishing feature commonly observed in typical band insulating oxides and is one example of why the highly conductive interface between GAO and STO holds particular interest. As mentioned in section 2.1.3 (with Figure 2.5b in mind), it is the d_{XZ} and d_{YZ} bands that are lowest in energy and thereby located just below the Fermi energy allowing for electrons to occupy these states. Figure 2.6 illustrates the emergence of the 2DEG responsible for the highly conductive interface.

The emergence of GAO and STO into a heterostructure results in a mismatch in the electrochemical potentials which leads to the band bending of both the conduction bands (CBs) and valence bands (VBs). During GAO thin film growth, oxygen vacancies are generated and as the band bending effect occur near the interface, a triangular shaped confinement ceases to exist. This confinement is what is referred to as the 2DEG and is highlighted in red in Figure 2.6.[60,61]

The electrons in a 2DEG are, as the name refer to, free to move in two dimensions and tightly confined in the third dimension. The tight confinement leads to the formation of quantized energy

levels, which serve as accessible states for the free electrons. The electrons in question originates from oxygen vacancies in the structure, particularly near the interface. To iterate, an oxygen vacancy is the removal of a neutral oxygen where two electrons are left behind. The exact number of electrons that contribute to the 2DEG is somehow unknown, as it can only be measured indirectly as the charge carrier density. Some electrons from the vacancies will be localized and some will move freely in the crystal lattice and hence contribute to the 2DEG.[60] The mobility of the 2DEG is highly influenced by various factors, including scattering sites at the interface and internal interactions such as electron-phonon scattering, electron-electron scattering, and interface roughness scattering, among other scattering mechanisms. Materials that exhibit phenomena like the Kondo effect and colossal magnetoresistance can also experience spin-related scattering, impacting mobility.

The basis of this masters project is founded by the work on high mobility GAO/STO heterostructures published in 2013 by Chen et al. Here the authors presented a new type of 2DEG at the interface between STO and GAO. Besides describing both thin film growth, the crystal structure and electromagnetic properties, they describe a thickness dependency of 2D conductivity at the interface.[15] Figure 2.7a-b display the charge carrier densities and low-field electron Hall mobilities, respectively, measured in several GAO/STO heterostructures with different GAO thin film thickness. It is described that the GAO/STO heterointerface undergoes a transition from being highly insulating to metallic when the thickness of the thin film exceeds a critical threshold of approximately 2 uc. Specifically, at a thickness of 2 uc, the interface exhibits a sheet resistance of approximately 10 kΩ per square and a charge carrier concentration of 2.3 10^{13} cm^{-2} at 300K. This is similar to what have been seen at the perovskite-type LAO/STO heterointerface. From Figure 2.7a it can be seen that the charge carrier densities range from 10^{13} cm^{-2} to more than 10^{15} cm^{-2}. The Hall mobility varies with thin film thickness as well, ranging from $\sim 10^2$ to 10^5 cm^2/Vs. In this study an optimum for mobility and charge carrier density was found for 2.5 uc GAO. Another study conducted in 2016 by Christensen et al. found that an optimum in carrier density and mobility could be reached when depositing 3.5 uc GAO on STO.[62] Besides both studies investigating the GAO/STO interface varying the GAO thin film thickness, GAO/STO samples were grown using different growth parameters and PLD chambers. Hence, it was collectively demonstrated that the thin film thickness did not universally determine the perfect optimum for high mobility GAO/STO interfaces. Instead, they strongly indicate that growth conditions and the specific PLD chamber have a substantial impact on interface quality. Furthermore, the studies revealed the existence of

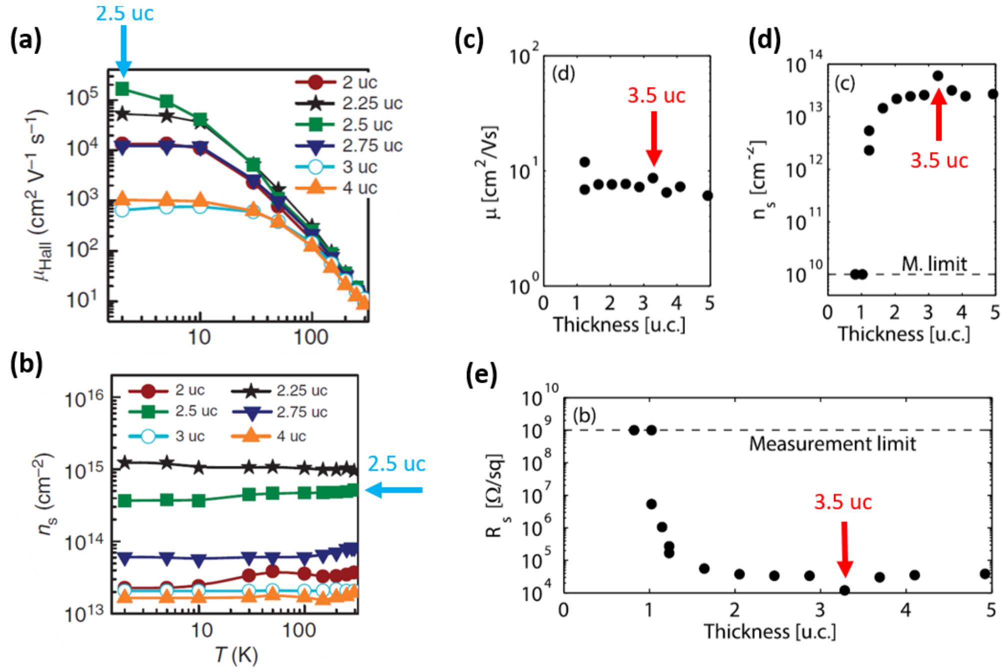

Figure 2.7: Mobility and charge carrier density of GAO/STO Two separate studies made on GAO/STO heterostructures grown to investigate the potential relation between optimum in mobility and GAO thin film thickness. Red and blue arrows highlights the GAO thin film thickness' of which an optimum in mobility was achieved. This emphasize that there may be no universal thickness dependency on optimum in electron mobility, but rather a strong coherence in the number of charge carriers and mobility. a-b) shows the data obtained by Chen et al.[15] in 2013. a) shows that an optimum in mobility was reached for 2.5 uc GAO on STO. b) shows the corresponding carrier density, being in the range of $n_S \approx 10^{14}$ cm^{-2}, exhibited by the heterostructure of 2.5 uc GAO on STO. c-e) shows the data obtained by Christensen et al.[62] in 2016. c) shows the optimum in electron mobility was reached at 3.5 uc of GAO on STO. d) shows the corresponding carrier density, likewise (a), being in the range of $n_S \approx 10^{14}$ cm^{-2}. e) shows the sheet resistance as a function of GAO thin film thickness. Here was it further showed that 3.5 uc GAO on STO had the lowest sheet resistance, which is accordingly with n_S and μ. The figures were adapted from Chen et al. and Christensen et al.

an optimal mobility as a function of charge carrier density, which exhibits greater universality compared to the dependency on film thickness. Both studies concluded that an optimal mobility was achieved when the charge carrier density reached approximately 10^{14} cm^2/Vs, occurring at 2.5 uc and 3.5 uc GAO, respectively.

Lastly, as mentioned in section 2.1.1, there exists a relationship between the dielectric constant of a material and electron mobility.[40,58,63,64] STO, for instance, demonstrates increased electron mobility at lower temperatures due to its elevated dielectric constant, as previously mentioned, reaching values above 20,000 at 2K. The dielectric constant represents a material's ability to store electric charge

and influences the screening of Coulomb interactions among charged particles, referred to as effective charge screening. Materials with higher dielectric constants exhibit stronger charge screening, which reduces the interaction between electrons and ionized scattering sites. Consequently, this reduces scattering of the charge carriers within the 2DEG, resulting in higher electron mobility.

3 Methods

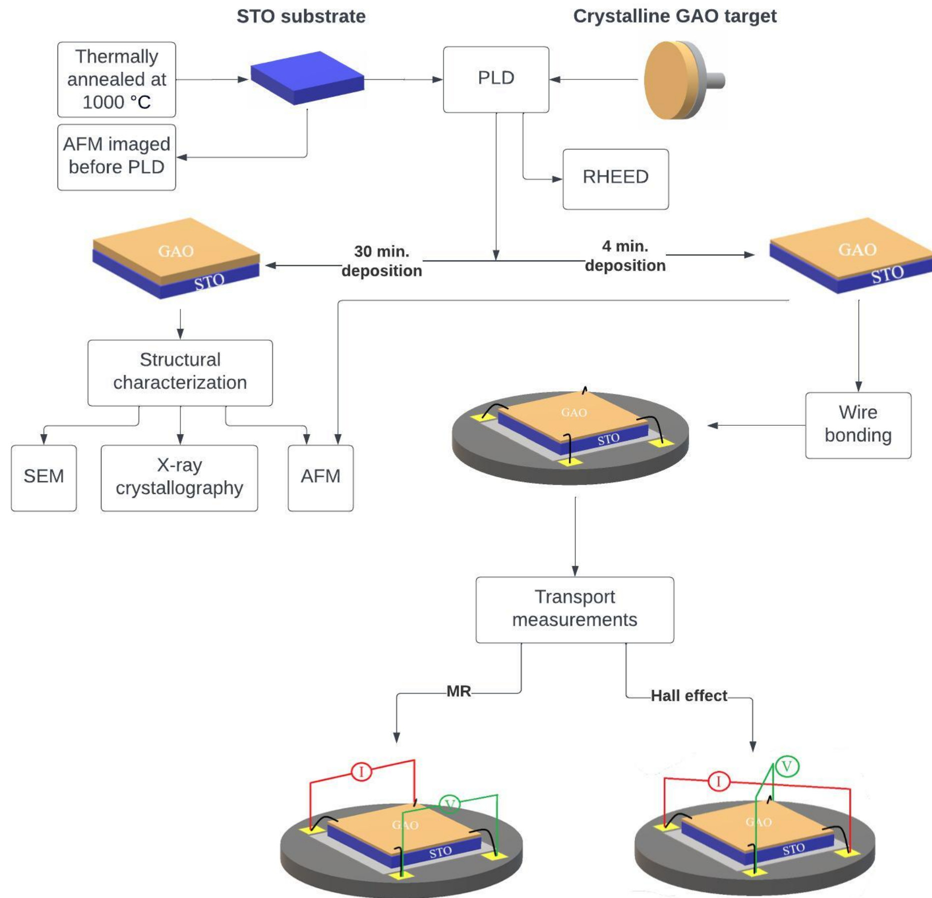

Figure 3.1: Flowchart of laboratory work Flowchart outlining the steps involved in the laboratory work of this masters project. GAO/STO heterostructures were produced by PLD using a thermally annealed STO substrate and a crystalline GAO target. RHEED was used during the first depositions to follow the growth rate. Thin films were made with two different deposition times, 4 minutes (for transport measurements) and 30 minutes (for thickness determination used to calculate growth rates). Structural characterization (SEM, X-ray crystallography and AFM) were performed on the 30 minutes deposited thin films. The 4 minutes deposited thin films were imaged with AFM and wire bonded for the purpose of conducting transport measurements, i.e. MR and Hall effect measurements.

In this masters project GAO/STO heterostructures were prepared using pulsed laser deposition (PLD) and subsequently sheet resistance, magnetoresistance (MR) and Hall effect were measured in order to extract information about the charge carrier concentration and electron mobility of the system. Several techniques were additionally used to gain structural information pre- and post deposition. These techniques included atomic force microscopy (AFM), x-ray crystallography, scanning

electron microscopy (SEM) and reflection high energy electron diffraction (RHEED). The methods and techniques used to study, prepare and test the samples in question are presented in the following sections. The sections are focused to describe the phenomena and expected results for oxide based samples and GAO/STO samples, in particular. The work process, from sample preparation to the final product and the execution of electrical measurements, is displayed with a flowchart in Figure 3.1.

Section 3.1 describes the process of sample preparation which included substrate treatment, atomic force microscopy imaging and the process of sample growth with pulsed laser deposition. Section 3.2 describes and elaborates on the structural characterization and growth rate determination of the grown samples. This includes scanning probe microscopy, reflection high energy electron diffraction and x-ray crystallography (i.e. x-ray diffraction and x-ray reflectometry). Section 3.3, the final section in this methods chapter, describes and elaborates on the electrical characterization going into the necessary details on the wire bonding and back-gating of the samples, utilizing the electrical measurements which include room temperature Van der Pauw measurements, magnetoresistance and the Hall effect.

3.1 Sample preparation

3.1.1 Substrate treatment

High quality STO substrates with a pre-terminated flat surface were supplied by the Japanese company Shinkosha.[65] The substrates had been miscut with an angle of $<0.5^{\circ}$ relative to the surface normal which consequently results in ∼45-223 nm wide terraces.[66,67] These are theoretical values supplied by Shinkosha and may be verified by scanning probe microscopy (SPM). Each step corresponds to a single unit cell of the STO lattice (0.39 nm). Furthermore, the as-recieved substrates has been surface terminated with TiO_2. However, the surface of the as-received substrates is comprised of nonlinear arrays of terraces, which are not ideal for thin film deposition. An atomic force microscopy (AFM) image of an as-received STO substrate is shown in Figure 3.2a, imaged by Shinkosha. The substrates were supplied in 15 × 15 mm sizes with pre-processed grooves on the back-side outlining 9 squares of 5 × 5 mm, as shown in Figure 3.2b, that can easily be broken by hand into separate squares. This concept ensured the same crystal quality of all 9 squares and was expected to improve the experimental consistency in the planned experiments.

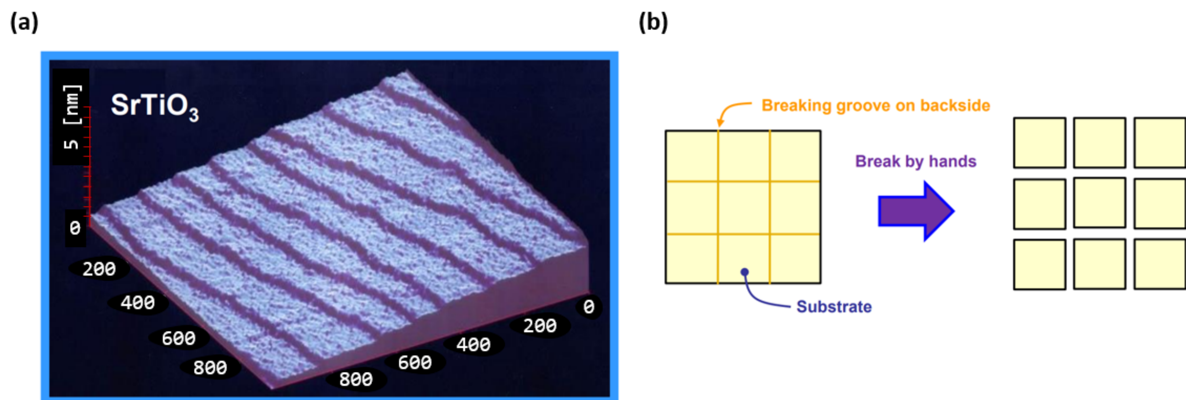

Figure 3.2: $SrTiO_3$ substrates from Shinkosha a) Atomic force microscopy image of a STO substrate showing the as mentioned terraces. b) The as recieved substrates came in 3x3 5 mm square pieces. Figures adapted from Shinkosha.[65]

Prior to deposition, the substrate was surface terminated and subsequently annealed in oxygen to create well-defined and atomically smooth terraces. A well-defined terrace should ideally be linear and have a 90° sharp step to ensure optimal growth conditions for thin film growth. The as received substrate had been surface terminated with a strong acid (i.e. hydrofluoric acid) by edging away SrO to gain a surface consisting primarily of TiO_2. This ensured the utmost favorable growth conditions while depositing. The substrate was subsequently investigated using AFM to confirm the presence of the aforementioned well-defined terraces. Further description on AFM and the substrates used in this project is described in sections 3.2.1 and 4.2.1. Degreasing and dedusting of the substrate surface using acetone and isopropanol, respectively, was performed in between annealing, imaging, and deposition to secure a clean surface.

Substrate annealing was executed in a tube furnace at 1000°C with a dwell time of 60 minutes in the presence of 1 bar molecular oxygen. The heating and cooling rate was set to 1.66 °C per minute. Oxygen gas was introduced in the furnace to control the environment and prevent intrinsic oxygen from leaving the structure. The annealing procedure involved heating the substrate to above its recrystallization threshold, maintaining the temperature at this designated level for the required duration, and subsequently cooling it down to room temperature to complete the recrystallization process.

3.1.2 Pulsed laser deposition

Pulsed laser deposition (PLD) is a laser ablation technique used as a central tool in thin film growth.[68–70] An illustration of a PLD system is showcased in Figure 3.3. The technique involves using high-energy laser pulses to elevate the energy of a target material to the point where plasma is formed, leading to plasma ablation.[71] The experimental setup consists of a KrF excimer laser with a wavelength of 248 nm, which emits individual pulses guided through a beamline into a vacuum chamber. Inside the chamber, there is a designated target and a chosen substrate. The laser pulses are concentrated on the target, generating an extremely high energy density on its surface. Once the energy density surpasses the ablation threshold of the material, the absorbed energy causes the material to evaporate as plasma.

The plasma plume contains high-energy ionized particles that will be ablated onto any surface within a distance of few centimeters.[71,72] A substrate of choice can be placed in front of the target and ionized particles will ablate onto the substrate surface forming a thin film. A layer of material, on top of another material, can be recognized as a thin film if the thickness of the layer is in the order

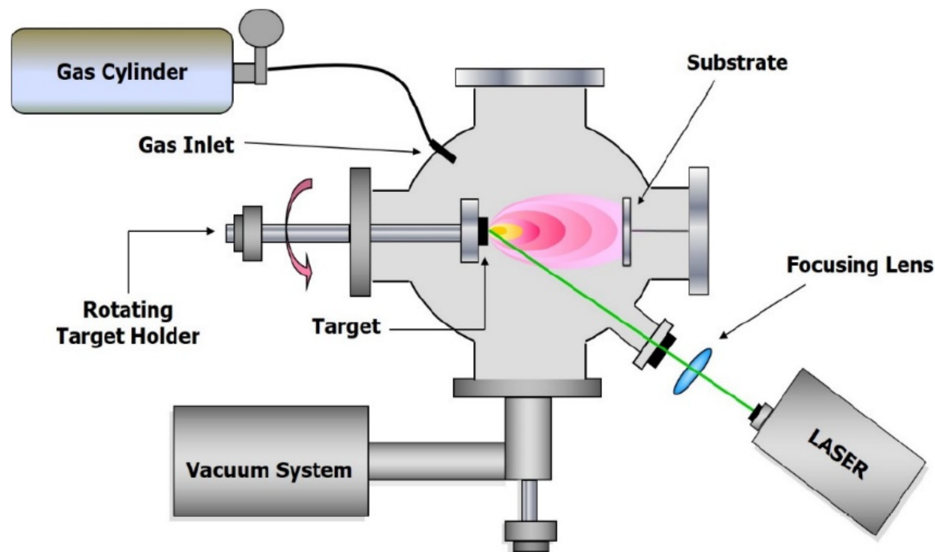

Figure 3.3: Schematic of the setup for Pulsed Laser Deposition The Pulsed Laser Deposition (PLD) setup consist of a vacuum chamber, a gas inlet, target holder, substrate holder and heater, and a laser focused through a focusing lens into the chamber. The Figures is adapted from Bonis and Teghil 2020.[72]

of 0.1μm or smaller. The thin film quality can be controlled by varying different parameters such as laser wavelength, laser fluence, gas composition, pressure before, during, and post-deposition, target to substrate distance, plume geometry, and deposition temperature.[?, 71] As the thin film quality is highly dependent on the aforementioned parameters, likewise, are the plume properties dependent on background gas and laser fluence.[73]

One critical part of GAO deposition on STO is to have high-energy plasma as this is one of the primary catalysts for high concentrations of oxygen vacancies formed at the interface. To gain a high concentration of oxygen vacancies, and hence a high mobility GAO/STO interface, it is therefore important to generate high energy plasma along with optimal growth conditions. High energy plasma can be gained from using a high laser fluence.

$$\text{Fluence} = \text{E}_{\text{Laser}}/\text{Area}_{\text{Spot size}}, \ [J/cm^2] \tag{3.1}$$

Laser fluence is defined as laser energy per laser spot size area and is a measure of how much energy is delivered per unit area. The laser energy is measured in front of the sample with an energy meter. The laser spot size is dependent on mask size, mask position and lens position which are all carefully measured and set prior to experiments. A high laser fluence secures the crucial high kinetic energy of the ablated species, which is important as plasma species of high kinetic energies have a direct effect on film crystallinity and the formation of oxygen vacancies. The expansion and overall geometry of the plasma plume is additionally highly influenced and controlled by the gas species and background gas pressure. The background gas, in the case of GAO/STO thin film deposition, primarily acts as a moderator of the kinetic energy of the plasma species through collisions.[71]

Gaining a comprehensive understanding of how each deposition parameter can impact the quality of thin films during PLD is therefore crucial in order to effectively control and influence the results.

3.2 Structural characterization and growth rate determination

3.2.1 Scanning probe microscopy

Scanning probe microscopy (SPM) is a family of techniques used to investigate the surface properties of materials at the nanoscale. It involves scanning a sharp probe or tip across the surface of a sample to gather information about its topography, physical properties, and interactions with the probe.[74]

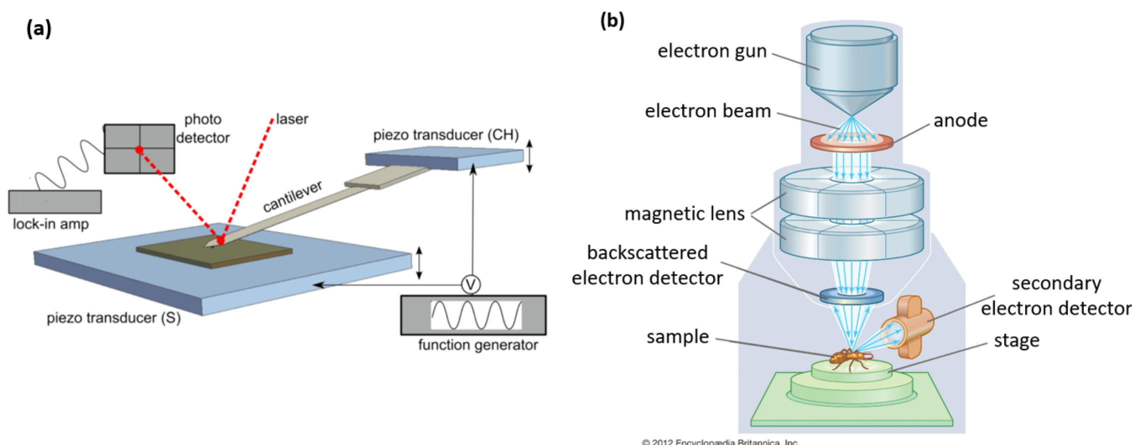

Figure 3.4: Scanning probe microscopy. Schematics of a) atomic force microscope and b) scanning electron microscope. Figures adapted from the National institute of standards and technology (NIST) and Britannica on SEM.[78]

The most well-known technique within SPM is atomic force microscopy (AFM), where a small cantilever with a sharp tip is used to scan the sample surface.[75–77] A schematic of AFM is shown in Figure 3.4a. As the tip moves across the surface, it experiences forces, which are then measured and used to construct a high-resolution image of the sample's topography. Several modes and variations of AFM exist including tapping mode and contact mode, as well as conducting AFM (c-AFM) and piezoelectric force microscopy (PFM). Tapping mode is a commonly used imaging mode that enables imaging of delicate or soft samples. Tapping mode involves oscillating the cantilever and probe tip near its resonant frequency while scanning the sample surface. This mode utilizes a feedback loop to maintain a constant oscillation amplitude, which provides information about the surface topography and other properties. By continuously adjusting the z-piezo position based on the error signal, the feedback loop in tapping mode keeps the cantilever oscillation amplitude constant as it scans the sample surface. The resulting topographic image is formed based on the feedback corrections applied during the scanning process.

In this project, AFM was employed to assess the quality of both the substrate surface and the resulting thin film. The investigation involved imaging various locations on the samples, with predominant imaging sizes of 10x10 μm and 2x2 μm. The primary imaging technique utilized for this purpose was the height sensor, although phase imaging could also be employed to examine the surface's morphology and crystallinity.

Another well known technique withing SPM is scanning electron microscopy (SEM).[76,77,79] A schematic of SEM is shown in Figure 3.4b. Electron microscopy employs electrons to visualize and capture images of the surface of a sample. An electron gun generates electrons and an anode, a positively charged metal plate, attracts the electrons to form a beam. A pair of magnetic lenses focus' the beam towards the sample. The electrons scatter of the sample, some elastically detected by the backscattered electron detector, and some in-elastically as secondary electrons detected by the secondary electron detector. Furthermore, the resolution is influenced by the characteristics of the electron wave, which has a wavelength of 6 pm. As a result, the achievable resolution for SEM can fall within the range of 1 to 10 nm. Figure 3.2b illustrates components and setup for SEM. SEM involves scanning a focused beam of electrons over the surface of a sample. As the beam scans the surface, it interacts with the sample, and different interactions produce various signals, including secondary electrons, backscattered electrons, and X-rays. These signals are collected by aforementioned detectors to generate a detailed image of the sample surface. Secondary electrons are electrons that undergo inelastic scattering within the sample whereas backscattered electrons are electrons that originate from the primary beam and, upon striking the sample, reflect off the surface with high energy and return in the opposite direction. In comparison to AFM, SEM offers several advantages for surface analysis. SEM can provide information about surface morphology, elemental composition, and crystal structure. It has a larger working distance of up to 1 cm, allowing for a broader field of view. However, SEM requires a vacuum environment, while AFM can operate in various environments i.e. air and liquid. SEM necessitates the sample to be conductive or coated with a conducting layer (i.e. gold or carbon), while AFM can handle both conducting and non-conducting samples. Additionally, AFM in tapping mode is a non-invasive technique suitable for investigating delicate features without damaging conductive interfaces, whereas SEM is considered highly invasive due to its use of highly accelerated electrons. SEM was utilized in this project to create an image of which the thickness of a GAO thin film could be measured.

3.2.2 Reflection High Energy Electron Diffraction

To verify the growth of GAO thin film, a variety of methods can be used for this purpose.[80,81] Reflection High-Energy Electron Diffraction (RHEED) can be used in situ, during PLD, to follow in real time the growth on the atomic level and thereby gain a direct estimate of the number of deposited unit cells and total thin film thickness.[82–84] High-energy electrons have energies above 1 keV[84] and interact in-elastically with the first few unit cells of the targeted surface resulting in

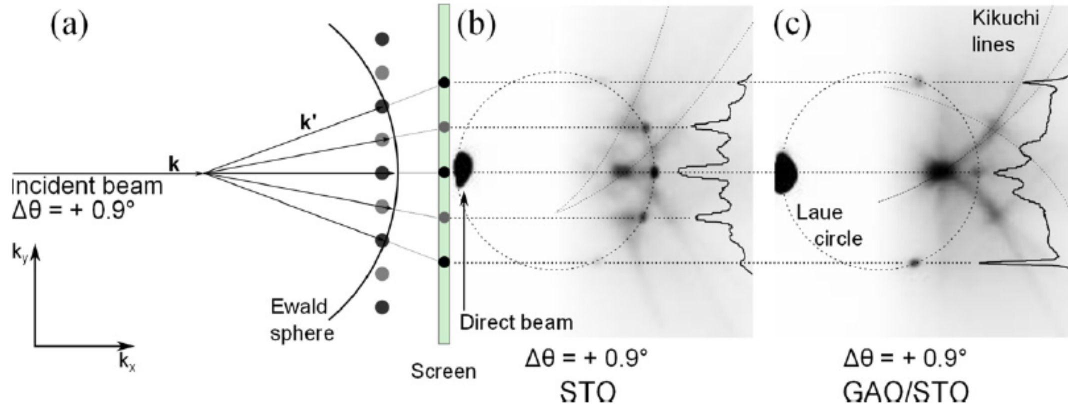

Figure 3.5: The Ewald spheres of STO and GAO/STO a) Ewald construction where black dots represent reciprocal rods and grey dot s indicate the absent rods for GAO. b) Ewald sphere drawn on the RHEED pattern of the surface of STO. c) Ewald sphere drawn on the RHEED pattern of the surface of the as deposited GAO/STO. The images are adapted from Schütz et al.[85]

Bragg-diffraction that can be detected within the probing depth of RHEED. The high energy results in the electron wavelength being much greater than the spacing between direct lattice points,

$$\lambda_{\mathrm{e}} << d_{\mathrm{spacing}}(lattice_{\mathrm{direct}}). \tag{3.2}$$

As a consequence the radius of the Ewald sphere will be much smaller compared to the spacing between reciprocal lattice points,

$$r_{\mathrm{Ewald}} << d_{\mathrm{spacing}}(lattice_{\mathrm{reciprocal}}). \tag{3.3}$$

The Ewald sphere is a geometric construction that allows for the relationship between the wavevector of the incident and diffracted electron beam, the diffraction angle for a given reflection, and the reciprocal lattice points of the crystal to be solved.[86] Due to the large radius of the Ewald sphere compared to the small direct lattice spacing, a small part of the Ewald sphere can be perceived as flat. For each of the reciprocal lattice points, there will be a corresponding electron diffraction beam that will result in a specular spot on the Ewald sphere. The central specular spot occurs as a result of the directly transmitted electron beam, whereas secondary specular spots are a result of the electrons being diffracted. The resulting diffraction pattern will hence simply be a small part of a recurring crystal lattice that can be fitted onto the Ewald sphere.

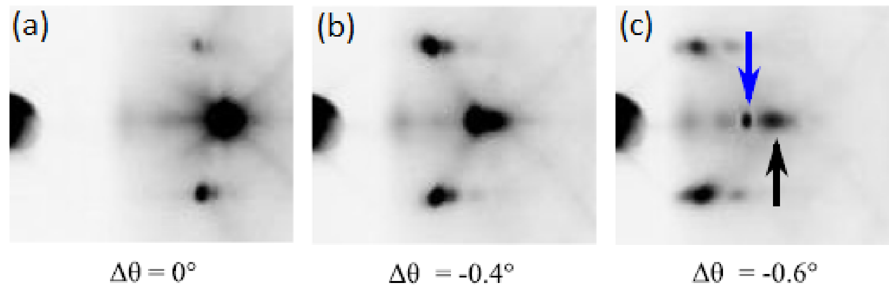

Figure 3.6: RHEED images of bare STO before deposition The specular spots (black spots) can be split by optimizing the angle of incidence. This splits the signal from Kikuchi lines (black arrow) and electrons diffracted of GAO (blue arrow). The images are adapted from Schütz et al.[85]

The RHEED pattern of GAO on STO has been studied by Schütch et al.[85] Here the authors show a sketch of the Laue circle on top of a recorded image of the diffraction pattern of STO alone (Figure 3.5b) and GAO on STO (Figure 3.5c). The Laue circle is a contraction from the Ewald sphere seen in figure 3.5a. The dark gray spots located on the Laue circle are referred to as Laue spots, diffraction spots resulting from electrons interfering with the crystal structure. Kikuchi lines and the corresponding line profile taken along the Laue circle are sketched as well. Kikuchi lines are an artifact from the interference of diffracted electrons from the primary electron beam.

The diffraction pattern of STO, seen in Figure 3.5b shows two centered diffraction spots, which due to a change in the angle of incidence has split the primary center spot into two spots. As seen in Figure 4.7a-c, the splitting of the center specular spot into two distinctive spots is done by changing the angle of incidence from the optimized position of $\Delta\theta = 0$ to a slightly tilted position of $\Delta\theta = 0.6$. The tilted position does not affect the growth of the GAO thin film but splits the diffraction signal from electrons that will be diffracted by the growth of GAO (blue arrow), from the intensity signal originating from Kikuchi lines (black arrow). This enables the direct and real-time monitoring of layer-by-layer GAO unit cell growth.

Figure 3.5c is the post-deposition GAO/STO diffraction pattern and shows how the primary center spots have changed in size from two spots to one large spot. The position of the two secondary diffraction spots has changed as well along with the Laue circle line profile. The overall change of the diffraction pattern indicates a change in the surface crystal structure, which is to be expected for the growth of a heteroepitaxial interface as is the case for GAO on STO. For a more detailed understanding of thin film growth, analyzing the RHEED intensities monitored before and during growth is of great advantage.

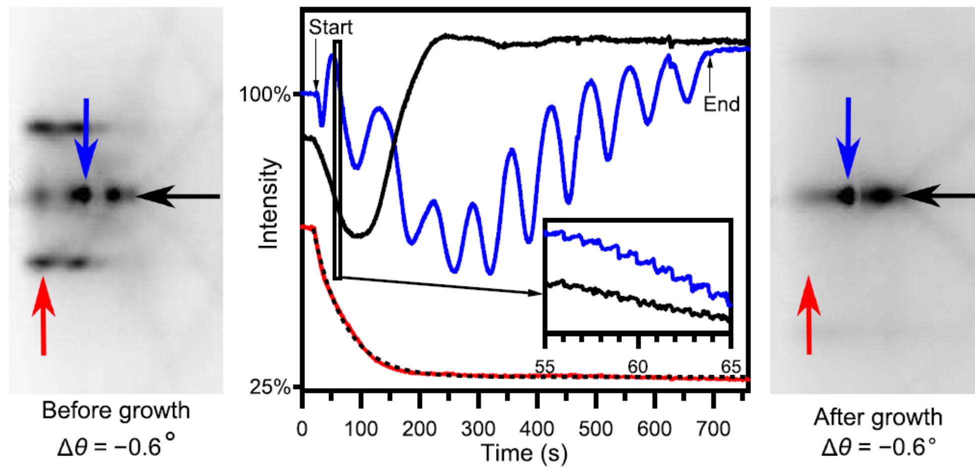

Figure 3.7: RHEED oscillations during PLD of γ-Al_2O_3 on $SrTiO_3$. Before growth (left image) is seen the RHEED pattern of STO after the primary specular has been split by optimizing the incidence angle. After growth (right image) are only two dark spot still visible. The monitored RHEED signals (center image) showcase three signals. The blue signal corresponds to the layer-by-layer growth of GAO. The black signal corresponds to the signal from Kikuchi lines. The red signal corresponds to surface of STO. The images are adapted from Schütz et al.[85]

For RHEED to be used as a tool to follow crystal growth as well as to confirm high crystallinity in the case of GAO on STO, it is crucial to find the STO RHEED (0,0) pattern as shown in Figure 4.7a and subsequent tune the angle of incidence to a degree at which the center specular spot is split into two as has been done in Figure 4.7c.

Figure 4.8 shows the evolution of the electron diffraction pattern detected pre- and post-deposition with the corresponding intensity profiles recorded during deposition. Monitoring and analyzing the three diffraction spots marked with a blue, black, and red arrow gives different information about how the surface crystal structure is changing during deposition.

The diffraction spot marked with a blue arrow is, as mentioned, the result of electrons being diffracted from GAO during deposition. Well-defined oscillations are detected from this spot as seen from the blue RHEED intensity oscillations. The oscillations are a direct image of the increasing and decreasing surface roughness resulting from the GAO ablation. One oscillation corresponds to the deposition of ¼ of the GAO unit cell meaning that four RHEED oscillations equal one unit cell of GAO.

The difference in phase and crystal structure for perovskites and spinels manifests itself even further when analyzing the black and red monitored RHEED intensities. The black RHEED intensity

corresponds to what appears to be a diffraction spot marked with a black arrow. The spot is in fact the result of diffracted electrons acting as a pseudo-primary beam from below the crystal structure. It is an enhancement of the surface-wave resonance resulting from intersecting Kikuchi lines that form an intensity increase. The intensity and behavior of Kikuchi lines are not affected by the periodic change in surface roughness occurring during growth, which means that no oscillations can be seen from this intensity profile. The decrease and subsequent increase of the signal are inherently connected to the aforementioned difference in the crystal structure of STO and GAO. The intensity decreases as a result of the increased disorder, as the electrons are being absorbed and diffracted from the heteroepitaxial interface but will begin to increase as the thickness of GAO exceeds the probing depth of RHEED.

As the intensity of Kikuchi lines increases, a similar inverse behavior is seen for the secondary specular spot marked with a red arrow. The red RHEED intensity decreases exponentially and corresponds to the (1,0) RHEED specular spot from STO. As GAO is ablated onto STO, the probing thickness will eventually exceed so that electrons can no longer reach the surface of STO and thus the diffraction spots of STO disappear.

3.2.3 X-ray crystallography

Another technique that is frequently used to gain information about the crystallinity and quality of thin films is x-ray crystallography, particularly x-ray diffraction and x-ray reflectometry. Figure 3.8a illustrates the process of which x-rays are produced. Electrons are accelerated with an electric field and directed towards a metal target, such as copper or tungsten. This process results in two types of x-ray radiation: Bremsstrahlung and characteristic radiation. Bremsstrahlung radiation is created when the accelerated electrons interact with the metal target nucleus, causing the electrons to slow down and change direction, which in turn converts their high kinetic energy into electromagnetic radiation i.e. x-rays. Characteristic radiation, on the other hand, is generated when the accelerated electrons interact with the electrons in the metal target, causing the electrons to become excited and then emit x-ray photons as they return to a lower energy state. This type of radiation is unique to each metal target. However, the majority of x-rays generated during this process is Bremsstrahlung radiation. x-ray radiation can range in wavelength between 0.01-10 nm.[87]

X-ray diffraction (XRD) and X-ray reflectometry (XRR) are two analytical techniques within x-ray crystallography that are used to study and characterize atomic structures and determine the

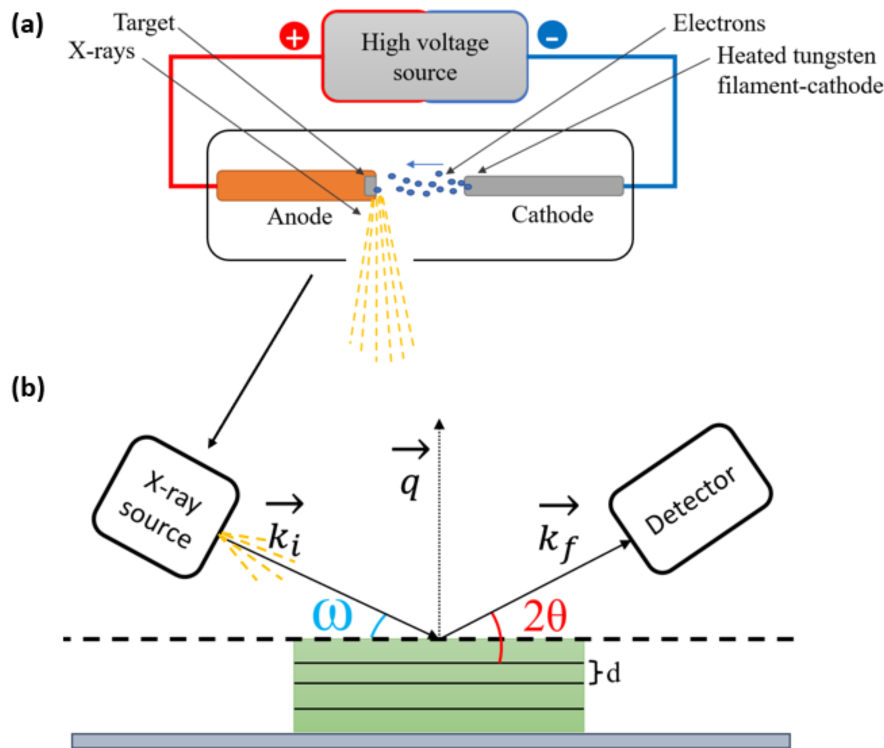

Figure 3.8: X-ray generation and scattering a) X-rays are generated by heating up a tungsten filament-cathode of which electrons are produced. The electrons hit the anode target which generates x-rays. b) The generated x-rays interacts with the material with some incidence angle ω and wave vector $\vec{k_i}$. Crystal planes normal to the scattering vector $\vec{q}$ will diffract x-rays. The scattered x-rays will exit the crystal planes with the scattering angle θ and wave vector $\vec{k_f}$.

morphology and crystallinity of a material.[87–89] XRD is particularly useful as a characterization method for crystalline materials as any occurring Bragg peaks in the diffraction pattern can be directly linked to the distance between atoms in the crystal lattice. When x-rays are directed towards crystalline structures, the atoms in the well-defined crystal lattice scatter the x-rays, creating a diffraction pattern. This pattern provides information about the arrangement of the atoms in the crystal lattice, their interatomic spacing, the size and orientation of the atoms and the symmetry of the crystal. The condition for diffraction follows that only planes perpendicular to the scattering vector, $\vec{q}$, will appear as diffraction peaks in XRD. This is illustrated in Figure 3.8b. In principle, according to Bragg's law only planes perpendicular to the scattering vector will appear in a diffraction pattern. The scattering vector is defined from the subtraction of the wavevectors $\vec{k_i}$ and $\vec{k_f}$.

$$\vec{q} = \vec{k_f} - \vec{k_i} \tag{3.4}$$

Given that the material is highly crystalline can the distance between the planes detected by XRD can be found by using Bragg's law. Bragg's law states that the angle of incidence ω (the angle of which the x-ray enters the crystal lattice) and the angle of scattering θ (the angle of which the x-ray exits the crystal lattice) are equal. When the path difference (d) between two x-ray waves is equal to a whole number (n) of wavelengths it will result in constructive interference.

$$2d\, sin\theta = \lambda n \tag{3.5}$$

where d is the interatomic distance, θ is the incidence angle and λ is the wavelength. Isolating for d gives and expression for the interatomic distance:

$$d = \frac{\lambda n}{2\, sin\theta} \tag{3.6}$$

The interatomic distance in a material can be calculated from the crystal lattice parameter (a) and the orientation of crystal planes of which the x-rays will intercept, i.e. the Miller indices, (hkl).

$$d = \frac{a}{\sqrt{h^2 + k^2 + l^2}} \tag{3.7}$$

$$\frac{2a}{\sqrt{h^2 + k^2 + l^2}}\, sin\theta = \lambda n \tag{3.8}$$

Eq. 3.8 combines eq. 3.6 with Braggs law (eq. 3.4) making it possible to calculate the angle of which Bragg peaks are expected to appear during XRD for a certain material. This is applicable for both single crystal materials as well as heterostructures, particularly useful for characterization of thin films grown on crystalline substrates.

Figures 3.9a and 3.9b displays the XRD and XRR data, respectively, of $La_{0.88}Sr_{0.12}MnO_3$/ $(LaAlO_3)_{0.3}(Sr_2AlTaO_6)_{0.7}$ (LSMO/LSAT) oxide heterostructure.[90] The diffraction pattern of LSMO/ LSAT shows several peaks including the thin film peak of (002)LSMO. Following the thin film peak is the substrate peak of (001)LSAT. Due to the structural similarities between LSMO and LSAT, the thin film Bragg peak is located right next to the substrate Bragg peak. Laue oscillations are visible in this diffraction pattern of the LSMO/LSAT heterostructure, as highlighted by a magnified image

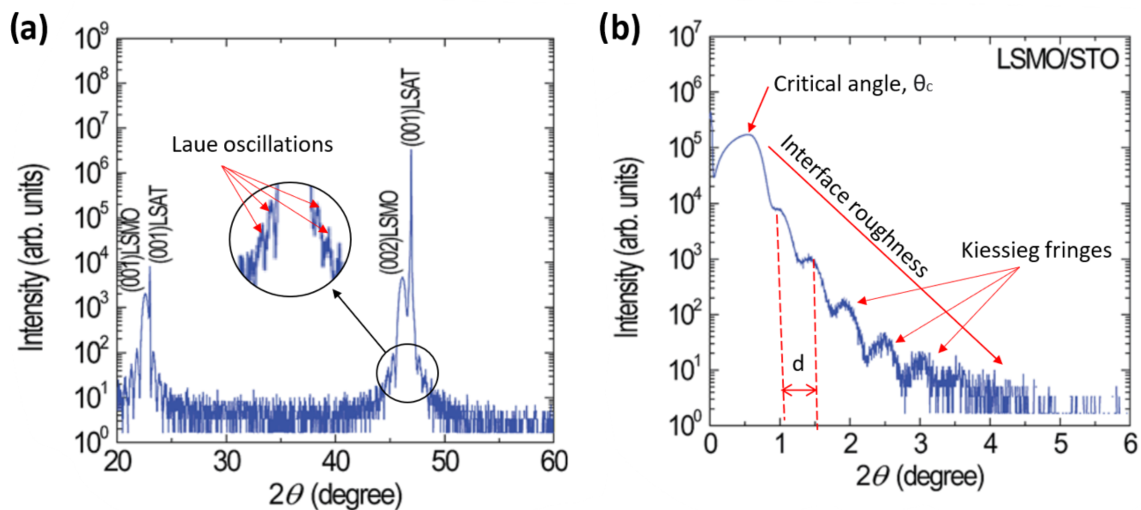

Figure 3.9: XRD and XRR of oxide thin films a) XRD data from a LSMO/LSAT heterostructure. Laue oscillations are highlighted by red arrows. b) XRR data from a LSMO/STO heterostructure. Critical angle, interface roughness and Kiessieg fringes is highlighted by red arrows. Figures adapted from Kim et al.[90]

and red arrows in Figure 3.9a. Not all thin films will show Laue oscillations which can be attributed to lack of order and defects in the crystal lattice. Laue oscillations are caused by interference of diffracted X-rays, within the sample, as they propagate through the crystal. The incident x-rays interact with the atoms in the crystal lattices and are subsequently scattered in all directions within the crystal. The scattered x-rays will add up constructively, if they are in phase, which results in a strong diffraction peak. The peaks with highest relative intensity is recognized as Bragg peaks and is correlated to a corresponding Bragg angle. Changing the angle slightly away from the Bragg angle results in the x-rays deviating slightly in phase. Interference effects leads to the intensity of the x-rays to oscillate as a function of 2θ, the summation of incident and scattering angle, until the waves are completely out of phase and intensity drops to zero.

The diffraction peaks in XRD can, furthermore, give information about epitaxial growth where peak broadness may indicate if the thin film contains stacking faults, has a lower degree of crystallinity, microstrain or other defects that will enhance disorder.[88] Peak position can be used to calculate the unit cell dimensions as 2θ is related to the lattice parameter through Braggs law(eq. 3.4). A small change in peak position, as compared to the pre-calculated table value, may indicate strain and changes in unit cell dimensions that can be attributed to how the thin film is made and connected to the substrate. For structures with higher orders of crystallinity, Bragg peaks may

be accompanied by Laue oscillation and the distance between oscillations can be used to extract information on interatomic distances. In the case of few or vague Laue oscillations present in the diffraction pattern, XRD can be combined with XRR for thin film thickness determination.

XRR relates the thickness, density and interface roughness in one measurement. Reflectometry is conducted by varying the incidence angle ω.[88] At low incidence angles, the phase shift upon reflection is minimal, and constructive interference predominates. This results in enhanced intensity and the appearance of fringes, such as Kiessig fringes, with alternating maxima and minima. However, as the incidence angle increases, the phase shift upon reflection becomes more significant. The increased angle leads to a larger path difference between the incident and reflected waves. This difference in path length affects the interference pattern, leading to destructive interference and a decrease in the overall intensity of the reflected wave. This is what can be seen in Figure 3.9b. From the data it is possible to read of the critical angle, the thin film thickness and the interface roughness. Figure 3.9b shows the XRR data of the LSMO/LSAT oxide heterostructure. The critical angle is the angle of which the x-ray beam goes from being refracted to total internal reflection which results in the first drop in intensity. The thickness is related to the period of Kiessieg fringes and the interface roughness is related to the slope. The data presented in Figure 3.9b shows clear oscillating Kiessieg fringes and thus a thin film thickness of LSMO can be extracted using Bragg's law.

3.3 Electrical characterization

To study the electronic properties of 2DEGs, such as those formed at the heterointerface of GAO/STO, two commonly used experimental setups used for this purpose are the Van der Pauw method and the Hall effect method. The Hall effect can be measured by applying a perpendicular magnetic field to the sample, whereas the Van der Pauw method does not require a magnetic field. The GAO/STO heterostructures produced in this masters project were bonded to a chip carrier and measured using the former mentioned methods to get the sheet resistance, charge carrier density and electron mobility of each sample.

3.3.1 Wire bonding

After deposition of the GAO thin film, the GAO/STO heterostructure was placed on a chip carrier using a conducting silver paste. To establish electrical contact between the conducting pads of the chip carrier and the GAO/STO interface, 25 μm thick aluminum leads was employed to penetrate the GAO layer, by ultrasonic wedge bonding. The wires were positioned near the corners of the sample in a square formation, as this is the optimal arrangement for the Van der Pauw measurement method. An illustration of a wire bonded GAO/STO sample and a photograph of the actual wire bonded sample captured through a microscope lens are depicted in Figures 3.10a and 3.10b, respectively.

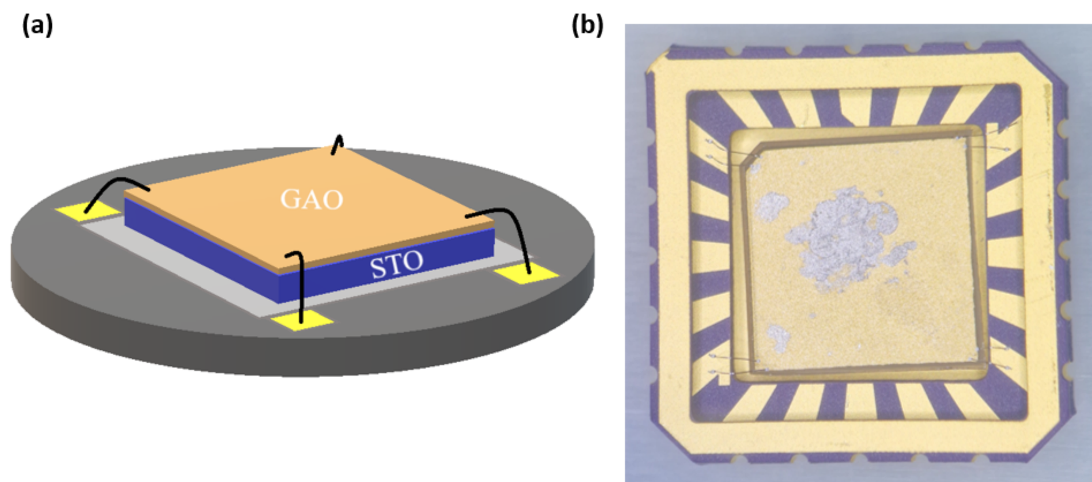

Figure 3.10: Wire bonding GAO/STO samples were mounted on a chip carrier (grey platform) and each corner of the chip was bonded to a conducting pad (yellow square). a) illustration of the bonded GAO/STO heterostructure as compared to the b) actual wire bonded GAO/STO heterostructure.

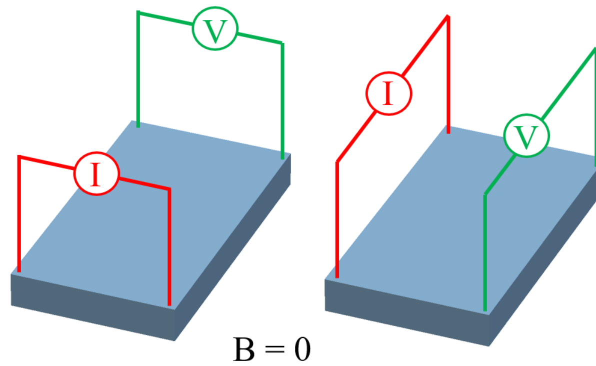

Figure 3.11: Van der Pauw setup. The resistivity can be measured using the 4-probe setup, also referred to as the Van der Pauw setup, by applying a current (I) between two points and measuring the voltage drop (V) between the remaining two points.

3.3.2 Van der Pauw method

The 4-point probe setup is commonly referred to as the Van der Pauw (VdP) method and is a technique used to measure the electrical resistance and conductivity of a thin, planar sample. It involves measuring the resistance of a sample between four points arranged in a square pattern, and then repeating the measurement with the sample rotated by 90 degrees. By analyzing the resistance measurements, the VdP method can determine the sheet resistance and give a representation of how conductive the sample is. The VdP setup is sketched in Figure 3.11 and was employed to measure the overall resistance of the GAO/STO samples, initially at room temperature and subsequently measuring the resistance as a function of temperature ranging from 300K to 2K.[91]

3.3.3 Magnetoresistance and Hall effect

Following the measurement of resistance using the VdP setup, where there is no magnetic field applied, the GAO/STO samples were subsequently placed inside a 16T (tesla) cryostat. This setup allowed for the examination and investigation of the effects of a magnetic field on the samples. Figure 3.12 shows an illustration of the wire bonded GAO/STO chips in a VdP setup (a) and a Hall setup (b). Applying a magnetic field to the VdP setup enables for magnetoresistance measurements. Magnetoresistance (MR) is a measure for the change in electrical resistance of a material in response to an applied magnetic field. As it is commonly known will a charge in a magnetic field bend into a cyclotron motion due to the Lorentz force. The measured resistance may vary at particular magnetic fields because of changes in the electron scattering, resulting in increased or decreased

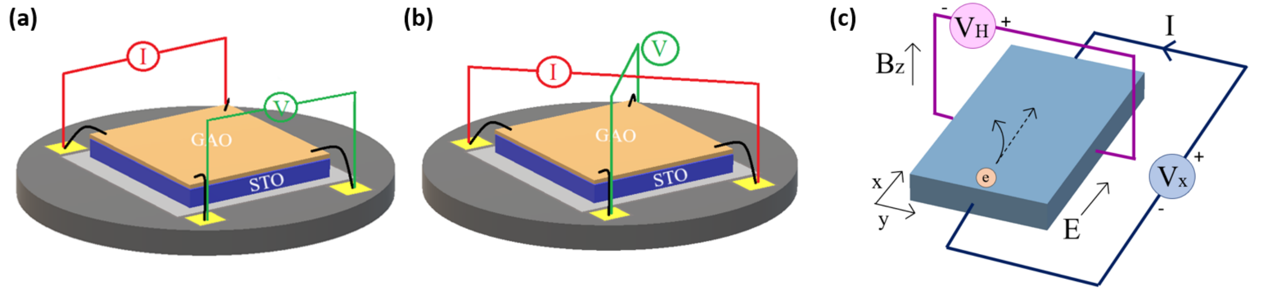

Figure 3.12: Electrical characterization setups The wire bonded GAO/STO chips were measured using the VdP setup (a) and the Hall setup (b). The illustration in (c) shows the occurrence of two voltage contributions, the V_x and the V_H, where the latter originates from the Hall effect.

resistance, indicating the conductivity of the sample between the designated probes. The Hall effect is the phenomenon where a magnetic field perpendicular to an electric current applied to a material induces a voltage across the material. This is illustrated in Figure 3.12b where the Hall setup for a wire bonded GAO/STO chip is shown.

From section 2.2 it was established how the conductivity of a material is a balance between the number of charge carriers and their freedom of movement. The VdP setup, with and without magnetic field, and the Hall setup can give a measure of the resistance and allow us to extract the aforementioned quantities. To understand the origins of the sheet resistance and Hall resistance, and what contributes to their quantities, let us consider a situation with a 2D material such as the 2DEG at the GAO/STO interface. Figure 3.12c illustrates a 2D material with an applied electric and magnetic field. The electrons are driven by the direction of the electric field, E. Since it is a 2D material, the electrons are only free to move in the X and Y direction. A perpendicular magnetic field is applied and is directed out of the plane. The voltage measured along the x-direction, denoted V_x, is the voltage drop known from the VdP setup. The voltage measured along the y-direction, denoted V_H, is the Hall voltage and is the voltage difference that is produced perpendicular to both the current flow and the magnetic field. Hall voltage can be used to measure the Hall resistivity tensor, which describes the relationship between the magnetic field and the current density in the material. To find an expression for the Hall resistance one may consider the contributing forces that act upon a charge in motion, in this given situation.[91,92]

$$\vec{F} = \left|\frac{\partial \vec{P}}{\partial t}\right|_{Fields} + \left|\frac{\partial \vec{P}}{\partial t}\right|_{Scattering} \tag{3.9}$$

Here $\vec{F}$ is the sum of forces contributing to the change in momentum of the charge over time, *Fields* is the Lorentz force driving the charge forward and *Scattering* refers to the counteracting forces originating from scattering events. After some time, the system can be assumed to reach a steady state where scattering events and the Lorentz force balances out. Therefore eq. 3.9 can be set to 0 and we get the following expression:

$$0 \ = \ -e(\vec{E} + \vec{V} \times \vec{B}) - \frac{m\,\vec{V}}{\tau} \tag{3.10}$$

as

$$\left|\frac{\partial \vec{P}}{\partial t}\right|_{Scattering} = \frac{m\,\vec{V}}{\tau} \tag{3.11}$$

$$\left|\frac{\partial \vec{P}}{\partial t}\right|_{Fields} = -e(\vec{E} + \vec{V} \times \vec{B}) \tag{3.12}$$

Then we isolate for $\vec{E}$ in eq. 3.10 and get

$$\vec{E} \ = \ \frac{m\,\vec{V}}{e\,\tau} - \vec{V} \times \vec{B} \tag{3.13}$$

and realize that $\frac{m}{e\tau}$ is, in fact, the inverse expression for electron mobility.

$$\frac{1}{\mu} \ = \ \frac{m}{e\,\tau} \tag{3.14}$$

And thus we can write:

$$\vec{E} \ = \ \frac{\vec{V}}{\mu} - \vec{V} \times \vec{B} \tag{3.15}$$

Eq. 3.15 can be expanding by performing the cross product to get eq. 3.16 and subsequently set up a vector to get eq. 3.17:

$$\vec{E} = \frac{1}{\mu}\begin{pmatrix} V_x \\ V_y \end{pmatrix} - \begin{pmatrix} V_y \cdot B_z \\ -V_x \cdot B_z \end{pmatrix} \ = \ \frac{1}{\mu}\begin{pmatrix} V_x \\ V_y \end{pmatrix} - \begin{pmatrix} V_y \\ -V_x \end{pmatrix} B_z \tag{3.16}$$

As mentioned in the beginning of the section, the electrons are only free to move in the X and Y direction. Additionally, an out of plane B-field is applied to the sample giving the B vector only

a Z component.

$$\vec{E} = \begin{bmatrix} \frac{1}{\mu} & -B_z \\ B_z & \frac{1}{\mu} \end{bmatrix} \begin{bmatrix} V_x \\ V_y \end{bmatrix} \tag{3.17}$$

Recalling Ohm's law and the correlation between current density, electric field and conductivity, one can write a matrix that include the conductivity and resistivity of the system.

$$\vec{J} \,=\, \boldsymbol{\sigma}\,\vec{E} \,=\, \frac{\vec{E}}{\boldsymbol{\rho}} \tag{3.18}$$

since resistivity is the inverse of conductivity. The current density can also be expressed as

$$\vec{J} \,=\, n\,e\,\vec{V} \tag{3.19}$$

which makes it possible to rewrite the expression for the electric field as

$$\vec{E} \,=\, \boldsymbol{\rho}\,\vec{J} \tag{3.20}$$

where both $\boldsymbol{\rho}$ and $\boldsymbol{\sigma}$ are matrices. Going back to eq. 3.17, the matrix found here can be made into the resistivity matrix shown in eq. 3.20 and thus we get:

$$\vec{E} = \begin{bmatrix} \frac{1}{\mu\,n\,e} & \frac{B_z}{n\,e} \\ -\frac{B_z}{n\,e} & \frac{1}{\mu\,n\,e} \end{bmatrix} \begin{bmatrix} J_x \\ J_y \end{bmatrix} \tag{3.21}$$

This results in an expression for the resistivity tensors, that are also referred to as the sheet resistance (found from the classical Drude theory) and the Hall resistance.

$$R_S \,=\, \rho_{xx} \,=\, \rho_{yy} \,=\, \frac{1}{\mu\,n\,e} \,=\, \frac{m}{n\,e^2\,\tau} \tag{3.22}$$

and

$$R_{Hall} \,=\, \rho_{xy} \,=\, -\rho_{yx} \,=\, -\frac{1}{n\,e} \tag{3.23}$$

Where R_S is the sheet resistance, $\rho_{xx} = \rho_{yy} =$ are the longitudinal resistivity tensors, R_{Hall} is the

Hall resistance, and ρ_{xy} and $-\rho_{yx}$ are the transverse resistivity tensors. Eq. 3.23 shows that the Hall resistance is inversely proportional to the electron mobility, meaning that a material with higher electron mobility will have a lower Hall resistance. Hence, a high mobility interface is expected to exhibit a lower Hall resistance. In the case where both the charge carrier density and the electron mobility is unknown, as it is the case for grown materials i.e. GAO/STO, the electron mobility can be extracted experimentally by measuring the Hall resistances and the charge carrier density subsequently found from knowing the mobility. The Hall mobility is derived from assuming that only one band effectively contributes to the mobility.

4 Results and discussion

In this section, the findings obtained through the investigation of the grown GAO/STO heterostructures are presented, employing both structural characterization electrical characterization techniques. The results are presented using data acquired from magnetoresistance (MR) and Hall measurements, x-ray crystallography (XRD, XRR), atomic force microscopy (AFM), scanning electron microscopy (SEM), and reflection high-energy electron diffraction (RHEED). Throughout the presentation, insights are provided into the thought process and decision-making pathway that led to the achievement of high mobility GAO/STO interfaces, offering a clear understanding of the underlying reasoning. The GAO/STO heterostructures will be introduced by their growth parameters and later referred to by their assigned sample names. The sample names are composed by the first few letters of the substrate company provider (Shinkosha), incorporating the batch number (1-25) and the square number (1-9). This results in the format ShinXX_Y. A batch from Shinkosha where the squares has been broken into 9 separate squares is shown in Figure 4.1

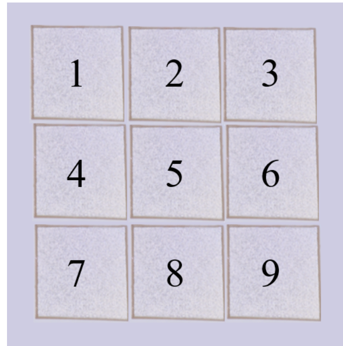

Figure 4.1: Shinkosha "chocolate bar" STO substrate The Japanese company Shinkosha provides 3x3 5x5mm $SrTiO_3$ substrates that have been TiO_2 surface terminated as-recieved. The substrate piece can be broken by hand into 9 equally sized squares.

The primary objective of this project was to produce high mobility GAO/STO heterostructures and conduct electrical and structural characterization. To do so, the specific set of growth parameters that promoted this object had to be identified. Initially, this pursuit resembled a puzzle with numerous unknown pieces. The first part of the picture involved determining how to achieve a somewhat conductive interface. To establish the starting point for the deposition parameters, previous work on GAO/STO interfaces was referenced. However, it should be noted that these parameters were applicable to a different pulsed laser deposition system than the one used in this project. Therefore, even though those parameters successfully yielded a GAO/STO heterostructure with a

mobility of 140,000 cm^2/Vs, their effectiveness for these depositions was not guaranteed. Once a GAO/STO heterostructure exhibited a low sheet resistance, the second part involved fine-tuning the parameters to achieve a set of deposition conditions that facilitated the optimum in concentration of charge carriers for achieving the greatest mobility, while still preventing the heterostructure from becoming 3D conducting.

During the search for favorable growth parameters, which included tuning the background pressure and the laser fluence, numerous small adjustments were necessary to achieve just the right conditions that would ultimately lead to the successful fabrication of the first of several highly mobile GAO/STO heterostructures. The impact, that the aforementioned adjustments, had on the growth of GAO thin films will be elaborated and discussed along side other results in the following sections.

4.1 Pulsed laser deposition growth parameters

This project can be divided into three distinct parts. The first part, which was undeniably the most critical and challenging, focused on growing conducting GAO/STO samples. The second and third part of the project intertwined, combining both structural and electrical characterization. All samples underwent 2-point probe and 4-point probe resistance measurements at room temperature, while selected samples were subjected to low temperature transport measurements and investigated using AFM. Sheet resistance and Hall measurements were employed to determine the charge carrier density and electron mobility, and the growth parameters that yielded the most intriguing results were replicated with longer deposition times for samples that underwent additional structural characterization. The first many GAO/STO samples grown were insulating. This was due to the use of a too low laser fluence (<2 J/cm^2) and too high pressure (1.00 10^{-5} mbar). The laser fluence was increased to range between 3-9 J/cm^2 while the deposition pressure was kept at 1.00 10^{-5} mbar. Still, these growth parameters only resulted in insulating samples.

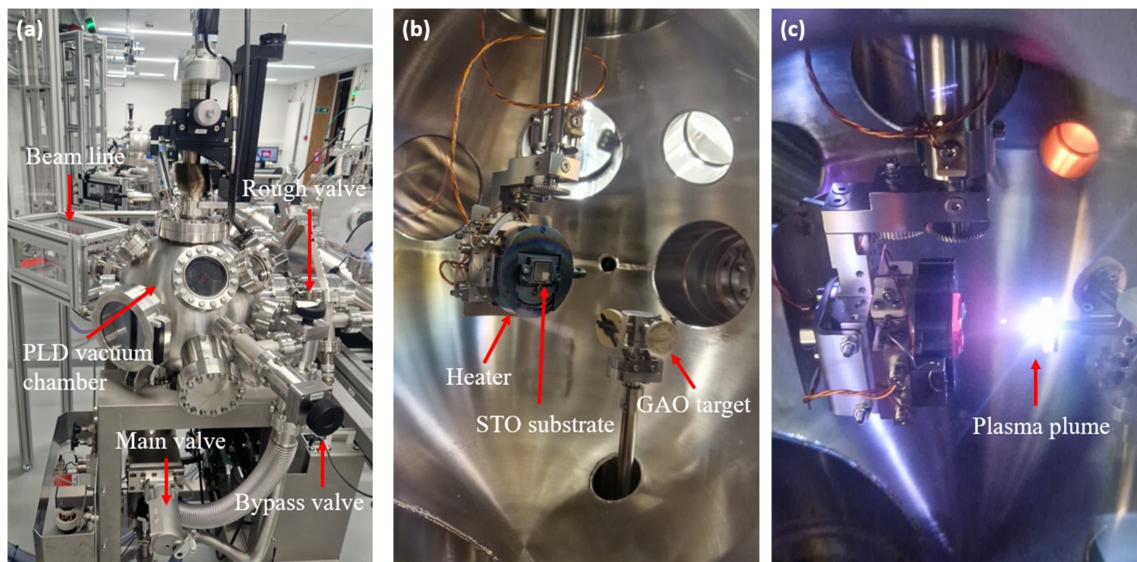

Figure 4.2: PLD chamber a) This image shows the PLD chamber utilized for growing the high mobility GAO/STO heterostructures. The valves used for stabilizing and controlling the background pressure are highlighted with red arrows, specifically the main and bypass valves, connecting to the turbo pump, were used during heat up and cool down to control the background pressure manually. The rough valve connects to the backing pump and was only in use after venting the chamber to gain a pressure below 7.00 10^{-2} mbar. b) Here the heater is shown with a STO substrate after loading. The crystalline GAO target is highlighted by a red arrow as well. c) The image is taken during a deposition where a fluence of 6 J/cm^2 is utilized.

The deposition pressure was then decreased to 1.00 10^{-6} mbar while the laser fluence was set to the highest achievable value at that time, 9.6 J/cm^2. This resulted in the first highly mobile and conductive sample, named Shin12_6. At 15K the charge carrier density was measured to 1.8 10^{15} cm^{-2} with a captivating high mobility of 70,774 cm^2/Vs. Figure 4.2a-c shows images of (a) the PLD chamber used to grow Shin12_6 and the samples to follow, (b) the inside of the chamber with a loaded STO substrate and (c) the deposition of a GAO/STO heterostructure. The choice of decreasing the pressure and increasing the fluence lied in the fact that both adjustments would presumably promote the generation of oxygen vacancies and an interface of higher quality. The selection of deposition parameters was conducted across a range in which the production of conducting GAO/STO heterointerfaces was anticipated. Concurrently, an investigation was carried out to uncover potential correlations between charge carrier density, mobility, and the varied deposition parameters. However, it was not guaranteed that there would be an obvious correlation specifically related to the deposition parameters.

For the samples to follow, the deposition pressure was varied between 1.00-2.00 10^{-6} mbar, while the laser fluence was varied between 3-9 J/cm^2. My efforts were directed towards identifying parameters that, in the end, would potentially yield GAO/STO heterointerfaces with a charge carrier density of $\sim 10^{14}$ cm^{-2} expected to simultaneously achieve an optimum in electron mobility.[38] For all samples, the growth parameters were carefully controlled and a strict protocol depicting the times for pre-ablation of the GAO target, the time of which the substrate was kept (annealed) at the deposition temperature and the time of deposition, to mention a few, were strictly followed for all depositions. Of course, some depositions were flawed due to technical errors which included unstable pressure, blocked laser beam or longer annealing time resulting in experimental uncertainty. The growth parameters are depicted in Table 4.1 and a full list of all times and additional parameters can be found in Appendices in Section 6.2.1 Table 6.2.

Table 4.2 shows a list of some of the grown GAO/STO samples with corresponding growth parameters. The full list of grown samples can be found in the Appendices in Section 6.2. Initially, two sets of GAO/STO samples were selected from the grown samples. One with a deposition pressure variation and one with a fluence variation. The aim was to map the pressure and fluence window where high electron mobility was achievable. Five samples selected for the pressure and fluence window are depicted in Table 4.3. However, in the weeks leading up to the submission deadline, we realized that it would not be feasible to measure all five samples shown in Figure 4.3 within the available time frame. As a result, during the initial resistance assessments (Section 4.3.2),

Parameter	Value
Background gas	Oxygen
Deposition pressure	Varying
Deposition temperature	650 °C
Laser fluence	Varying
Substrate-target distance	450 mm
Pre-ablation time	10 min
Effective dwell time at deposition temperature	11 min
Deposition time	4 min / 30 min
Laser fluence	Varying

Table 4.1: A list of the growth parameters carefully maintained during all depositions. The full list and additional comments on the depositions can be found in the Appendices in Section 6.2 Table 6.2.

Sample	Laser fluence	Pressure	Deposition time
Shin12_6	9.63 J/cm^2	1.00 10^{-6} mbar	4 min
Shin18_7	9.12 J/cm^2	1.00 10^{-6} mbar	4 min
Shin18_9	6.05 J/cm^2	1.00 10^{-6} mbar	4 min
Shin18_4	3.1 J/cm^2	1.00 10^{-6} mbar	4 min
Shin18_1	9.22 J/cm^2	1.50 10^{-6} mbar	4 min
Shin18_2	9.29 J/cm^2	2.00 10^{-6} mbar	4 min
Shin18_8	9.12 J/cm^2	2.00 10^{-6} mbar	4 min

Table 4.2: Grown GAO/STO samples with corresponding laser fluence and deposition pressure. A full list of all samples grown as a result of Shin12_6 can be found in the Appendices in Section 6.2.1 Tables 6.3 and 6.5

we prioritized four samples in order to maximize the chances of obtaining data on high mobility. Further details on this selection process and its outcomes are discussed in Section 4.3 and subsequent sections. As mentioned, after favorable growth parameters were discovered, thicker thin films were grown for the purpose of structural characterization utilizing x-ray crystallography, AFM and SEM. The GAO/STO samples and corresponding growth parameters are depicted in Table 4.9.

The laser spot size was optimized and measured as a part of optimizing the PLD setup. The spot size optimization can be seen in Appendices in Section 6.8.3 Figure 6.40.

Pressure \ Fluence	9 J/cm^2	6 J/cm^2	3 J/cm^2
1.00 10^{-6} mbar	Shin18_7	Shin18_9	Shin18_4
1.50 10^{-6} mbar	Shin18_1	-	-
2.00 10^{-6} mbar	Shin18_8	-	-

Table 4.3: Two series of data sets were selected for thorough investigation by transport measurements and structural characterization. The first series was intended to investigate the pressure dependency of GAO/STO heterostructures grown utilizing a fluence of 9 J/cm^2. The second series was intended to investigate the fluence dependency of GAO/STO heterostructures grown utilizing a deposition pressure of 1.00 10^{-6} mbar. All samples were grown with a deposition time of 4 minutes.

Sample	Pressure	Laser fluence	Deposition time
Shin23_3	1.00 10^{-6} mbar	3 J/cm^2	30 min
Shin23_4	1.00 10^{-6} mbar	3 J/cm^2	30 min
Shin20_5	1.00 10^{-6} mbar	6 J/cm^2	30 min
Shin20_9	1.00 10^{-6} mbar	6 J/cm^2	30 min
Shin20_6	1.00 10^{-6} mbar	9 J/cm^2	30 min
Shin20_8	1.00 10^{-6} mbar	9 J/cm^2	30 min

Table 4.4: GAO/STO samples grown for the purpose of x-ray crystallographic analysis. The samples were grown with a deposition time of 30 minutes.

4.2 Structural characterization and growth rate estimation

The structural characterization of the grown GAO/STO heterostructures started with an investigation of the thermally annealed STO substrates using AFM. The quality and crystallinity of the substrate surface was deemed critical, as any significant defects would compromise the growth of the GAO thin films. To iterate from the methods section, the STO substrate surface ideally consist of well-defined atomically sharp terraces of TiO_2. Examples of defects may include double terminated surfaces resulting in extra steps (i.e. terraces), large holes or other structures that do not belong on the substrate surface. Such defects may compromise the thin film growth or introduce scattering sites and thereby lead to undesired non-conducting interfaces. Once the heterostructures were grown, it was crucial to perform a thorough evaluation of the thin film surface using the aforementioned structural characterization techniques (i.e. AFM, X-ray crystallography and SEM). This assessment played a vital role in determining the structural quality of the thin film, that is if the thin film had been deposited uniformly, if GAO had been expitaxially grown on STO, if the thin

film was crystalline, and to detect any defects that may have occurred during deposition.

Although structural characterization alone does not provide a definitive assessment of the thin film homogeneity, a comprehensive electrical characterization, which includes Van der Pauw resistance measurements, can offer a coherent understanding of the interface formation during growth. Hence, the results presented in this section will be compared side-by-side with the subsequent findings of the electrical characterization, allowing for a more detailed discussion and comparison. Consequently, the following sections present and analyze the outcomes of the structural characterization. A summary of the conclusions derived from the structural characterization will conclude the section.

4.2.1 Atomic force microscopy

AFM was employed to assess the quality of the STO substrates before deposition and examine the local crystallinity of the GAO/STO thin films. As outlined in the beginning of the methods section, AFM proves to be a valuable tool for obtaining crucial information regarding the surface topography, morphology, and roughness of thin films. In particular, the morphology and roughness were of significant interest for both the 4-minute and 30-minute depositions. This section will present representative AFM images showcasing the STO substrates before deposition and the GAO/STO thin films. This includes AFM images of the thin films specifically produced for transport measurements (4-minute depositions) as well as the thin films generated for growth rate determination (30-minute depositions).

The STO substrates were examined prior to deposition, revealing distinct terraces on all investigated substrates. It was crucial to document the initial state of each substrate batch for future reference and comparison with the subsequently deposited samples. Figure 4.3a-c shows three STO substrates manufactured by Shinkosha. The substrate illustrated in Figure 4.3a is an individual 5x5 mm STO substrates originating from an unknown batch and exhibits noticeable linear terraces compared to the substrates shown in Figures 4.3b and 4.3c, which were employed for the depositions of Shin18-9 and Shin20-1, respectively. This example highlights the variability in step width, step edge sharpness, and overall appearance that can be observed among STO substrates.

After deposition, the GAO/STO heterostructures were imaged a second time. Figure 4.4a-b shows an AFM image of Shin20_1. Shin20_1 was deposited for 4 minutes using a laser fluence of 6 J/cm^2 and a deposition pressure of 1.50 10^{-6} mbar. Figure 4.4a shows an AFM image measuring a 10x10 μm area approximately in the center of the sample. Some impurities has been collected on the surface, which may have been accumulated as a result of handling the sample. The terraces

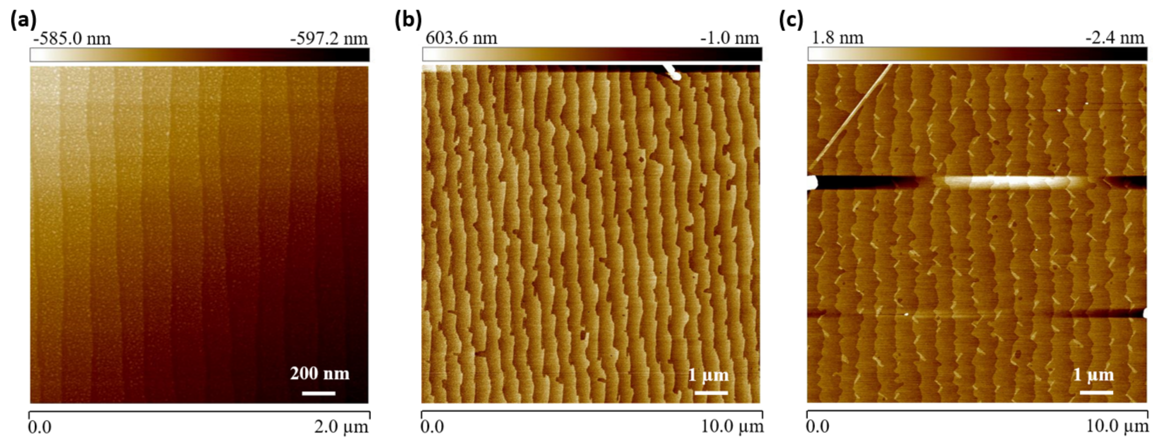

Figure 4.3: Atomic force microscopy of STO substrates a) 2x2 μm AFM image of individual STO substrate from an unknown batch. b) 10x10 μm AFM image of STO substrate originating from the Shin18 batch. The substrate was used for the deposition of Shin18-9. c) 10x10 μm AFM image of STO substrate originating from the Shin20 batch. The substrate was used for the deposition of Shin20-1.

can very clearly be spotted which is the first clue of crystalline and epitaxial growth of GAO on STO. Figure 4.4b shows a 2x2 μm area of the same part of the sample. Here, the terraces are still defined but have a more crude look as compared to the clean STO substrates. This is due to the structure of GAO, which even though it is epitaxial grown, is still not a perfect crystalline thin film. In general, no major defects were spotted on any of the 4 minutes deposited GAO/STO samples and terraces were visible on all of the imaged samples. A collection of AFM imaged STO substrates and GAO/STO heterostructures (both 4 and 30 minute depositions) is available in the Appendices in Sections 6.3.2 and 6.3.3, respectively.

Longer depositions of 30 minute duration were conducted to produce thin films suitable for x-ray crystallography. These samples were imaged using AFM as well. Here it becomes clear that both fluence and thin film thickness had a great influence on the surface morphology of the film. Figure 4.5a shows the AFM image of Shin20_6. Shin20_6 was deposited for 30 minutes using a laser fluence of 9 J/cm^2 and a deposition pressure of 1.00 10^{-6} mbar. Despite the longer deposition time, resulting in a significant greater thin film thickness, the terraces from STO can still be sensed as vague tilted vertical lines. The high laser fluence induces plasma species with exceptionally high kinetic energy, leading to the formation of a thin film with still some degree of crystallinity. In contrast, Shin23-3, lacks discernible terraces which indicates a much more amorphous structure. Figure 4.5b shows the AFM image of Shin23-3, which was deposited utilizing identical pressure and

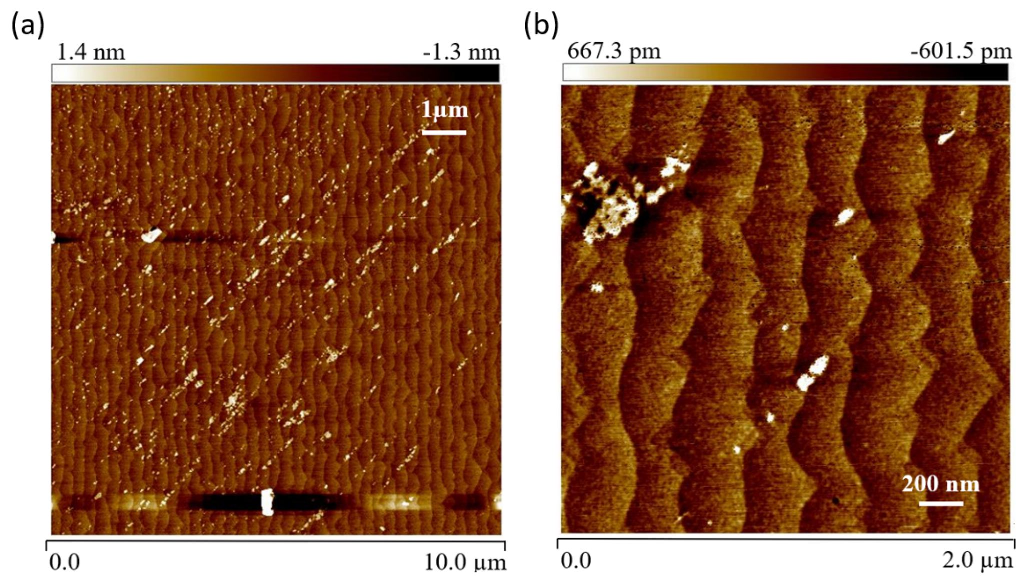

Figure 4.4: Atomic force microscopy of Shin20-1 Shin20-1 was deposited for 4 minutes, with a deposition pressure of 1.50E-06 mbar and a laser fluence of 6 J/cm^2. a) 10x10 μm AFM image of the center of Shin20-1. b) 2x2 μm AFM image of the bottom part of the 10x10 μm image.

deposition time as Shin20-6, but with a lower fluence of 3 J/cm^2. The lower laser fluence results in GAO plasma species of equally lower kinetic energy, which consequently may be thought to result in a less crystalline surface. While the crystallinity of the interface can be expected to remain unaffected, the surface appearance of the GAO thin film does exhibit a change as its thickness increases. A more detailed examination of the crystallinity and thin film thickness was conducted using x-ray crystallography. The findings, specifically on Shin20-6 and Shin23-3, are presented in section 4.2.3. AFM images of the investigated GAO/STO samples can be reviewed in the appendices, section 6.3.

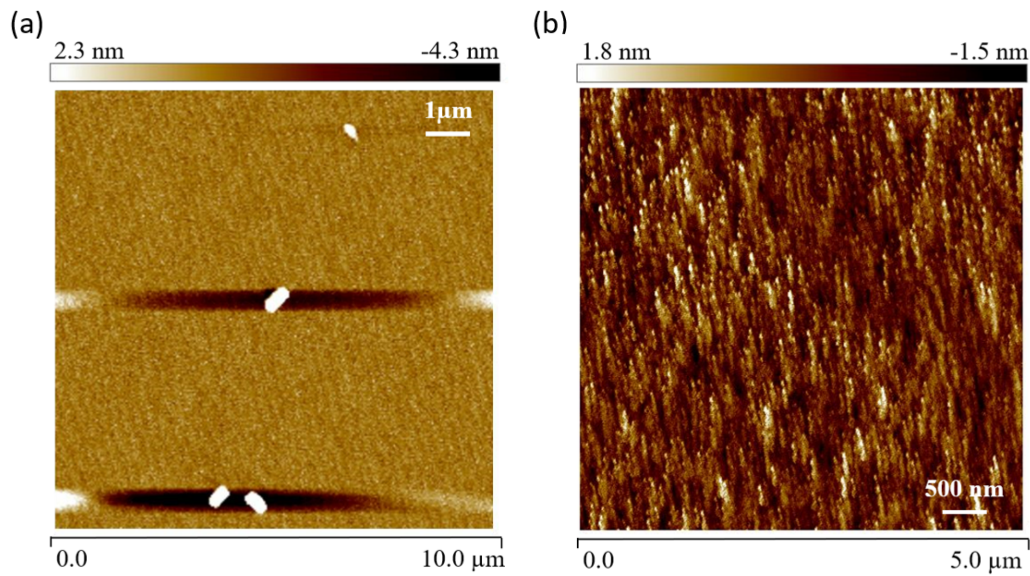

Figure 4.5: Atomic force microscopy of Shin20-6 and 23-3 a) 10x10 μm AFM image of Shin20-6. The GAO/STO sample was deposited for 30 minutes, with a deposition pressure of 1.00E-06 mbar and a laser fluence of 9 J/cm^2. b) 5x5 μm AFM image of Shin23-3. The GAO/STO sample was deposited for 30 minutes, with a deposition pressure of 1.00E-06 mbar and a laser fluence of 3 J/cm^2.

In an effort to measure the thickness of the GAO thin films, an attempt was made using AFM. A stainless steel mask was affixed to the STO substrate using silver paste and GAO was deposited on top. Figure 4.6 shows an optical microscopy image of Shin7-2, the first attempt out of three. GAO was deposited for 72 minutes using a laser fluence of 3.6 J/cm^2 and a deposition pressure of 9.94 10^{-6} mbar. This deposition, and the two to follow, was conducted with a background pressure that was later found to only produce insulating interfaces (i.e. the aforementioned 1.00 10^{-5} mbar). Note that the decision to decrease the pressure and increase the fluence was made as a result of several unsuccessful depositions utilizing the growth parameters used for these aforementioned GAO/STO samples. Previous studies have employed AFM for estimating thin film thickness by placing a mask on the substrate and measuring the height difference using AFM. The objective was to estimate the thin film thickness and determine the growth rate to accurately determine the number of deposited GAO unit cells. However, this task proved to be extremely challenging due to the absence of sharp edges in the thin film. Consequently, as the edges were not sharp but rather decreasing in height over several microns, the AFM approach was not possible. Due to the inability to achieve precise height measurements, it was determined that growing dedicated GAO/STO samples for x-ray crystallography was necessary to investigate the growth rate accurately. This decision was primarily

Figure 4.6: Optical microscopy image of Shin7-2 Shin7-2 was among the three samples in which a titanium mask was employed in an effort to fabricate a GAO thin film for AFM measurements. The pattern on the sample reveals the precise location of the mask, signifying that the STO surface underwent screening during the ablation process. The objective was to utilize AFM to measure the heights of the edges, particularly the edges that define the squares in the center.

influenced by the challenges faced in obtaining precise height measurements with AFM as well as the absence of RHEED. Additionally, the samples dedicated for x-ray crystallography was grown using deposition parameters that had been proved to produce highly conductive and mobile GAO/STO interfaces.

4.2.2 Reflection high energy electron diffraction

The initial depositions were conducted in a PLD chamber equipped with RHEED. Monitoring the growth of GAO on STO was essential for several reasons. Firstly, the production of a heteroepitaxial interface was of utmost importance since any non-epitaxial thin films would not yield the emergence of the highly mobile 2DEG that is the primary objective of this masters project. Secondly, tracking the progress through the number of RHEED oscillations provided a direct measure of the number of deposited unit cells at a given time. Previous studies conducted on this subject indicated an ideal thickness of 2.5 - 3.5 uc. This section treats the initial RHEED data collected on the very first depositions. The data was used afterwards as a measure to decide on the standardized deposition time.

The RHEED data depicted in this section originates from the deposition of R2. The STO substrate used for R2 was provided by Shinkosha and was a single 5x5 substrate from an unknown batch. R2 was deposited with a laser fluence of 1.6 J/cm^2 and a deposition pressure of 1.00 10^{-5} mbar. Figure 4.7a-d shows RHEED patterns obtained before (Figure 4.7a-b) and after (Figure 4.7c-d) deposition

of R2. The RHEED patterns observed from the utilized STO substrate prior to deposition exhibit a resemblance to the expected patterns for STO. Figure 4.7a shows the primary specular spot (central large spot) before it was separated to two smaller diffraction spots. The separation of the primary specular spot is a result of the change in incidence angle, which in turn facilitates visibility of layer-by-layer GAO unit cell growth. Figure 4.7b shows the RHEED pattern after correcting the incidence angle such that the primary specular spot was separated into two distinctive spots. The specular spot to the left (marked with a blue arrow) corresponds to the expected intensity signal from electrons diffracted during the growth of GAO. The spot to the right (marked with a black arrow) corresponds to the intensity signal originating from Kikuchi lines. The secondary specular spots (on either side of the primary specular spot) can be seen in both Figures 4.7a and b along with the Kikuchi lines. Before proceeding with the deposition, markers were placed on the specular spots and the background such that the RHEED intensities could be monitored. The markers can be seen in Figure 4.7d showing the RHEED pattern post deposition. Figure 4.7c shows the same image but without markers, where the different diffraction spots can be seen more clearly. The markers in Figure 4.7d each corresponds to a RHEED intensity signal monitored during deposition, presented in Figure 4.8a.

At the time when the RHEED data was collected, my experience in setting up RHEED and adjusting the incident beam angles to obtain a clear pattern on the substrate surface was limited. It was necessary to position precise and small-sized markers accurately in order to prevent noise or signal interference in the RHEED detector. Despite careful marker placement, there were occasions when the collected data displayed mixed intensity signals or low amplitude signals, making the RHEED oscillations unreadable.

Figure 4.8a-b displays the RHEED data of the R2 GAO/STO heterostructure, which represents the sole instance where distinct RHEED oscillations were successfully obtained, enabling effective monitoring of GAO growth. The purple colored RHEED intensity, depicted in both Figures 4.8a and b, represents the direct monitoring of layer-by-layer growth of GAO. The initial intensity increase represented the first 1/4 layer of GAO uc. The marker associated with this intensity was located at the specular spot depicted to be the signal of the (004) plane of GAO. One RHEED oscillation was found to have an average period of 15 seconds. The duration between the first and last oscillation, spanning a total of fourteen oscillations, was calculated to be approximately 204.5 seconds or 3 minutes and 24 seconds. This corresponds to a growth rate of approximately 8 Å/min, slightly

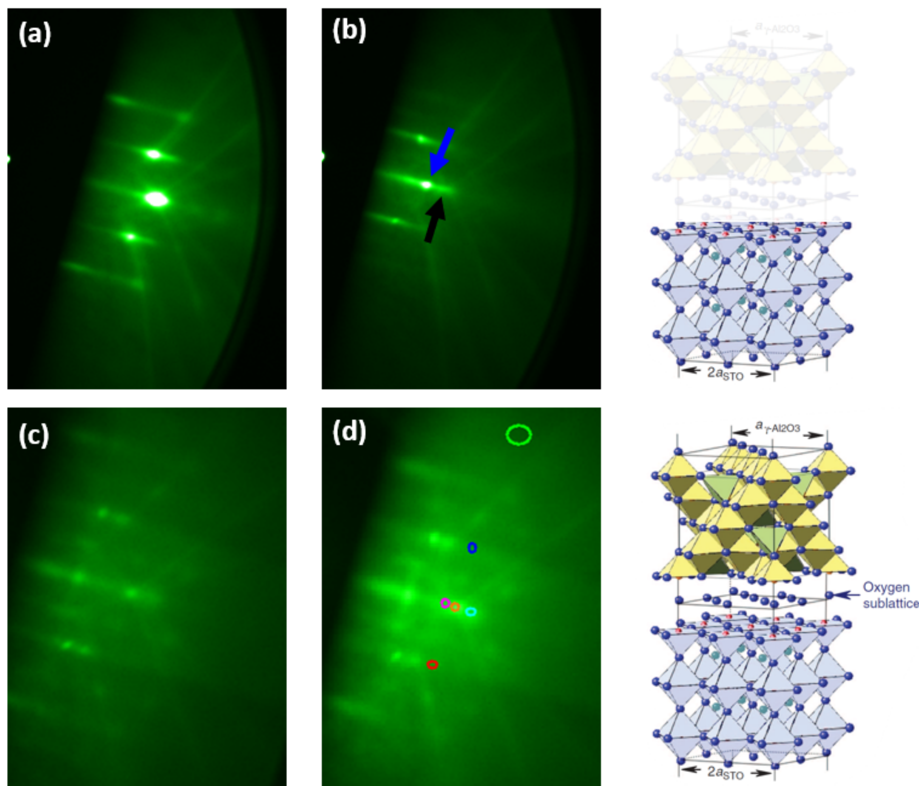

Figure 4.7: RHEED patterns before and after deposition of GAO on STO a) and b) shows the RHEED diffraction patterns of the STO substrate prior to deposition. The primary specular spot centered in a) has been split in b) by changing the incidence angle. The blue arrow highlights the expected specular spot of GAO. The black arrow highlights the expected diffraction signal from Kikuchi lines. c) and d) shows the RHEED diffraction pattern of R2 after deposition. d) shows the RHEED pattern with the markers for detecting RHEED intensities. The colors of the markers each corresponds to a recorded RHEED intensity in Figure 4.8a.

exceeding the growth of one uc of GAO per minute, considering that one uc is equivalent to 7.911 Å. Figure 4.8b illustrates the 1/4 uc GAO oscillations, with the first and fourteenth oscillations highlighted by arrows. Here, an intriguing observation arose when comparing the purple RHEED signal to the turquoise RHEED signal. In Figure 4.7d, the turquoise marker was positioned opposite the purple marker, with an orange marker in between. The turquoise RHEED intensity exhibited two distinct oscillations. Further investigation revealed that the period of each oscillation was approximately 64 seconds. Dividing this period by 4 demonstrated that one turquoise oscillation corresponded to four purple oscillations, indicating that the turquoise oscillation represented the (001) plane of GAO, reflecting the growth of the complete unit cell. Both the turquoise and purple

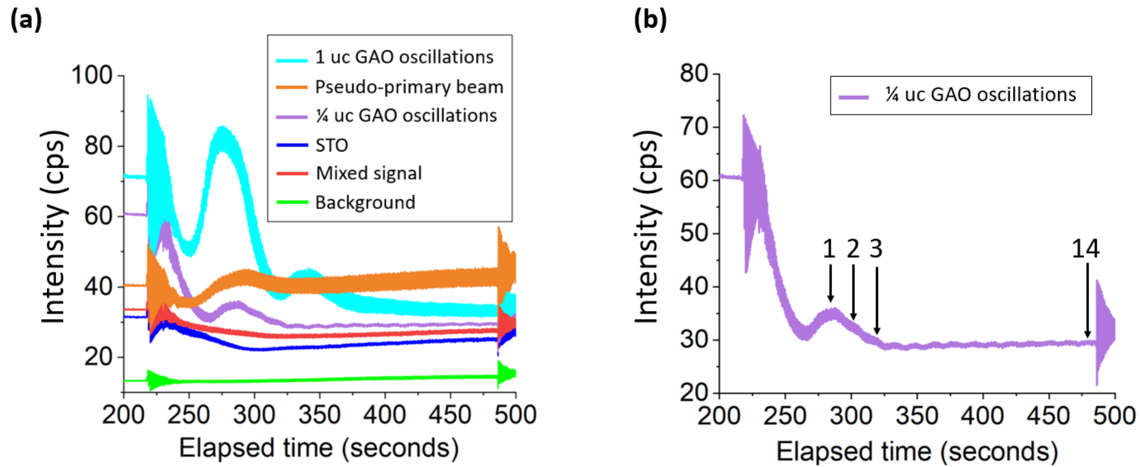

Figure 4.8: RHEED data for RHEED intensities collected during the depostion of R2. R2 was deposited using a laser fluence of 1.6 J/cm^2 and a background pressure of 1.00 10^{-5} mbar. a) Each RHEED intensity corresponds to a marker on the RHEED pattern (Figure 4.7d). The graph illustrates the RHEED intensity plotted as a function of elapsed time. The RHEED intensity associated with the primary specular spot is highlighted in purple where each oscillation equals 1/4 uc GAO. The turquoise highlighting represents 1 full uc GAO per RHEED oscillation. b) The distinct GAO RHEED oscillations displayed clear periodic behavior. These oscillations were utilized to estimate the required time to achieve the desired number of unit cells during the growth process.

RHEED signals exhibited a shared characteristic of an initial decrease in intensity followed by a significant increase (between 225 and 275 seconds). The intensity decrease was interpreted as a consequence of sudden increased disorder upon the arrival of the first GAO plasma species at the STO surface. As the initial 1/4 charge-neutral layer of GAO formed, order was established, resulting in constructive interference and an overall elevation in RHEED intensity. Subsequently, the turquoise RHEED intensity gradually declined over the subsequent 3/4 of the GAO unit cell since electrons diffracted of planes other than the (001) plane of GAO would not result in constructive interference.

In Figure 4.7d, positioned between the purple and turquoise markers, is an orange marker. Examining Figure 4.8a, the orange RHEED intensity demonstrates a growth pattern similar to that observed in the RHEED signals corresponding to GAO growth. Initially, the intensity shows an increase at a comparable rate. Subsequently, there is a slight decrease followed by a relatively constant intensity signal throughout the deposition process. As explained in the Methods Section 4.2.2, this signal is inherently associated with the phase and structural disparities between the crystal structures of STO and GAO. The diffracted electrons within the region of the orange marker behave as a pseudo-primary beam, resulting from the intersection of Kikuchi lines.

Upon further examination of the RHEED intensities presented in Figure 4.8a, the presence of the blue and red intensities becomes apparent. The blue RHEED intensity demonstrated a consistent decrease in signal, stabilizing around the initial peak of the GAO RHEED intensities. This can be attributed to the (001) plane of STO. As GAO is deposited onto the STO surface, the RHEED probing depth eventually exceeds the thickness of the STO layer, making it difficult to detect electrons diffracted from STO. In Figure 4.7d, a closer look at the red and blue markers reveals that the red marker was positioned slightly closer to the RHEED source compared to the blue marker. As a result, the red RHEED intensity may represent a mixed signal containing electrons diffracted from STO as well as electrons diffracted from other planes. The final green RHEED signal corresponds to the background signal and exhibits a low and constant intensity, aligning with expectations.

Shortly after the deposition of R2, a decision was made to switch to another PLD chamber. Although this new chamber lacked RHEED, it offered more available booking time and featured manually controlled pressure valves. The latter proved to be a significant advantage as it allowed for more precise regulation of the background pressure. As described in the methods section, precise control of the background pressure is crucial for achieving highly mobile interfaces. The protocol that was used to grow the initial high mobility GAO/STO heterostructures (Christensen et al. in 2016 and Chen et al. in 2013) was originally optimized for a different PLD system and laser. Additionally, the STO substrate and GAO target used in this project differed from those utilized in the original experiments. It is important to note that each PLD chamber is unique, and parameters that yield desired results in one experiment may not necessarily be applicable to another chamber. The same principle applies to the choice of substrates, targets, laser optics, and substrate preparations. Therefore, it was not anticipated that the selected parameters would work on the first attempt, and indeed, several parameter adjustments were required before the first successfully highly mobile and conducting GAO/STO heterostructure were grown. The standardized deposition time, applied on the GAO/STO heterostructures to follow, was estimated by counting the number of RHEED oscillations seen in Figure 4.8b during the deposition and then calculating the time it took to get that number of oscillations. Drawing from the previous work by Christensen et al. in 2016,[62] the intended thickness was set to 3.5 uc of GAO and thus 14 oscillations were counted before ending the deposition of R2.

To summarize, the RHEED data presented here is of a GAO/STO sample grown using a fluence of 1.6 J/cm^2. In contrast, the fluences used to grow the conducting GAO/STO heterostructures ranged

from 3-9 J/cm^2. The lower fluence of 1.6 J/cm^2 compared to the higher fluences was anticipated to lead to a considerably slower growth rate. This was explored further at a later time, when the correlation between growth rate and fluence was investigated using x-ray crystallography. This is discussed in section 4.2.3 and did in fact confirm that a higher fluence led to an increased growth rate. The RHEED data showed that the desired thin film thickness of 3.5 uc could be achieved in less than 4 minutes. Nevertheless, the deposition time was standardized to 4 minutes for all subsequent depositions. This was due to the fact that the depositions would take place in a different PLD chamber and that both the fluence and background pressure would be changed significantly. Specifically, the background pressure utilized for the deposition presented in the RHEED data was 10^{-5} mbar whereas all subsequent GAO/STO heterostructures would be deposited in a background pressure of 10^{-6} mbar, This difference in pressure also exerts a significant impact on the growth rate. Consequently, considering the combination of factors including the change of PLD chamber, the increased laser fluence, and the decreased background pressure, the deposition time of 4 minutes was established to ensure the attainment of a GAO thin film exceeding 2 nm, i.e. the critical thickness necessary to achieve a stable conductive GAO/STO interface.

4.2.3 X-ray crystallography

In the absence of RHEED, there was a need to explore alternative methods for investigating the thickness and crystallinity of GAO. To address this need, I turned to x-ray crystallography and employed the technique on samples specifically grown for this purpose.

As mentioned in the methods section 3.2.3 is x-ray crystallography a powerful technique that provides valuable insights into the structural characteristics of materials, particularly in combination with other structural characterization techniques such as AFM and RHEED. However, to perform a simple x-ray diffraction measurement, the investigated sample must possess a certain degree of crystallinity. Specifically, I focused on six GAO/STO heterostructures dedicated to x-ray crystallography analysis. The thin films were carefully chosen to ensure a higher likelihood of obtaining measurable samples, with two films prepared for each fluence. The GAO/STO heterostructures were grown with varying fluences of 3 J/cm^2, 6 J/cm^2 and 9 J/cm^2, all at a deposition pressure of 1.00 10^{-6} mbar and deposition time of 30 minutes. As proved by AFM, only the samples grown at 9 J/cm^2 possessed some level of ordered atomic arrangement. However, AFM provides a microscopic perspective limited to the surface of the thin film. XRD and XRR should come to prove that the

Sample	Pressure	Laser fluence	Thickness	Growth rate
Shin23_3	1.00 10^{-6} mbar	3 J/cm^2	16.8 nm	0.56 nm/min
Shin23_4	1.00 10^{-6} mbar	3 J/cm^2	n/a	n/a
Shin20_5	1.00 10^{-6} mbar	6 J/cm^2	n/a	n/a
Shin20_9	1.00 10^{-6} mbar	6 J/cm^2	n/a	n/a
Shin20_6	1.00 10^{-6} mbar	9 J/cm^2	34.7 nm	1.16 nm/min
Shin20_8	1.00 10^{-6} mbar	9 J/cm^2	n/a	n/a

Table 4.5: GAO/STO samples grown for the purpose of x-ray crystallographic analysis. The samples were grown with a depostion time of 30 minutes.

thin films possessed a significant degree of crystallinity at a macroscopic scale such that Bragg peaks would show in XRD. Out of the six samples examined, two exhibited minimized interface roughness, enabling the observation of Kiessieg fringes in XRR. The detection of Kiessieg fringes allowed for an estimation of the thin film thickness.

Considering that the deposition duration was limited to only 4 minutes, it was expected that the resulting thin films would have a thickness that would not exceed 5-10 nm, even with the highest fluence of 9 J/cm^2. In order to obtain reliable XRD and XRR data, the GAO thin films needed to surpass a thickness of $\sim$15 nm. To achieve thicker films, the deposition time was extended from 4 minutes to 30 minutes. This decision was based on previous XRD measurements conducted on the patterned Shin7_4 (showed in Figure 4.6), as a consequence of unsuccessful attempts to measure it using AFM. The XRD analysis revealed that the central region of the thin film had a thickness of $\sim$73 nm, achieved through a 72-minute deposition using a laser fluence of 3.6 J/cm^2 and a deposition pressure of 9.94 10^{-6} mbar. Supplementary data is presented in Section 6.5.2 Figure 6.27.

Section 4.1 mentions the growth parameters and how these were adjusted to promote the formation of high-mobility interfaces. To iterate, the modifications included reducing the deposition pressure to a range of 1.00-2.00 10^{-6} mbar and varying the laser fluence between 3-9 J/cm^2. Consequently, GAO/STO heterostructures for the purpose of x-ray crystallographic analysis were fabricated, incorporating the aforementioned fluence variations while maintaining a deposition pressure of 1.00 10^{-6} mbar. The deposition time was set to 30 minutes, which was estimated to yield GAO thin films ranging in thickness from approximately 20 nm to 50 nm.

Oxide	hkl	2θ
STO	001	22.753
	002	46.472
GAO	004	45.845

Table 4.6: The calculated reference peak positions for STO (001 and 002) and GAO (004). hkl refers to Miller indices. d is the lattice constant for the designated plane. θ is the diffraction peak in radians. 2θ is the diffraction peak position in degrees. The values are calculated from using Bragg's law.

Prior to performing x-ray crystallography, it is advisable to pre-calculate the anticipated 2θ values for each material considering the potential crystallographic orientations. Table 4.6 depicts the expected 2θ values for STO and GAO, specifically the (001) and (002) plane for STO, and (004) plane for GAO. Figures 4.9, 4.10 and 4.11 presents XRD and XRR data of Shin23_3, Shin20_5 and Shin20_6, respectively. Bragg peaks belonging to the (001) and (002) planes of STO, and (004) plane of GAO were present for all samples, including samples not presented in this section. The data of Shin20_8, Shin_9 and Shin23_4 is presented in the Appendices in Section 6.5.2 Figures 6.28, 6.29 and 6.30, respectively. The presence of the aforementioned Bragg peaks instantly yielded insights into the crystal structure, lattice parameters, crystallographic orientation, and degree of crystallinity. Particularly, by comparing the actual 2θ values for each peak with the calculated values, it became possible to detect the strain effects exerted by the growth of GAO on STO on the respective lattice parameters. This will be elaborated and discussed later on in this section.

In all samples, a consistent observation was made that the Bragg peak associated with (001)STO occurred at approximately $2\theta \sim 23$ degrees, while the Bragg peak of (002)STO was observed around $2\theta \sim 46$ degrees. This correlation was expected since both the (001) and (002) planes are perpendicular to the incident x-rays, indicating that both orientations should be visible in a $2\theta/2\theta$ scan. Furthermore, the estimated position of the (004)GAO Bragg peak was calculated to be at $2\theta=45.8$ degrees (i.e. Table 4.6). All samples exhibited a distinct peak just preceding the (002)STO peak, of which 2θ value aligned with the predicted (004)GAO peak position. All peak values are listed in the Appendices in Section 6.5.2 Table 6.7.

Figures 4.9a-c shows the XRD (a and b) and XRR (c) measurements of Shin23_3. This sample was produced utilizing a laser fluence of 3 J/cm^2. In Figure 4.9a, the Bragg peaks have been associated with their respective crystallographic orientations in STO and GAO. Additionally, Figure 4.9b presents a fine scan of the (004)GAO peak, revealing its broad nature and the presence of

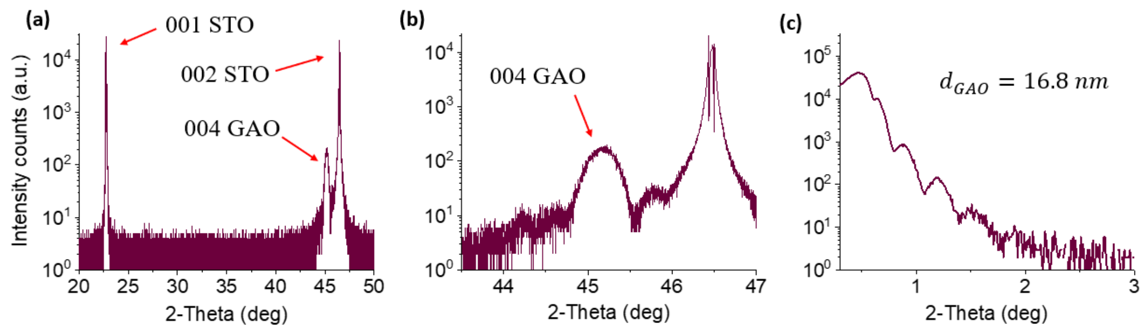

Figure 4.9: X-ray crystallography of Shin23_3 Shin23_3 was deposited for 30 minutes using a laser fluence of 3 J/cm^2 and a deposition pressure of 1.00 10^{-6} mbar. a) X-ray diffraction intensity counts as a function of 2θ for 20-50 2θ. Bragg peaks belonging to (001) and (002) STO, and (004) GAO are highlighted with red arrows. b) X-ray diffraction intensity counts as a function of 2θ for 43-47 2θ. The broad Bragg peak of (004) GAO is highlighted by a red arrow. c) X-ray reflectometry intensity counts as a function of 2θ for 0-3 2θ. The thickness of Shin23_3 was estimated from the period of Kiessig fringes to be 16.8 nm.

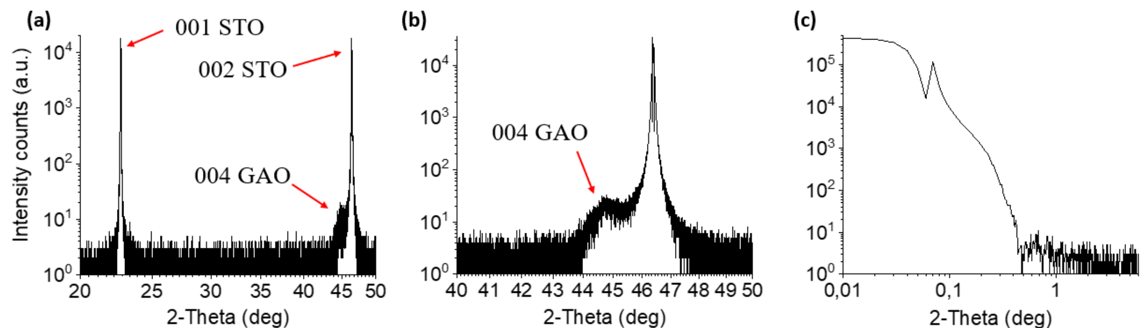

Figure 4.10: X-ray crystallography of shin20_5 Shin20_5 was deposited for 30 minutes using a laser fluence of 6 J/cm^2 and a deposition pressure of 1.00 10^{-6} mbar. a) X-ray diffraction intensity counts as a function of 2θ for 20-50 2θ. Bragg peaks belonging to (001) and (002) STO, and (004) GAO are highlighted with red arrows. b) X-ray diffraction intensity counts as a function of 2θ for 40-40 2θ. The small Bragg peak of (004) GAO is highlighted by a red arrow. c) X-ray reflectometry intensity counts as a function of 2θ for 0-2 2θ. The thickness of Shin20_5 could not be estimated due to the lack of Kiessig fringes.

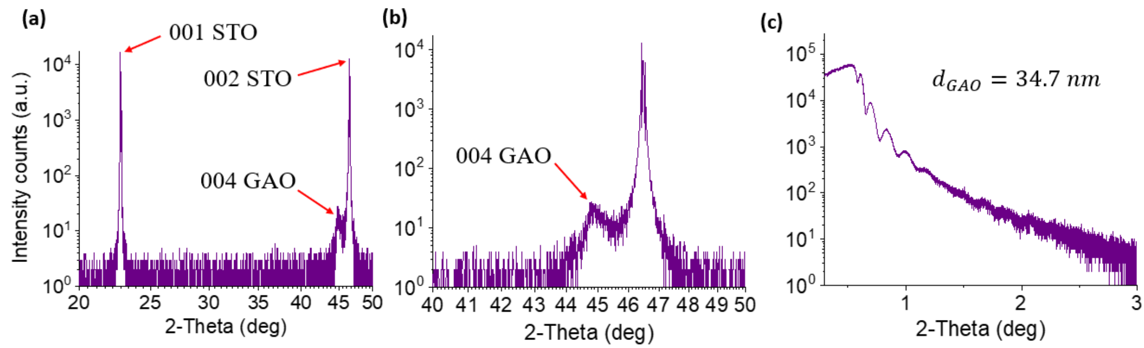

Figure 4.11: X-ray crystallography of shin20-6 Shin20_6 was deposited for 30 minutes using a laser fluence of 9 J/cm^2 and a deposition pressure of 1.00 10^{-6} mbar. a) X-ray diffraction intensity counts as a function of 2θ for 20-50 2θ. Bragg peaks belonging to (001) and (002) STO, and (004) GAO are highlighted with red arrows. b) X-ray diffraction intensity counts as a function of 2θ for 40-50 2θ. The small Bragg peak of (004) GAO is highlighted by a red arrow. c) a) X-ray reflectometry intensity counts as a function of 2θ for 0-3 2θ. The thickness of Shin20_6 was estimated from the period of Kiessig fringes to be 34.7 nm.

surrounding oscillations. While these oscillations may resemble weak Laue oscillations, only three of them are visible enough to be counted accurately. As a result, these oscillations could not be utilized for determining the thickness of the GAO thin film. Nevertheless, it is noteworthy that this peak is more well-defined and prominent in comparison to the (004)GAO Bragg peaks observed in the other samples.

The characteristics of the Bragg peaks observed in Shin20_5 and Shin20_6 exhibited remarkable similarities in terms of shape, peak broadness, and intensity. To reiterate, Shin20_5 and Shin20_6 were deposited using fluences of 6 J/cm^2 and 9 J/cm^2, respectively. Figures 4.10a-c and 4.11a-c presents the XRD (a and b) and XRR (c) data of Shin20_5 and Shin20_6, respectively. In Figure 4.11b, the (004)GAO Bragg peak of Shin20_6 appeared slightly sharper, but overall, there were no significant differences between the two samples. However, XRR revealed the greatest difference between all samples. Kiessig fringes were detected in only two samples, specifically Shin20_6 and Shin23_3 (depicted in Figure 4.9c and 4.11c), while the remaining samples exhibited an absence of Kiessig fringes. This absence was likely due to significant interface roughness, leading to destructive interference. Figure 4.10c illustrates this scenario for Shin20_5. Recalling that reflectometry provides insights into interface/surface roughness, thickness, and density, the period between the distinct Kiessig fringes observed in Shin23_3 and Shin20_6 was utilized to estimate the thickness of the GAO thin film. For Shin23_3, which employed a deposition fluence of 3 J/cm^2, the estimated thickness was 16.8 nm, corresponding to a growth rate of 0.56 nm/min. Thus, for GAO/STO

heterostructures grown for 4 minutes using a fluence of 3 J/cm^2 and a deposition pressure of 1.00 10^{-6} mbar, a thickness of 2.25 nm for the GAO thin film was obtained. Comparatively, Shin20_6, utilizing a fluence of 9 J/cm^2 during deposition, yielded a thickness of 34.7 nm, corresponding to a growth rate of 1.16 nm/min. Consequently, a 4-minute deposition would result in a 4.63 nm thick GAO thin film. Notably, the Kiessig fringes observed in Shin20_6 were more pronounced than those in Shin23_3, indicating that a higher laser fluence reduces interface roughness. The abundance of fringes in Shin20_6 suggests a more consistent thickness and density of the GAO thin film across the interface. In contrast, the limited and indistinct Kiessig fringes in Shin23_3 indicate a rougher or more irregular interface, likely resulting from variations in thin film thickness or density, as well as increased surface roughness or growth defects. It is plausible that an increased laser fluence enhances interface homogeneity, as observed in this case, rather than a lower fluence inducing defects. Unfortunately, neither of the two samples deposited with a fluence of 6 J/cm^2 could be measured using XRR. There is no apparent reason for this issue other than the presence of excessive interface roughness, rendering the measurements impractical. The findings regarding the potential influence of laser fluence on crystallinity, interface roughness, and thin film quality align with the microscopic perspective obtained through AFM analysis. Although the coherence between the surface morphology observed by AFM and the overall morphology observed by x-rays was not explicitly established, the agreement between the two techniques suggests a consistent trend.

As mentioned previously, there was no notable distinction observed in the appearance of the Bragg peaks among the samples. However, a slight deviation in peak position was still evident compared to the reference value. By calculating the diffraction peak positions using Bragg's law for a specific crystallographic orientation and lattice parameter, an estimation of the expected peak locations in XRD could be obtained. Upon comparing this reference value with the actual peak positions, a downward shift in peak position was identified for all samples. Table 4.7 depicts this trend.

The observation of shifted Bragg peaks for both STO and GAO indicates a change in the lattice parameter of both unit cells. As I delved into understanding the relationship between the deviating 2θ values and the lattice parameters, I found myself engaging in reverse calculations, utilizing Bragg's law. Through this process, I discovered that to achieve a match between the actual 2θ values, adjustments to the lattice parameters of both STO and GAO would be necessary. The downward shift in the position of the Bragg peaks corresponds to an increased lattice parameter. The largest change in 2θ peak position was noticed for GAO. It is unfavorable for STO to atomically rearrange

Plane \ Fluence	**3 J/cm^2**		**6 J/cm^2**		**9 J/cm^2**	
	Shin23_3	**Shin23_4**	**Shin20_5**	**Shin20_9**	**Shin20_6**	**Shin20_8**
001 STO	-0.088	-0.089	-0.087	-0.089	-0.140	-0.110
002 STO	-0.091	-0.096	-0.097	-0.093	-0.142	-0.101
004 GAO	-0.653	-0.772	-1.187	-0.908	-0.943	-1.051

Table 4.7: Table giving an overview of the change in diffraction peak position for each of the six samples in question. The value represents the peak position with respect to the calculated reference value. The complete list of peak positions as well as the reference can be found in the Appendices in Section 6.5.2 Tables 6.6 and 6.7.

to fit the GAO uc to prepare for epitaxial growth. Therefore, it is GAO which experiences the greatest amount of strain. One may imagine that one uc of GAO can cover four uc of STO, since the dimensions of GAO is twice as big as STO. This results in the GAO uc being strained in plane to fit the dimensions of STO. The growth of GAO on STO hence requires that GAO is tensile strained such that it gains a lattice parameter closer to $\sim$8 Å as compared to 7.911 Å. Nevertheless, it is thought that this strain effect is what leads to the anomalous band order where the d_{XY} state gets shifted above the $d_{\mathrm{XZ}}/d_{\mathrm{YZ}}$ states.

The shift in Bragg peak position is a great indication of epitaxial growth, since a shift in 2θ indicates that the lattice parameter has changed. The change in lattice parameter can be a manifestation of strain, since it reflects how the dimensions of the uc is altered. Strain can cause the lattice to be compressed or stretched resulting in a smaller or greater lattice constant. Epitaxial growth refers to the growth of a crystalline film on a substrate in such a way that the crystal structure of the film is aligned with that of the substrate. In the case of tensile strain, the uc of the crystal film is stretched to accommodate for the different lattice spacing of the substrate.

Based on the observation that all six samples displayed Bragg peaks with a consistent shift in peak position, similar size, and broadness, attributed to the (001)STO, (002)STO and (004)GAO, it can be concluded that GAO underwent epitaxial growth in the (001) direction during the depositions. The x-ray crystallographic analysis enabled a deepened understanding of the average degree of crystallinity and its variation with laser fluence. Additionally, these techniques confirmed the epitaxial growth of GAO on STO and provided insights into the possible strain effects experienced by GAO on STO.

4.2.4 Scanning electron microscopy

SEM imaging was performed on Shin23_4 and Shin20_5, two of the four samples that could not be assessed using XRR. The obtained SEM images did not reveal the anticipated thicknesses when compared to XRR measurements. However, the images did exhibit a contrast distinction between the regions belonging to GAO and STO. Figure 4.12 and 4.13a-b illustrates SEM images of Shin23_4 and Shin20_5, respectively.

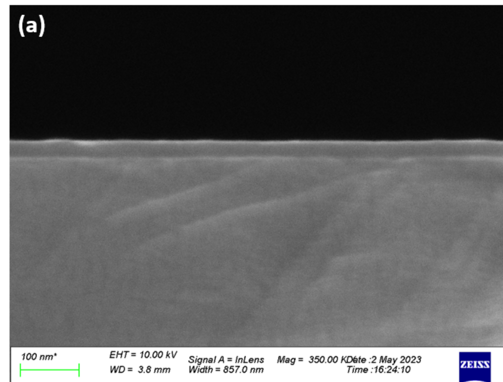

Figure 4.12: Scanning electron microscopy image of Shin23_4 SEM image of Shin23_4. The GAO/STO sample was grown for 30 minutes, utilizing a fluence of 3 J/cm^2 and a deposition pressure of 1.00 10^{-6} mbar. The scale bar measures 100 nm.

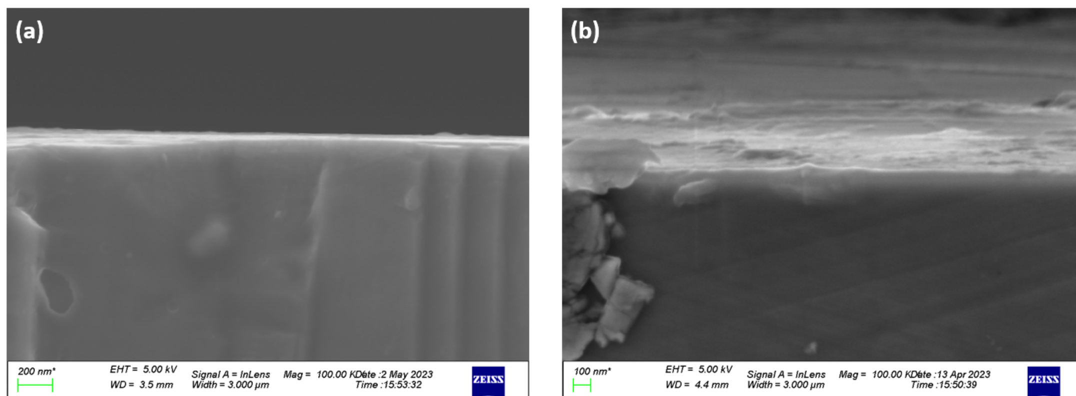

Figure 4.13: Scanning electron microscopy image of Shin20_5 SEM image of Shin23_4. The GAO/STO sample was grown for 30 minutes, utilizing a fluence of 6 J/cm^2 and a deposition pressure of 1.00 10^{-6} mbar. a) The scale bar measures 200 nm. b) The scale bar measures 100 nm.

It is noteworthy that the thickness of the Shin20_5 GAO thin film appeared to be rather heterogeneous in the SEM images. In contrast, Shin23_4 seemed much more homogenous. It is important

to consider that, similar to AFM, SEM provides insights into the local structure and cannot be used to obtain an averaged measure of thickness. Additionally, the samples were broken into smaller pieces before being coated with a 5 nm Ag layer. It is uncertain whether the observed heterogeneity in appearance is influenced by the sample preparation and cutting process.

Shin23_4 was one of the two samples grown with a fluence of 3 J/cm^2. XRR analysis indicated a GAO thickness of 16.8 nm for Shin23_3, whereas the SEM images suggested a thickness range of 30-50 nm for the GAO thin film in Shin23_4. Furthermore, the SEM images of Shin20_5 suggested a varying thickness of 20-100 nm. Consequently, it can be concluded that SEM did not provide a definitive clarification regarding the thicknesses of the GAO thin films in either Shin23_4 or Shin20_5. The SEM imaging was conducted by the PhD student Raphael Anacleto. A collection of all SEM images can be found in the Appendices in Section 6.4.2.

4.3 Transport properties of high mobility GAO/STO heterointerfaces

The first deposited GAO/STO heterostructures exhibited insulating 2-point and 4-point resistances which led to the adjustment of growth parameters in between depositions. As discussed in the section about growth parameters (Section 4.1), it was only when the deposition pressure was reduced from 1.00 10^{-5} mbar to 1.00 10^{-6} mbar and a fluence above 9 J/cm^2 was applied that the first conducting heterostructure was produced. Figure 4.14 displays the measured 4-point resistances in various as-grown Shin12 GAO/STO heterostructures. The plot illustrates the logarithmically scaled 4-point resistance as a function of laser fluence. Shin12_1 to Shin12_5 were grown using a background pressure of 1.00 10^{-5} mbar. This plot emphasizes the significant influence that the background pressure had on the quality of the interface. Notably, Shin12_6, indicated by a triangular marker, exhibited a room temperature (RT) 4-point resistance of 0.1 kΩ, equivalent to an estimated sheet resistance (R_S) of 0.4 kΩ/sq. From this deposition onward, all subsequent GAO/STO heterostructures were grown at pressures ranging from 1.00-2.00 10^{-6} mbar, while varying the fluence between 3-9 J/cm^2, in an effort to achieve reproducible high mobility GAO/STO heterointerfaces.

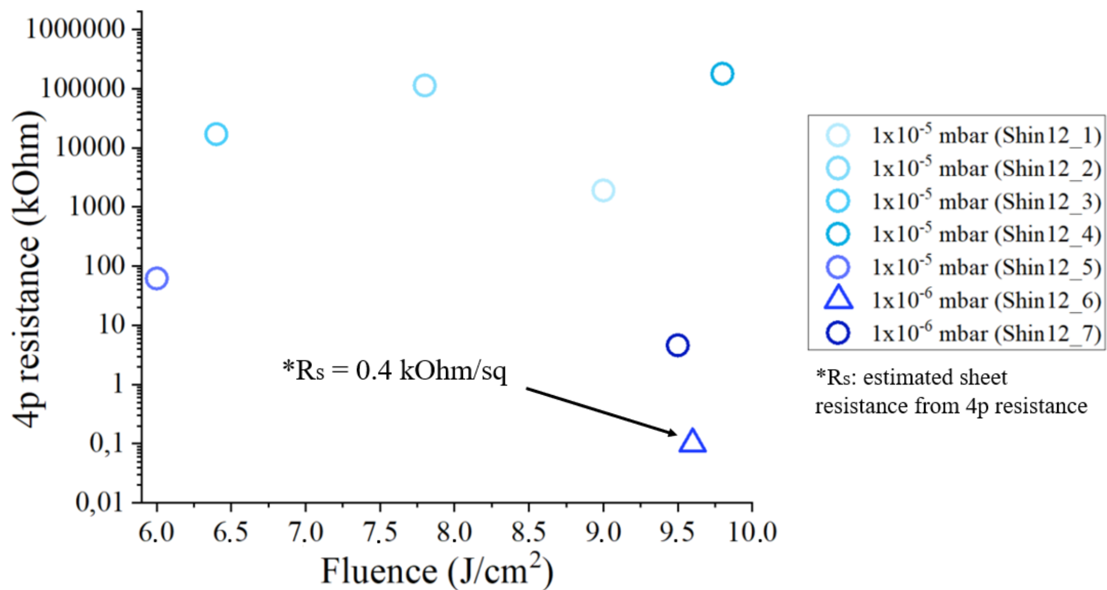

Figure 4.14: 4-point probe resistances of Shin12 GAO/STO heterostructures Shin12_1 to Shin12_5 were grown utilizing a background pressure of 1.00 10^{-5} mbar. It was not until the pressure was decreased to 1.00 10^{-6} mbar that a conducting interface was produced. Shin12_6 is highlighted by a triangle and exhibited a RT 4-point resistance equivalent to 0.4 kΩ/sq.

These sections revise the results of transport measurements conducted on as-grown GAO/STO heterostructures. The samples underwent wire bonding and were subjected to 2-point and 4-point resistance measurements to estimate the RT sheet resistance. Additionally, transport measurements were performed at both 300K and low temperatures to examine the actual sheet resistance, magnetoresistance, and Hall effect. Throughout these investigations, a pattern was observed, revealing a connection between the charge carrier density and mobility. The samples exhibited intriguing magnetoresistance and Hall coefficients, suggesting the presence of extraordinary magnetoresistance, anomalous Hall effect, and the collective contribution of multiple bands to the carrier mobility at low temperatures.

Presented here is first the data acquired from Shin12_6, followed by a comparative presentation of the transport data and electrical characterization pertaining to the remaining investigated GAO/STO heterostructures.

4.3.1 The first high mobility GAO/STO heterostructure: Shin12_6

Shin12_6 was the first GAO/STO heterostructure that exhibited conducting properties and measured a high carrier mobility. The growth of Shin12_6 involved a significant high laser fluence of 9.6 J/cm^2 and a low deposition pressure of 1.00 10^{-6} mbar. These parameters were carefully replicated to generate other GAO/STO structures with similarly enhanced carrier mobility. This section focuses on the transport measurements conducted on Shin12_6.

Shin12_6 underwent two separate measurements spanning a month. The initial measurement yielded the first recorded high mobilities and carrier densities, which are outlined in Table 4.8. Notably, a promising carrier mobility of 70,000 cm^2/Vs at 15K served as a motivation for growing samples using similar deposition parameters. However, due to technical challenges, a complete data set could not be obtained, leading to a subsequent round of measurements.

Temperature	n_S	μ
2 K	1.904 10^{15} cm^{-2}	24796.96 cm^2/Vs
15 K	1.811 10^{15} cm^{-2}	70774.95 cm^2/Vs
290 K	1.639 10^{15} cm^{-2}	8.46 cm^2/Vs

Table 4.8: Charge carrier denity and mobility of Shin12_6. Shin12_6 was measured two times. The first round of measurements showed Shin12_6 to exhibit the highest mobility at 15K.

Consequently, both data sets will be presented and subjected to further analysis. The results

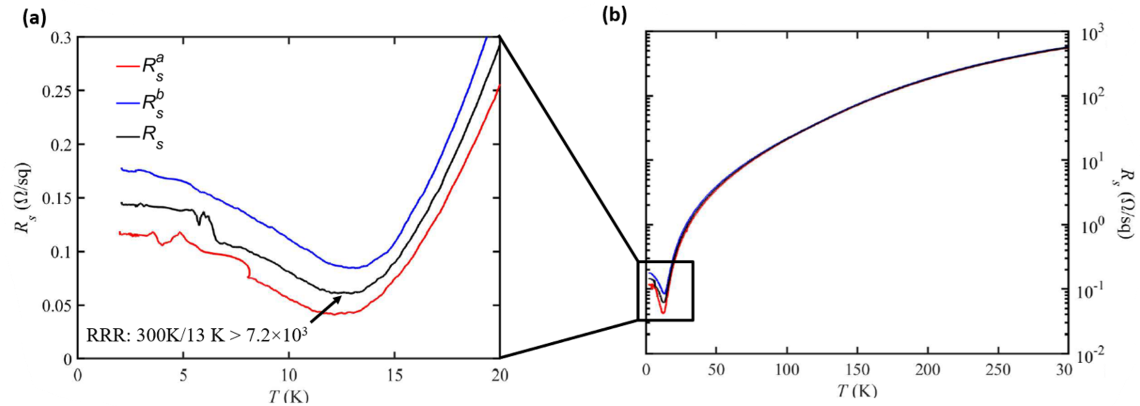

Figure 4.15: R_S measured in Shin12_6 Sheet resistance measured as a function of temperature for both permutations of Shin12_6. a) A closer look at the combined sheet resistance (R_S highlighted in black) calculated from the sheet resistance of permutation a ($R_S{}^a$ highlighted in red) and the sheet resistance of permutation b ($R_S{}^b$ highlighted in blue). The RRR was found to be 300K/13K>7.2 10^3 indicating high mobility. b) The full R_S as a function of temperature.

from the first set of measurements are denoted by a * symbol (i.e. Shin12_6*), distinguishing them from the second data set.

The sheet resistance was measured as a function of temperature for both permutations, denoted a and b. Figures 4.15a-b shows the sheet resistance measured for permutation a (highlight in red), permutation b (highlighted in blue) and the combined sheet resistance (highlighted in black). Figure 4.15a provides a closer look of the sheet resistance measured between 2 K and 20 K. An interesting upturn in resistance occurs around 13 K. At low temperatures an upturn in resistance, as the one measured in Shin12_6, can be associated to the Kondo effect as it is a phenomenon known to occur at low temperatures in 2DEGs. Due to lack of time and resources, this was not investigated further. Additionally, the different contributions from $R_S{}^a$ and $R_S{}^b$ are noticeable when compared to the combined R_S. The comparison emphasises the resistance differences that there may be between permutations. In the case of Shin12_6 $R_S{}^a$ is 0.05 Ω/sq lower as compared to $R_S{}^b$, and $R_S{}^a$ seems to have a kink at 2-7K which is noticeable in the combined sheet resistance as well. This shows the importance of measuring both permutations, as the combination of permutation a and permutation b gives a representative sheet resistance. As highlighted by a black arrow in Figure 4.15a the residual resistance ratio (RRR) between 300K and 13K was found to be >7.2x10^4. RRR is a measure of the ratio between the residual resistance and the normal state resistance of a material. A significant change in high temperature R_S as compared to low temperature R_S suggest a high electron mobility

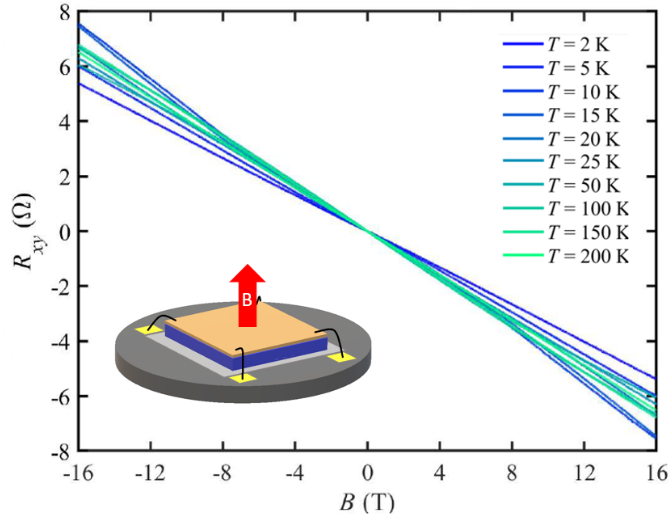

Figure 4.16: Magnetotransport measured in Shin12_6 Hall coefficients (R_{xy}) as a function of perpendicular applied magnetic field were measured from 200K to 2K. The Hall coefficients showed to include non-linear behavior at temperatures 5K, 10K, 15K, 20K, 50K and 100K.

of the sample. It implies that the heterointerface is of high quality and is capable of maintaining its desirable conductive properties even at low temperatures. It additionally indicates that the interface experiences minimal scattering and impurity effects, resulting in a higher overall electrical conductivity. The definition of a high residual resistance ratio was drawn from what had earlier been described by Christensen et al.[93] High-mobility interfaces tend to have a RT Rs≈1 kΩ and a RRR = Rs(300K)/Rs(2K)≈10^4. The latter was used as an indication of high mobility charge carriers.

After measuring the sheet resistance, the configuration of the cables was changed to Hall configuration. Hall resistances were then measured at various temperatures including 2K, 5K, 10K, 15K, 20K, 25K, 50K, 100K, 150K, and 200K. The magnetic field was swept between 16 and -16T. However, due to technical issues with the cryostat heater system, it was not possible to measure Hall resistances at 250K and 300K for Shin12_6. Figure 4.16 showcase the Hall resistances for the mentioned temperatures as a function of magnetic field. The magnetic field was applied perpendicular to the sample as illustrated in Figure 4.16.

Upon closer examination, it became evident that not all Hall curves exhibited linear behavior. The non-linear behavior suggested the presence of an anomaly in the charge transport. However, for a first approximation it was decided to fit the Hall curves with the 1-band model, to simplify the data treatment such that an estimate of the electron mobility could be made. The 1-band model

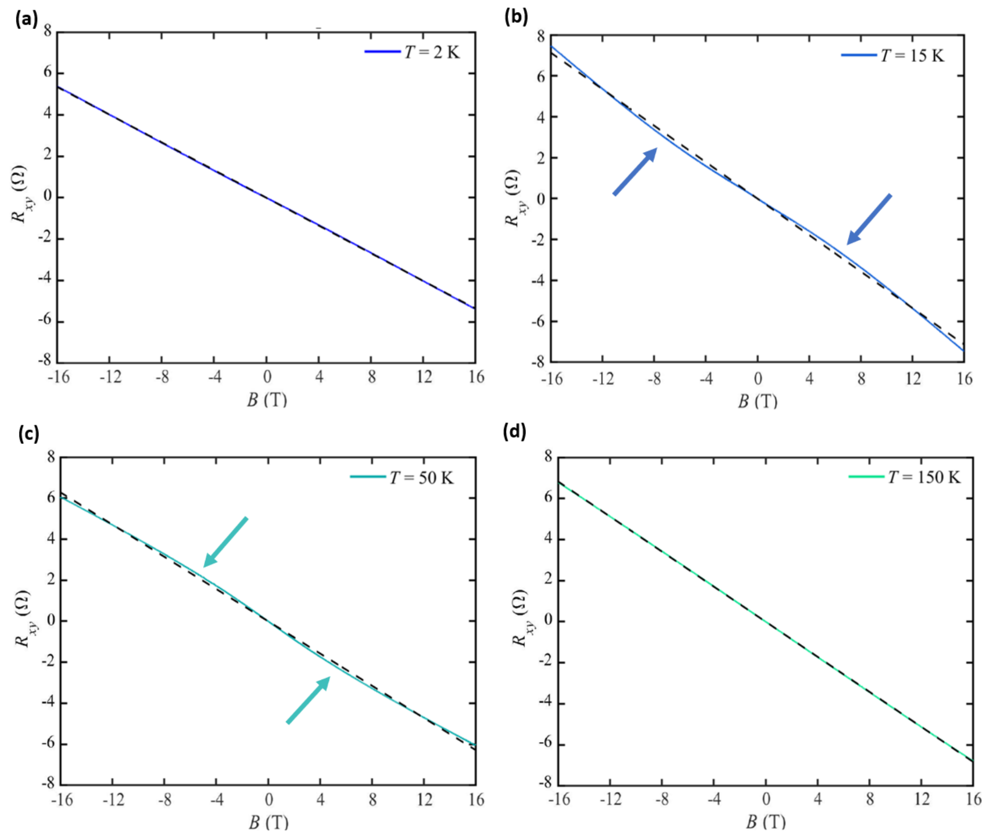

Figure 4.17: Separate Hall coefficients measured in Shin12_6 a-d) Separate Hall coefficients (R_{xy}) displaying the described linear and non-linear behavior. a) At T=2K the Hall coefficient showed linear behavior indicating ordinary Hall effect. b) At 15K the non-linearity was very distinct. Blue arrows indicate the non-linear behavior. c) At 50K the non-linear behavior seemed to have changed pre sign resulting a non-linearity symmetrical opposite as the one seen at 15K. This is highlighted by green arrows. d)The linear behavior was seen again from 150K-200K.

assumes that all charge carriers in the material belong to a single band characterized by a specific effective mass and mobility. In this model, the Hall resistance is primarily influenced by the charge carrier density and mobility of this single band, resulting in a linear Hall curve. The slope of the Hall curve corresponds to the Hall coefficient, which is directly related to the carrier mobility and charge carrier density.

Figures 4.17a-d shows the Hall curves for (a) T=2K, (b) T=15K, (c) T=50K and (d) T=150K. For T=2K and T=150K the behavior was linear and a linear fit was deemed appropriate to determine the mobility. A distinct non-linear behavior was noticeable for T=15K and T=50K and indicated the contribution from multiple bands to the charge transport. A more advanced method to treat

non-linear Hall data is to consider the presence of multiple bands by fitting the Hall coefficients with the 2-band model. Each band may have its own effective mass and mobility, which complicates the extraction of charge transport information as the contributions from different bands may interact thus resulting in a non-linear behavior. The presence of multiple bands can lead to multiple slopes in a Hall curve that cannot be explained by the 1-band model. Figure 4.17b shows the Hall resistance measured between 16 and -16T at 15K. The blue arrows denote a non-linear behavior, as described above. This behavior may be attributed to the Anomalous Hall effect (AHE). Furthermore, Figure 4.17c shows the Hall resistance measured between 16 and -16T at 50K. The green arrows denote a second non-linear behavior. This behavior is symmetrical opposite as compared to the non-linear behavior seen in Figure 4.17b and may be attributed to the existence of multiple bands. As it would become evident, a non-linear behavior was present in all the GAO/STO heterostructures following Shin12_6, indicating the occurrence of both AHE and the existence of multiple bands. From around 100K to 25K, Shin12_6 shows a behavior where multiple bands seems to contribute to the mobility of the system. The separated Hall curves for temperatures 10K, 20K, 25K, 100K and 200K can be found in the Appendices Section 6.6.2 Figure 6.32. At 25K the character of the non-linear behavior changes such that it may be associated with AHE, thus out competing any 2-band behavior that was present up until this point. Finally, at 2K the Hall coefficient takes it characteristic linear form again. The magnetoresistance for both permutations was measured as well. This data will be presented and compared with other MR data in Section 4.3.3.

The transport measurements conducted on Shin12_6 constructed the foundation for what we hoped would be reoccurring characteristics for other GAO/STO heterostructures grown with similar growth parameters. It was indeed very exciting to have grown a heterointerface with a mobility of 70,000 cm^2/Vs and to have found signs of what could be the Kondo effect, AHE and multiple bands contributing to the electron mobility.

4.3.2 Initial resistance measurements

As previously mentioned, the first objective was to cultivate a GAO/STO heterostructure measuring a low sheet resistance (kΩ range). This meant that the samples should as a consequence exhibit small 2-point and 4-point resistances. Once this was achieved, the growth parameters used to obtain this outcome were regarded as a reference point. Gradual adjustments to the growth parameters were then made to produce additional heterostructures with progressively smaller 2-point and 4-point

resistances. It should be noted that a decrease in 2-point resistance does not necessarily imply a proportional decrease in 4-point resistance. However, it was found that structures exhibiting 2-point resistances below 100 kΩ would additionally exhibit 4-point resistances in the low kΩ range. This trend was consistently observed across all GAO/STO heterostructures examined. To measure the 2-point and 4-point resistances of the as-grown GAO/STO heterostructures, a voltmeter and a simple setup consisting of a breakout box and a Keithley 2400 Sourcemeter providing DC were utilized. All resistance measurements were performed at RT. Table 4.9 presents the 2-point and 4-point resistances for GAO/STO heterostructures deposited using a laser fluence of 9 J/cm^2. The table includes the list of selected samples along with their corresponding growth parameters, such as laser fluence and deposition pressure, followed by the measured 2-point and 4-point resistances. Additionally, the estimated sheet resistance at RT, denoted as R_S*, is also provided. As discussed in Section 4.1 regarding growth parameters, it became apparent in the weeks preceding the submission deadline that it would not be feasible to measure all the samples initially planned for this project. Therefore, a decision was made to prioritize and focus on the samples listed in Table 4.9, excluding Shin12_1. For all samples except those prior to Shin12_6, the 2-point resistances measured below 100 kΩ. Shin12_1 exemplified the significant influence of deposition pressure on the 2-point and 4-point resistances, as it exhibited resistance values in the MΩ range, except for one 4-point resistance measurement. It is important to recall that the 2-point resistance includes the contact resistance between the gold pad on the chip carrier and the bonding thread, as well as between the bonding thread and the 2DEG. Therefore, this value may vary between different permutations and samples. Nonetheless, it serves as a valuable indicator when compared to the 4-point resistance, providing insights into the connectivity of all bonds to the 2DEG, the homogeneity of the 2DEG, and the sample's conductivity. This collection of 2-point and especially 4-point resistances served the purpose of an introductory evaluation before proceeding to transport measurements. At the time of submission Shin18_8 was still in the process of undergoing transport measurements, which prevented the evaluation of its 2-point resistances. Additionally, other samples not included in this thesis had not been investigated or were in the process of being investigated. As a result, the data from these samples was not immediately accessible for analysis and discussion within the specified time frame.

Sample	Fluence	Pressure	2-point resistance	4-point resistance	Estimated Rs*
Shin12_1	9 J/cm^2	1.00 10^{-5} mbar	8000 kΩ 14000 kΩ 26000 kΩ 21000 kΩ	7000/1900 kΩ* 1800/900 kΩ*	3600 kΩ/sq
Shin12_6	9.6 J/cm^2	1.00 10^{-6} mbar	9.05 kΩ 5 kΩ 9.6 kΩ 13.6 kΩ	0.1 kΩ 0.1 kΩ	0.4 kΩ/sq
Shin18_1	9 J/cm^2	1.50 10^{-6} mbar	24.90 kΩ 9.40 kΩ 4.84 kΩ 20.52 kΩ	224 kΩ 153 kΩ	854.35 kΩ/sq
Shin18_2	9 J/cm^2	2.00 10^{-6} mbar	19.22 kΩ 9.51 kΩ 5.25 kΩ 14.84 kΩ	0.179 kΩ 0.124 kΩ	0.686 kΩ/sq
Shin18_7	9 J/cm^2	1.00 10^{-6} mbar	80.1 kΩ 79.8 kΩ 87.8 kΩ 89.4 kΩ	4.22 kΩ 4.69 kΩ	20.2 kΩ/sq
Shin18_8	9 J/cm^2	2.00 10^{-6} mbar	37.56 kΩ 50.81 kΩ n/a n/a	1.96 kΩ 1.43 kΩ	7.6 kΩ/sq

Table 4.9: Initial resistance measurements The 2-point and 4-point resistance was measure on all GAO/STO heterostructures. In the case of as grown Shin18 samples was the 2-point resistance measured subsequently to all transport measurement presented in this thesis. All 4-point resistances were measure on as-bonded samples prior to transport measurements. The sheet resistance denoted Rs* was estimated by taking the average of the 4-point resistance and multiply it by $\frac{\pi}{ln(2)}$. The actual RT sheet resistance was measured for both permutations, where possible, and subsequently combined into the Rs utilized to determine the charge carrier densities at various temperatures presented later on. *Shin12_1 had a 4-point resistance that would differ with both permutations and which way the current was directed.

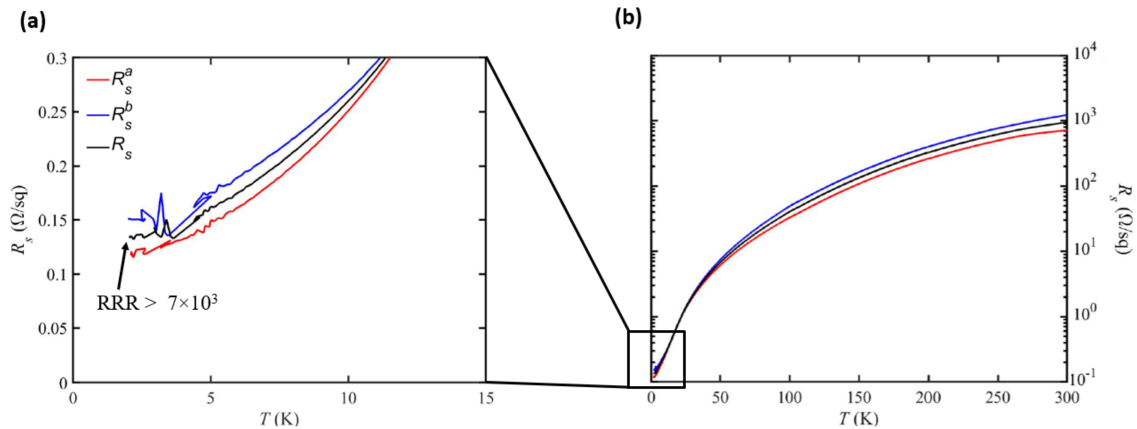

Figure 4.18: R_S measured in Shin18_1 Sheet resistance measured as a function of temperature for both permutations of Shin18_1. a) A closer look at the combined sheet resistance (R_S highlighted in black) calculated from the sheet resistance of permutation a (${R_S}^a$ highlighted in red) and the sheet resistance of permutation b (${R_S}^b$ highlighted in blue). The RRR was found to to be >7 10^3 indicating high mobility. b) The full R_S as a function of temperature.

The sheet resistance was measured as a function of temperature and was conducted for all samples. However, due to technical challenges related to the cryostat heating system, it was not possible to reach all temperatures, ranging from 300K to 2K. Additionally, not all samples had sheet resistance measurements for both permutations. These limitations were due to various factors such as time constraints, technical issues with the cryostat or measurement script, and occasional unexplained issues that resolved themselves over time. Therefore, it is important to note that some of the transport data presented may contain comments regarding missing data or deviations from the designated data collection protocol (Appendices Section **??**). It should be further noted that these deviations did not impede or compromise the conclusions presented in this thesis.

Figures 4.18, 4.19, and 4.20 display the sheet resistances measured as a function of temperature for Shin18_1, Shin18_7, and Shin18_8, respectively. Figure 4.18a provides a closer view of the sheet resistances in the range of 2K to 15K, where the full temperature range is shown in Figure 4.18b. For Shin18_1, slight differences were observed in the sheet resistance between permutation a (${R_S}^a$, highlighted in red) and permutation b (${R_S}^b$, highlighted in blue), similar to what was observed for Shin12_6 (Figure 4.15). This discrepancy can be attributed to the microstructure of the interface. The combined sheet resistance (highlighted in black) revealed that the anomalies in the final data points between 2K and 5K originated from ${R_S}^b$. The relative resistance ratio was determined to be greater than 7x10^3, indicating charge carriers of high mobility in Shin18_1. This measurement

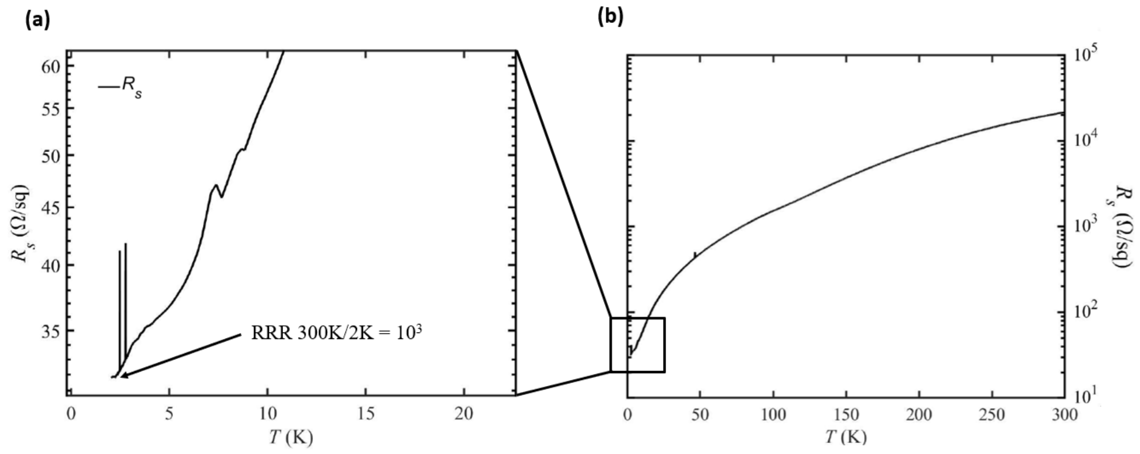

Figure 4.19: R_S measured in Shin18_7 The presented sheet resistance (highlighted in black) was estimated from $R_S{}^b$. a) A closer look at the combined sheet resistance. The RRR 300K/2K was found to be 10^3 indicating lower mobility as compared to Shin12_6 and Shin18_1. b) The full R_S as a function of temperature.

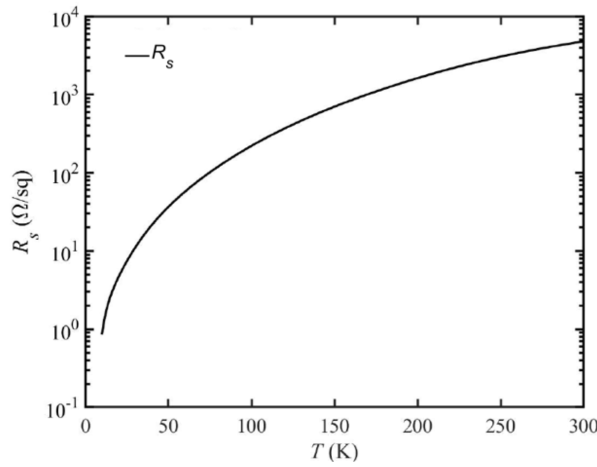

Figure 4.20: R_S measured in Shin18_8 The presented sheet resistance (highlighted in black) was an interpolation of separate R_S measurements where $R_S{}^a$ was assumed to be equal to $R_S{}^b$.

followed the prescribed data collection protocol.

The sheet resistance of Shin18_7 was determined by measuring the R_S of a single permutation. This was a different approach in contrast to Shin12_6 and Shin18_1, where $R_S{}^a$ and $R_S{}^b$ were combined to get the representative R_S. In the case of Shin18_7, this meant that only $R_S{}^a$ was measured in the range 300K to 2K. At 300K and 2K both $R_S{}^a$ and $R_S{}^b$ were measured, and the ratio between the high temperature and low temperature sheet resistance values was used to scale a plot for $R_S{}^b$ going from 300K to 2K. Now having a plot for both $R_S{}^a$ and $R_S{}^b$, the two data sets could be combined into the R_S plot depicted in Figure 4.19a-b. A closer look at the temperature range 2-20K is seen in Figure 4.19b. The relative resistance ratio for Shin18_7 was $\sim 10^3$ at 2K and indicated that a lower carrier mobility was to be expected as compared to Shin12_6 and Shin18_1.

The sheet resistance of Shin18_8 was estimated differently as well. The first attempt to measure the sheet resistance was made by measuring $R_S{}^b$ from 300K to 2K. However, from 10K and down when measuring the voltage drop for permutation b, it occurred that the voltage drop would not be the same in both directions. That is, if the current was directed from 1-2 it gave one voltage drop and when switched such that the current was directed from 2-1 it gave a different value. This deemed all sheet resistance measurements below 10K untrustworthy. It was therefore decided to measure the sheet resistance for one permutation from 300K to 10K before moving on to magnetotransport measurements. Unfortunately, time was not in out favor as for why only one permutation was measured. The measured R_S values were thus interpolated to create a R_S fit. Figure 4.20 shows the interpolated R_S.

The sheet resistances were used to gain the carrier mobilities ones the charge carrier densities were known from the Hall measurements. Charge carrier densities and Hall mobilities are presented and discussed in Section 4.3.4.

4.3.3 Magnetotransport in γ-Al_2O_3/$SrTiO_3$ heterostructures

Following the measurement of sheet resistances, a magneto-electric characterization was conducted, which involved measuring the Hall resistance as a function of magnetic field and magnetoresistance (MR). The magnetic field was swept over a range of -16T to 16T. Figures 4.21a-c illustrate magnetoresistance measured for (a) Shin12_6, (b) Shin18_1, and (c) Shin18_8. Figures 4.21a and 4.21b display the sheet resistance measured as a function of magnetic field. The red and blue lines represent

permutation a and permutation b, respectively. These results demonstrate the current orientation dependence of magnetoresistance. The MR data for both permutations had been defined from the sheet resistances, R_S^a and R_S^b, so that they intersect at B=0. This enabled the permutations to be compared. In the case of Shin12_6, permutation a displays a magnetoresistance five times larger than that of permutation b. Similarly, for Shin18_1, permutation a exhibits a magnetoresistance approximately 1 Ω/sq higher compared to permutation b. The observed discrepancy in magnetoresistance between permutations is consistent with the difference observed in the sheet resistance measurements (Figures 4.15 and 4.18) and could potentially be attributed to inhomogeneity in the microstructure.

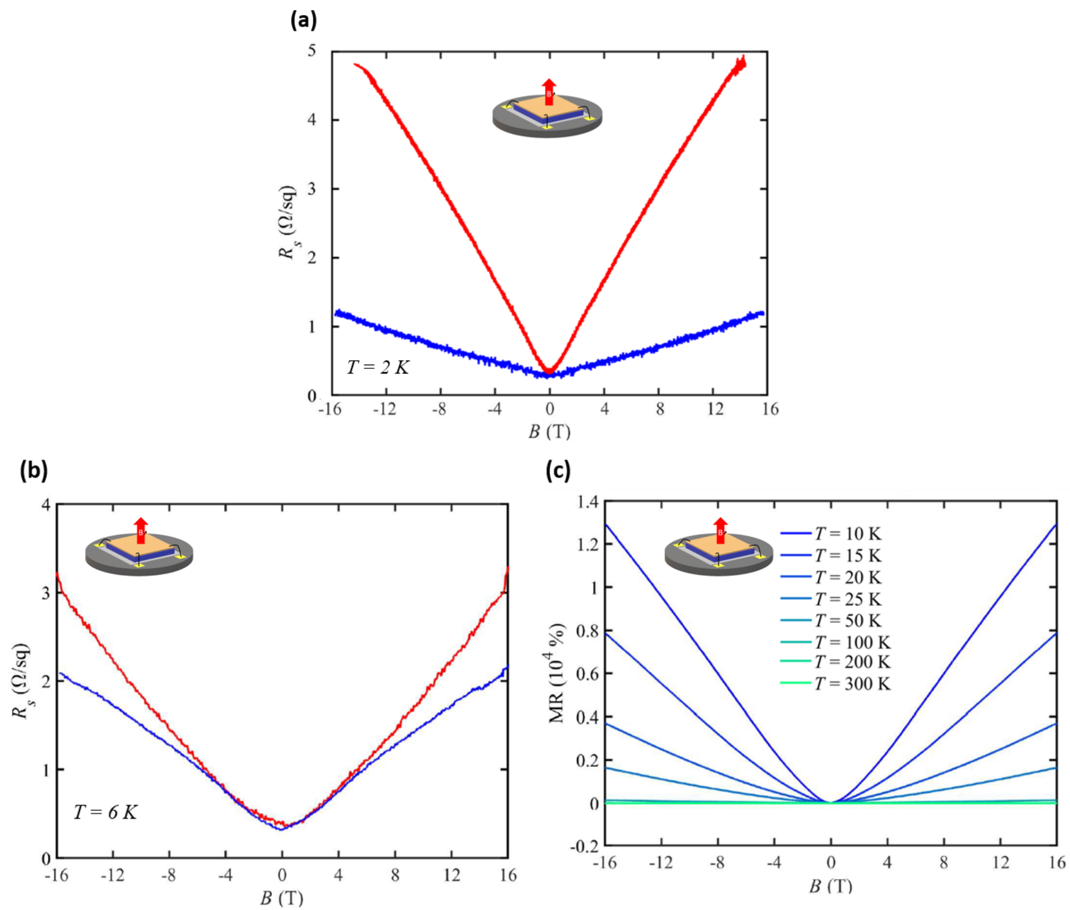

Figure 4.21: Magnetoresistance in GAO/STO heterostructures a) and b) display the MR measured as a function of perpendicularly applied magnetic field for Shin12_6 and Shin18_1, respectively. c) shows the percentage increase in MR as a function of magnetic field. At T=10K it measured 14,000% increase at ± 16 T.

The presence of inhomogeneity in the microstructure can lead to variations in the transport properties of the material, resulting in different MR values for different permutations. These inhomogeneities may arise during the growth of GAO on STO and could lead to differences in the scattering of charge carriers and how they respond to the applied magnetic field. Therefore, the inhomogeneous nature of the microstructure could contribute to the observed variations in both the sheet resistance as a function of temperature and the sheet resistance as a function of magnetic field, between different permutations.

In Figure 4.21c, the MR data for Shin18_8 is presented, showcasing the percentage increase as a function of magnetic field. The plot highlights a remarkable phenomenon referred to as Extraordinary Magnetoresistance (EMR). Magnetoresistance has both a geometrical and an intrinsic physical contribution. The geometrical contribution arises from the Lorentz force and manifests as a change in MR when varying the geometry. The physical contribution is intrinsic to the material and may give rise to phenomena such as anisotropic magnetoresistance (AMR) or giant magnetoresistance (GMR). EMR is characterized by a change in the behavior of MR at low magnetic fields as compared to higher magnetic fields. At low B-fields, MR increases as $\sim B^2$ as expected from the Lorentz force. However, at higher B-fields, MR increases linearly with no sign of saturation. In GAO/STO, exemplified by Shin18_8 in Figure 4.21c, the observed MR at low magnetic fields is likely to originate from the classical Lorentz magnetoresistance. The magnetic field causes a non-zero current to flow perpendicular to the electric field and saturates at high magnetic fields transforming into a linear, non-saturating magnetoresistance. At T=10K Shin18_8 exhibits an increase of up to 14,000%. A magnetic field can affect electrons to move in circular motions due the principle of the Lorentz force, therefore in the presence of a magnetic field, the Lorentz force can significantly affect the current flow near regions with varying resistance. It has been shown numerically that such redistributions in the current flow can cause a positive and linear MR that does not saturate. ([?,?]) The aforementioned inhomogeneities in the microstructure can be induced during the deposition of GAO on STO, or they can originate from the tetragonal domain formation in STO that happens below 105K. Additionally, asymmetric scattering caused by spin/orbit coupling can also play a role in the understanding of EMR in GAO/STO.

Hall curves were obtained for all five GAO/STO heterostructures. The main purpose of the Hall measurements was to obtain the charge carrier density and subsequently calculate the Hall mobility using the found R_S. Hall resistance curves were measured for different temperatures as the

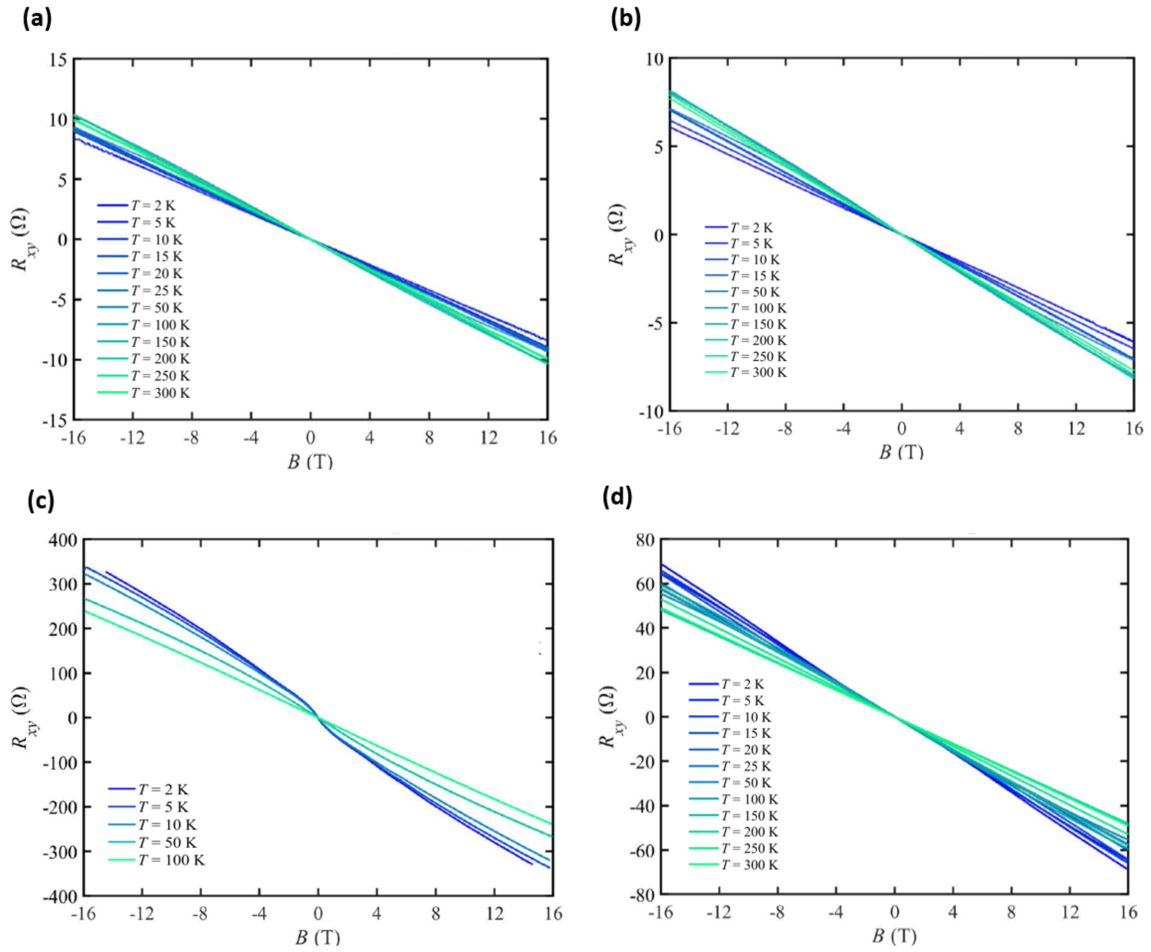

Figure 4.22: Magnetoresistance in GAO/STO heterostructures a) and b) display the MR measured as a function of perpendicularly applied magnetic field for Shin12_6 and Shin18_1.

samples were cooled from 300K to 2K. Figures 4.22a-d showcase the Hall curves for (a) Shin18_1, (b) Shin18_2, (c) Shin18_7 and (d) Shin18_8. A non-linear trend was shown to occur in the Hall data obtained from Shin12_6 (Figure 4.17). A similar non-linear trend was detected for all four aforementioned samples. The non-linear Hall effect was likely attributed to either the existence of multiple bands contributing to the transport or the AHE. The non-linear behavior will be further discussed in Section 4.3.4 with elaborations on the 2-band model and the AHE. Individual Hall curves are presented in the Appendices in Section 6.6.2 Figures 6.33, 6.34, 6.35, 6.36 and 6.37.

Based on the findings presented in the previous sections, the subsequent section will focus on the extraction of charge carrier densities and Hall mobilities. These parameters are derived from the analysis of sheet resistances and Hall curves obtained at various temperatures.

4.3.4 Charge Carrier Densities and Hall Mobilities of GAO/STO heterostructures

Returning to the primary objective of this masters project, the aim was to grow GAO/STO heterostructures by PLD with high-mobility interfaces. The subsequent step involved extracting the charge carrier density and electron mobility. In this section, the extracted charge carrier densities and carrier mobilities are presented, compared, and discussed. This analysis aims to identify any potential trends and determine if an optimum mobility, as a function of charge carrier density, was achieved.

To obtain the charge carrier densities and carrier mobilities the Hall curves presented in Section 4.3.3 were fitted with the 1-band model such that they could be extracted from the Hall coefficients. Table 4.3.4 details the investigated GAO/STO heterostructures along with their highest measured mobility.

At this point, the lack of fluence variation between the measured samples must be acknowledged. In Section 4.1, the growth parameters were discussed, and multiple GAO/STO heterostructures were presented, including samples deposited with laser fluences of 3 J/cm^2 and 6 J/cm^2. The original plan was to include an analysis of the samples presented in the beginning. However, considering the time-consuming nature of obtaining a complete transport data set, the final four weeks leading up to the submission were dedicated to measuring the samples that were most likely to exhibit high mobilities. The samples most likely to exhibit high mobilities were the GAO/STO heterostructures grown using a laser fluence of 9 J/cm^2. As a result, a decision was made to prioritize the samples dictated in Table 4.10 for the sake of efficiency. Table 4.10 depicts the samples Shin12_6(*), Shin18_1, Shin18_2, Shin18_7 and Shin18_8 along with their individual measured optimum in μ_{Hall}. The n$_S$, R$_S$ and the corresponding temperature at which the μ_{Hall} optimum occurred are listed as well.

Shin12_6(*) presents the first round of R$_S$ and Hall measurements that were conducted. At 15K the highest μ_{Hall} of all samples investigated was found in Shin12_6. The R$_S$ and n$_S$ at 15K was 60 mΩ and 1.81 10^{15} cm^{-2}, respectively. These exciting results were later discovered to be incredibly difficult to replicate, despite following a very strict protocol. However, it became evident later on for why this might have been the case. Before elaborating on this matter, further analysis of the

Sample	Fluence	Pressure	$R_S(\mu_{max})$	$n_S(\mu_{max})$	μ_{max}	T
Shin12_6*	9.6 J/cm^2	1.00 10^{-6} mbar	0.06 Ω/sq	1.81 10^{15} cm^{-2}	70,774 cm^2/Vs	15K
Shin18_1	9 J/cm^2	1.50 10^{-6} mbar	0.31 Ω/sq	1.11 10^{15} cm^{-2}	42,271 cm^2/Vs	2K
Shin18_2	9 J/cm^2	2.00 10^{-6} mbar	n/a	1.42 10^{15} cm^{-2}	25,694 cm^2/Vs	15K
Shin18_7	9 J/cm^2	1.00 10^{-6} mbar	31.85 Ω/sq	3.06 10^{13} cm^{-2}	6,421 cm^2/Vs	2K
Shin18_8	9 J/cm^2	2.00 10^{-6} mbar	0.86 Ω/sq	1.48 10^{14} cm^{-2}	27,152 cm^2/Vs	10K

Table 4.10: Mobility optimums for five GAO/STO heterostructures The maximum mobility achieved for the five investigated GAO/STO heterostructures are depicted with their corresponding n_S, R_S and the temperature at which the mobility optimum was reached.

pertaining samples was necessary.

Shin18_1 was deposited utilizing a pressure of 1.50 10^{-6} mbar and exhibited a μ_{Hall} of 42,271 cm^2/Vs, only half of what was exhibited by Shin12_6. The R_S reflected the decrease in mobility by being 5 times higher as compared to Shin12_6. Interestingly, the n_S was smaller as well but still in the 10^{15} cm^{-2} range. Shin18_1 did not exhibit an upturn in resistance as Shin12_6 and thus was the highest mobility found at 2K. The third highest mobility was found in Shin18_8 which was grown with a deposition pressure of 2.00 10^{-6} mbar. Here, the maximum μ_{Hall} was measured at 10K to be 27,152 cm^2/Vs. As n_S typically follows μ_{Hall}, the concentration of charge carriers was similarly smaller measuring 1.48 10^{14} cm^{-2}. As mentioned, Chen et al.[15] and Christensen et al.[62] found an optimum in carrier mobility for GAO/STO heterostructures with n_S ~10^{14} cm^{-2}. As seen in Figure 4.23a this does not seem to be the trend for the GAO/STO heterostructures investigated here. However, before drawing any conclusions several things must be taken into account.

First, the extraction of the mobilities was based on the 1-band model. It was obvious from the Hall coefficients presented in Section 4.3.3 that there were multiple Hall curves for which a non-linear fit was not ideal. Deviations from linearity in Hall coefficients are often a sign of multiple bands contributing to electron mobility, and it is, therefore, advisable to fit the non-linear Hall coefficients using the 2-band model. In other cases, a non-linear Hall coefficient is assigned to the AHE due to magnetic defects or the presence of spin-orbit coupling, resulting in a transverse voltage perpendicular to both the current flow and the applied magnetic field. Thus, the usual extraction of n_S from the slope of the Hall coefficient, at high magnetic fields, is in principle invalid as it will include contributions from both the ordinary Hall effect and the anomalous Hall effect. Given the time-consuming nature of growing conducting GAO/STO heterostructures and characterizing them both structurally and electrically, there was unfortunately insufficient time to conduct a thorough 2-band analysis of the Hall coefficients. In a 2018 article by Christensen et al.,[94] it was described that

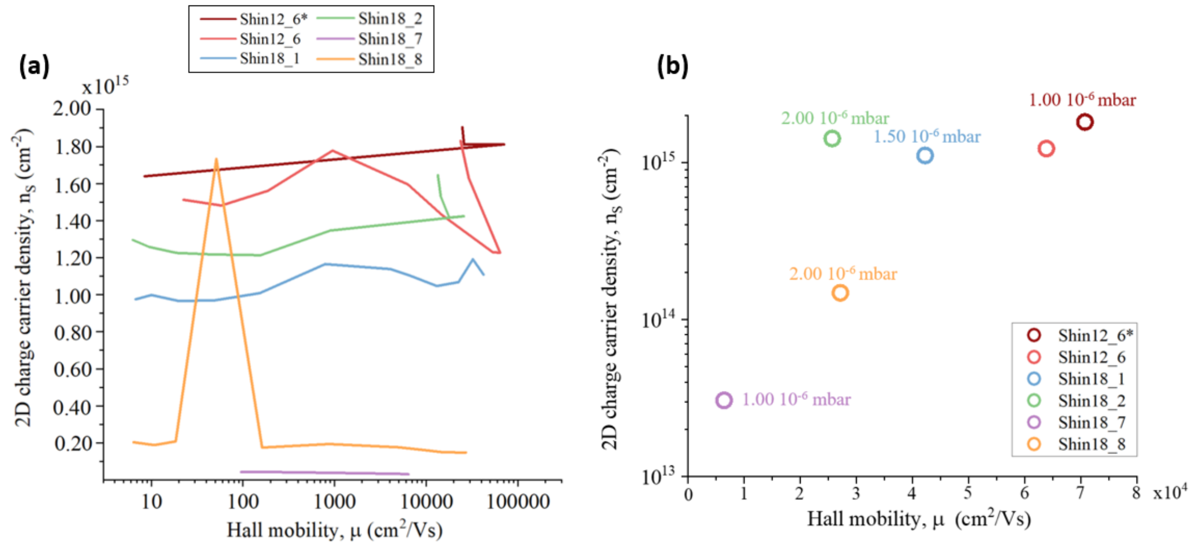

Figure 4.23: 2D Charge Carrier Densities as a function of Hall mobilities a) 2D n_S plotted against μ_{Hall} for the five depicted samples. Both measurements of Shin12_6 (depicted as Shin12_6* and Shin12_6) have been included. The x-axis depicting the mobility is logarithmically scaled. b) 2D n_S as a function of maximum μ_{Hall}. The deposition pressure employed is depicted for each sample. The data separated by sample is presented in the Appendices in Section 6.7 Figures 6.38a-e.

the non-linear Hall coefficients in GAO/STO heterostructures were not due to two-band conductivity, as it would require a coexistence of a large number of electrons and holes at the interface, which was rejected by another study conducted by the same author. Instead, the non-linearity was attributed to the AHE arising from an interaction between delocalized electrons and a magnetization along the interface normal. Therefore, it cannot be concluded whether only the AHE is the cause of the non-linear behavior in the Hall coefficients or if there are multiple bands contributing to the effective electron mobility.

The second thing to have in mind is the correlation between laser fluence, deposition pressure and mobility. It is well-known that the growth process, whether it is pulsed laser deposition, sputtering, atomic layer deposition or molecular beam epitaxy, is highly delicate and the electrical properties of the thin film can be very sensitive to the growth parameters. By now, it has been well established that the conducting properties of GAO/STO with greatest magnitude lies at the interface and thus is the quality and composition of the first few layers highly critical. The background/deposition pressure is one of the parameters that has been deemed to be critical for how the oxygen vacancies are produced at the interface. The laser fluence has also been debated to have an influence on the

conductivity of the interface. Alumina is an insulating material with a large band gab which thus requires a large amount of energy for it to bond with other materials. The choice of a high laser fluence, above 3 J/cm^2 to be exact, lied in the hypothesis that a laser pulse of very high energy would create Al^{3+} plasma species with a tremendous amount of kinetic energy. When the ions reached the surface of STO, they would pull oxygen atoms away from the interface to establish charge neutrality thus creating oxygen vacancies. The idea was that a low deposition pressure along with a high laser fluence would create a high concentration of oxygen vacancies and a low amount of defects, again as a consequence of the chosen parameters. The substrate was furthermore held at a temperature of 650 °C during the deposition to create a surface that would favorise the epitaxial growth of GAO on STO. Despite not having the opportunity to investigate other fluences than 9 J/cm^2, some information can still be drawn from comparing the maximum mobilities with their corresponding carrier densities and the pressure of which the GAO/STO heterostructures were grown. Figure 4.23b shows a plot of the μ_{max} and n$_S$ values presented in Table 4.10. The Figure depicts the 2D charge carrier densities as a function of maximum Hall mobility for Shin12_6, Shin18_1, Shin18_2, Shin18_7 and Shin18_8. Shin12_6 is depicted twice in the Figure representing the first (Shin12_6*, highlighted with a dark red circle) and the second (Shin12_6, highlighted with a lighter red circle) Hall mobility measured at the same temperature.

In the second set of transport measurements conducted on Shin12_6, the Hall mobility was determined to be 63,907 cm^2/Vs, which was lower than the initial measurement of 70,774 cm^2/Vs. This change in mobility was accompanied by a decrease in carrier concentration from 1.81 10^{15} cm^{-2} at 15K to 1.23 10^{15} cm^{-2}. The time gap between the two measurements, spanning a few weeks, contributed to the uncertainty regarding the rate of decrease in n$_S$ and μ after deposition. When considering the exceptionally high carrier mobility observed in Shin12_6, there are several potential explanations for the success of its high mobility interface, as well as the challenges encountered in reproducing those results. Figure 4.23b shows the 2D charge carrier densities as a function of optimum carrier mobilities. The plot demonstrates that there is no discernible trend associated with deposition pressure. For instance, despite being deposited under the same conditions as Shin12_6, Shin18_7 (depicted with a purple circle) exhibited the lowest mobility. In contrast, the second-best sample, Shin18_1 (depicted with a blue circle), was deposited at a pressure of 1.50 10^{-6} mbar. Both Shin18_2 and Shin18_8 (depicted with a green and yellow circle, respectively) were deposited at a pressure of 2.00 10^{-6} mbar and displayed similar mobilities but significantly different charge carrier densities. Shin18_2 had an n$_S$ of 1.42 10^{15} cm^{-2} and a μ_{max} of 25,694 cm^2/Vs, while Shin18_8 had

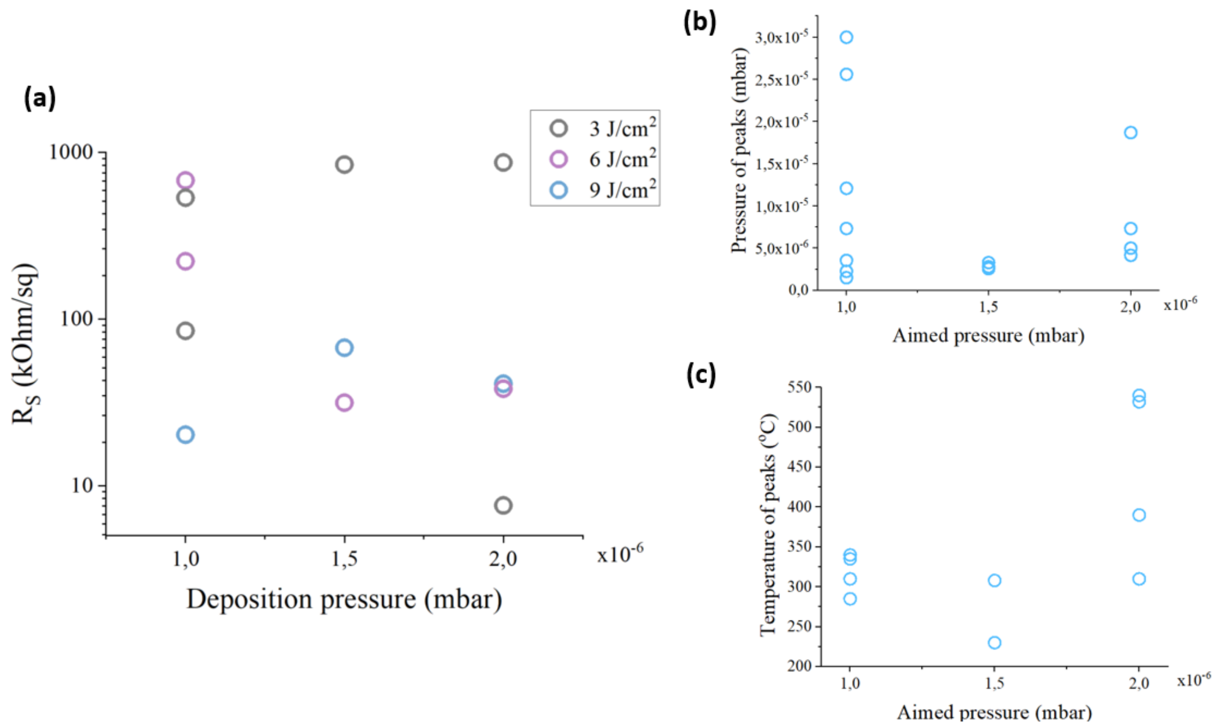

Figure 4.24: Deposition pressure dependency in RT Sheet resistance a) R_S estimated from 4-point resistances showed for several GAO/STO heterostructures deposited with laser fluences 3, 6 or 9 J/cm^2 and deposition pressures 1.00, 1.50 or 2.00 10^{-6} mbar. For each deposition the maximum pressure increase reached during heatup was log-booked along with the temperature of which it occurred. b) Pressure peak during hetup as a function of aimed background pressure. c) Temperature of the pressure peaks as a function of aimed pressure. The greatest fluctuations occurred at deposition pressure 1.00 10^{-6} mbar.

an n_S of 1.48 10^{14} cm^{-2} and a μ_{max} of 27,152 cm^2/Vs. Despite having a charge carrier density that was a thousand times smaller than Shin18_2, Shin18_8 exhibited a slightly higher carrier mobility.

The varying parameter, in the case of Shin12_6 as compared to the four other samples, was the deposition pressure. Specifically, it relates to the PLD system and the turbo pump used to maintain the pressure within the 10^{-6} mbar range. Figure 4.24a illustrates the plot of sheet resistance (estimated from RT 4-point resistance measurements) against the deposition pressure for GAO/STO heterostructures deposited with laser fluences of 3, 6, or 9 J/cm^2. Throughout this project, all GAO/STO heterostructures were at some point wire bonded to conduct 4-point resistance measurements. The estimated sheet resistance was then plotted against the pressure employed during deposition.

Initially, the resistances appeared to be scattered almost randomly. However, it was later realized that for all depositions following Shin12_6, the pressure would become unstable during the substrate

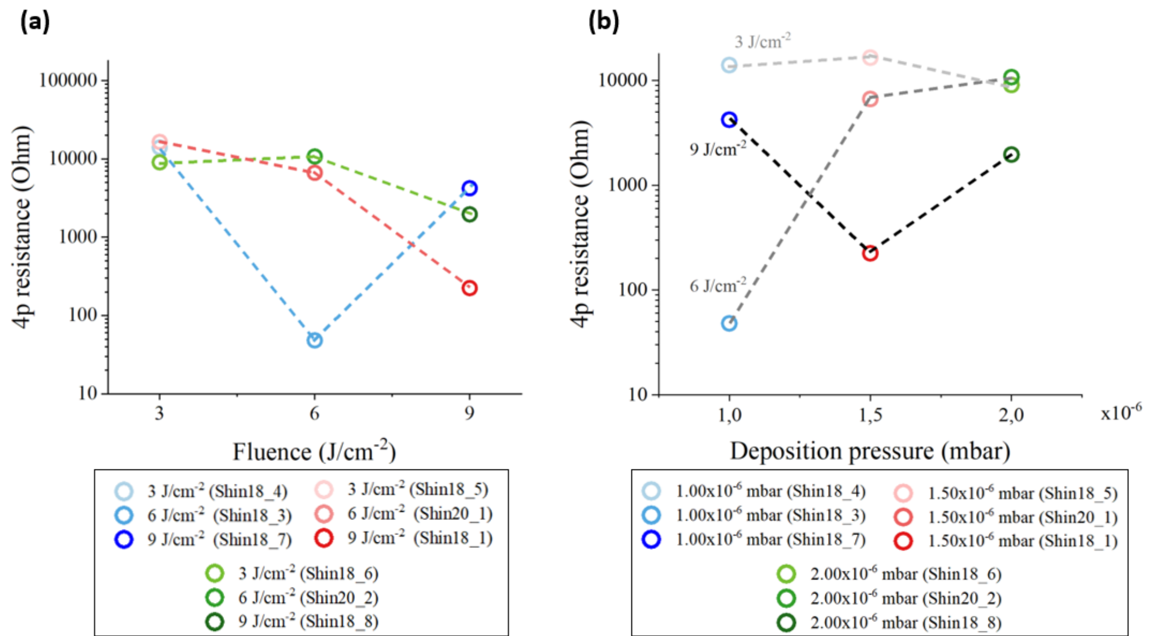

Figure 4.25: Fluence and pressure dependency of 4-point resistances. The 4-point resistances measured in as-deposited GAO/STO heterostructures plotted against laser fluence and deposition pressure. a) 4-point resistances as a function of laser fluence in 9 as-deposited GAO/STO heterostructures. b) 4-point resistances as a function of deposition pressure in 9 as-deposited GAO/STO heterostructures.

heating process. Without exception, the pressure would dramatically increase around 150°C. Despite all valves being opened to the turbo pump, the pressure occasionally rose as high as $\sim 3\ 10^{-5}$ mbar, even though it was intended to remain at $1.00\ 10^{-6}$ mbar. The pressure would eventually stabilize again around 300-500°C. This behavior is illustrated in Figures 4.24b and 4.24c. Notably, it seemed that the turbo pump would struggle the most to maintain stability at background pressures of 1.00 and $2.00\ 10^{-6}$ mbar, while it was relatively less unstable at a background pressure of $1.50\ 10^{-6}$ mbar. This trend is reflected in Figure 4.23, where significant differences in n_S and μ can be observed between samples, despite keeping all other parameters constant. The unstable pressure during the heat-up process may have contributed to these substantial variations. The underlying reasons for this instability remain currently unknown.

Despite the lack of transport and sheet resistance measurements on GAO/STO heterostructures deposited with laser fluences of 3 and 6 J/cm^2, some conclusions can still be drawn from the 4-point resistance measurements conducted on the as-deposited samples. Figures 4.25a and 4.25b shows the 4-point resistances as a function of (a) fluence and (b) deposition pressure. A trend was showing

where deposited GAO/STO heterostructures deposited with a fluence of 3 J/cm^2 were all higher in resistance as compared to samples deposited with a laser fluence of 6 and 9 J/cm^2. As shown in Figure 4.25b this was also true across samples grown with deposition pressures 1.00, 1.50 and 2.00 10^{-6} mbar. Another trend can cautiously be proposed. This includes that a small 4-point resistance can be gained from using a laser fluence of 6 J/cm^2 and stay at lower deposition pressures, or increase the fluence to between 6 and 9 J/cm^2 while increasing the deposition pressure.

It is important to state that for any trends regarding laser fluence, deposition pressure and magneto-electrical properties, all GAO/STO heterostructures introduced in this thesis must be thoroughly investigated as well as reinvestigated to confirm current results.

5 Conclusion and outlook

5.1 Conclusion

In conclusion, an experimental procedure for growing high mobility γ-Al_2O_3/$SrTiO_3$ heterointerfaces was successfully produced. The growth process was found to be highly influenced by the background pressure, particularly a continuously stability of the pressure was found to be of great importance. Additionally, the laser fluence was also found to be of great significance, but deemed to be less crucial as long as the fluence was in the range of 6 to 9 J/cm^2, as 3 J/cm^2 seemed to produce overall less conducting samples. Furthermore, it can be concluded that based on the structural characterization of a total of 25 GAO/STO heterostructures where AFM, RHEED, XRD and XRR was employed, it was unanimously proved that the grown GAO thin films exhibited locally and globally crystalline appearance and confirmed epitaxial growth. SEM was employed as a supplementary to XRD and XRR but did unfortunately not provide any new information on the structural characterization neither did it provide a trustworthy thickness of the GAO thin films investigated. Lastly, it can be concluded from magneto-electrical measurements that the five investigated GAO/STO heterostructures (Shin12_6, Shin18_1, Shin18_2, Shin18_7 and Shin18_8) all exhibited intriguing classical and quantum phenomena. Shin12_6 measured the highest mobility of 70,000 cm^2/Vs, but unfortunately is was proven very difficult to replicate these results. This may have been due to an unstable background pressure present for all sample following Shin12_6, exemplifying the importance of a carefully controlled pressure from the beginning of the heating process and with high probability cool down process as well. Shin12_6 also exhibited an upturn in sheet resistance, as the only sample of five, which may be associated with the Kondo effect. Furthermore, a difference in sheet resis-

tances was found between permutations, for the samples where both permutations were measured. This distinct difference was found in magnetoresistance measurements as well pointing to inhomogeneity in the microstructures. Inhomogeneity can manifest as large magnetoresistances. This was found in a sample (Shin18_8) grown with a fluence of 9 J/cm^2 and deposition pressure of 2.00 10^{-6} mbar which showed a magnetoresistance profile resembling Extraordinary magnetoresistance with the highest change in MR of 14,000% at 10K. In all five samples where transport properties were investigated non-linear Hall coefficients were found at varies temperatures. The non-linear behavior was associated with multiple bands contributing to the charge transport and the anomalous Hall effect. In summary, high mobility GAO/STO heterointerfaces were grown by Pulsed Laser Deposition and subsequently undergone structural and electrical characterization in order to determine the magnetotransport behavior and conductivity of the structures. It can be concluded that we did not succeed with producing a protocol of which reproducible GAO/STO heterostructures with tunable charge carrier densities and electron mobilities were exhibited. We did find trends pointing to the interface being highly sensitive to the background pressure. If reproducible GAO/STO heterostructures were to be achieved, it might be possible to find the optimum in mobility maybe for charge carriers in the 10^{15} cm^{-2} regime. This masters project has definitely opened up for new exciting paths to be investigated for the GAO/STO heterointerface, as well as insight in how delicate the deposition process and parameters is to conductive oxide interfaces.

5.2 Outlook

The work presented in this thesis opens up a vast expanse of possibilities moving forward. Several exciting phenomena has been introduced including the Kondo effect, the Extraordinary magnetoresistance, the anomalous Hall effect, spin-orbit coupling and the possibility of multiple bands contributing to the charge transport.

In future investigations, the focus should be on the magneto-electrical properties of several GAO/STO heterostructures. A discovery was made on superconductivity in the Shin18_8 sample at very low temperatures, presenting an exciting opportunity for further exploration. Additionally, eight more heterostructures are currently being studied, including one with a fluence variation, which requires investigation to validate or refute proposed trends in this thesis.

Replicating samples is always of interest, and if feasible, it would be advantageous to experiment with higher deposition temperatures ranging from 700-750°C. In our research group, a postdoc has demonstrated that increasing temperatures to 700°C or higher improves the local crystallinity of thin films on STO, as observed through AFM analysis. By pushing the deposition temperatures even higher, a further enhancement of epitaxial growth may be achieved and gain insights into how deposition temperature affects the charge carrier density and carrier mobility at the GAO/STO heterointerface.

To gain deeper insights into charge transport, carrier density, and carrier mobility, a comprehensive 2-band analysis of the non-linear Hall coefficients should be performed. This analysis will provide a better understanding of how the deposition parameters may have influenced the interface.

In addition to the presented structural characterization, reciprocal space mapping (RSM) may be employed as to offer valuable information regarding strain effects at the GAO/STO interface.

As future proposed work, further control and manipulation of carrier density and mobility in GAO/STO heterostructures may be investigated. The experimental procedure involves annealing backgated samples, grown at varied growth parameters, at 200-300°C with a voltage bias, followed by transport and resistance measurements. The samples would be investigated with transport and resistance measurements prior to the experiment as well. Three samples with different growth parameters should be used, including one for annealing without voltage bias.

6 Appendices

6.1 Tube furnace and annealing procedure

6.1.1 Protocol

Before proceeding to prepare for annealing, check if the tube furnace is already running:

- There will be a flow of bubbles in the glass on the bottom of the drawer under the oven.
- Data will be continuously generated on the computer.
- The thermometer under the oven will be showing a temperature larger than RT.

Preparing for annealing:

1. Make sure the tube is in the centre of the metallic furnace. Use the ruler to measure the length of the tube (outside part only) on both sides of the furnace (there should be the same length ± 1 mm on either side).
2. Open the tube in the end that points towards the computer.
3. Using gloves: take out the alumina plug and place it on a clean piece of paper*.
4. Place the sample that you want to anneal in the correct crucible (the one marked STO is ONLY for STO), in the farthest.
5. Place the crucible (containing the sample) on top of another crucible (do not use the one for STO) (should be stacked lid-box-box-lid) and place them in the tube with sample pointing towards the centre of the furnace.
6. Using the metal stick that isn't point, push in the crucible stack until it reaches the middle of the oven. The middle can be determined by the marks on the stick or by the (carefully) collision with the thermocouple, blocking the crucible.
7. Push in the alumina plug, until the outer face of it is aligned with the outer face of the oven pointing towards the computer.
8. Close the oven switching between the screws in a cross like fashion, not tightening one of them completely before the others.

9. Turn the knob cantered under the oven until the small marble reaches 10. Make sure that the correct gas is on before turning the knob!

10. Check if there is a bubble flow in the glass on the bottom drawer. If not, tighten the screws to close the oven even further.

11. When the bubbles are visible, turn down the knob as much as possible without letting the bubble flow start to lose its continuity.

12. Repeat step 1).

13. Set the annealing criteria on the computer, type in the location of your log-file (name of your folder) and end it by "name of your log-file* .txt". Run the process by clicking the on the white arrow in the top left corner.

14. Leave for 25 hours or until the temperature is below 50 degrees. Ensure that the program is finished. Close the gas supply.

15. Take out your sample by opening the tube in the end pointing towards the computer. Using gloves, take out the alumina plug using the metal stick with the sharp end, place it on a clean surface. Using the metal stick, that is not sharp, carefully drag out the crucibles. Take out the substrates and put place the crucibles back in their respective bags.

16. Put back the alumina plug and close the tube as step 8).

The specific parameters used for annealing STO substrates is listed in the table below.

Parameter	Value
Gas	Oxygen
Dwell temperature	1000 °C
End temperature	25 °C
Ramp rate	1.66
Ramp rate cooling	1.66
Dwell time	60 min
Dwell time end	240 min

Table 6.1: Annealing parameters for $SrTiO_3$ substrates

6.1.2 Example of data

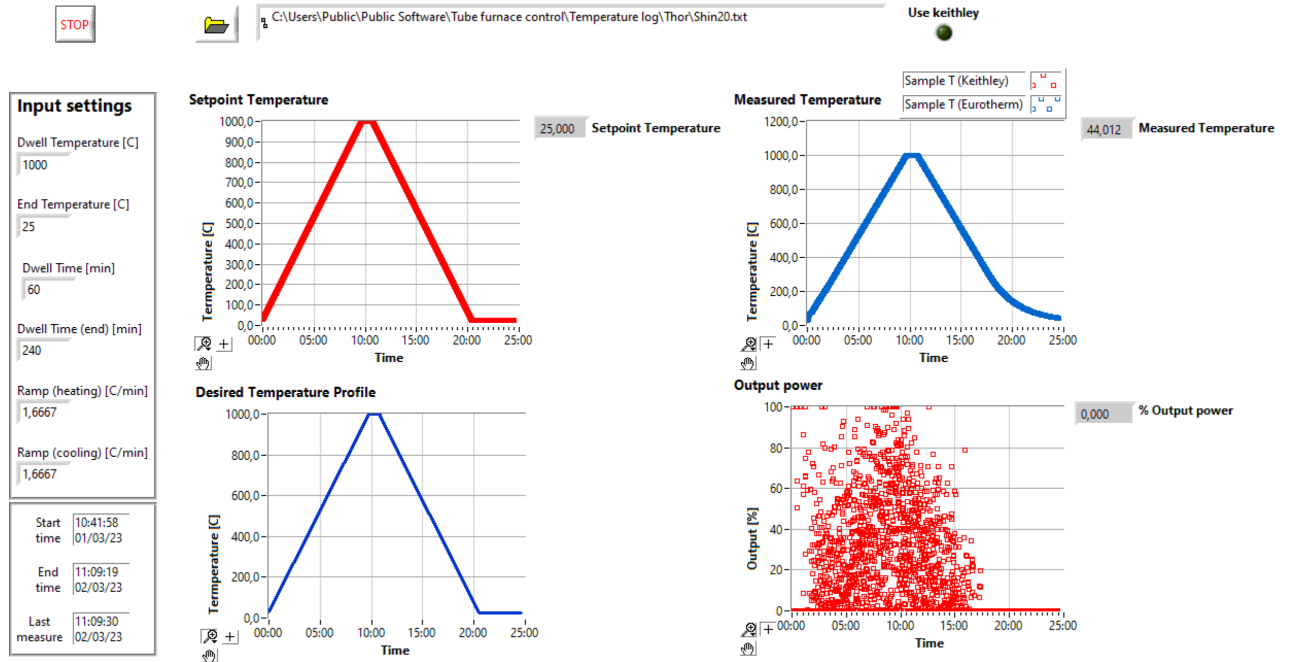

Figure 6.1: Annealing log Screen shot of the temperature profile of the annealing of Shin20 (3x3 piece).

6.2 Pulsed laser deposition

6.2.1 Deposition and growth parameters

All depositions were conducted cf. the standardized protocol (6.2.2) and the growth parameters listed in table 4.1.

Parameter	Value
Background gas	Oxygen
Oxygen flush	Flow 0.2 to reach 7.00 10^{-2} mbar
Deposition pressure	Varying
Deposition temperature	650 °C
Ramp rate	15 °C/min
Laser fluence	Varying
Substrate-target distance	450 mm
Pre-ablation time	10 min at RT
Dwell time at deposition temperature	10 min
Laser saturation time	60 sec
Deposition time	4 min / 30 min

Table 6.2: Caption

A table of all conducting samples is listed in table 6.3.

Sample	Comment	Deposition time	Laser fluence	Pressure	Temperature
Shin12_6	GAO/STO thin film	4 min	9.63 J/cm^2	1.00E-6 mbar	650 °C
Shin18_1	GAO/STO thin film	4 min	9.22 J/cm^2	1.50E-6 mbar	650 °C
Shin18_2	GAO/STO thin film	4 min	9.29 J/cm^2	2.00E-6 mbar	650 °C
Shin18_3*	GAO/STO thin film	4 min	6.08 J/cm^2	1.00E-6 mbar	650 °C
Shin18_4	GAO/STO thin film	4 min	3.1 J/cm^2	1.00E-6 mbar	650 °C
Shin18_5	GAO/STO thin film	4 min	3.15 J/cm^2	1.50E-6 mbar	650 °C
Shin18_6	GAO/STO thin film	4 min	3.17 J/cm^2	2.00E-6 mbar	650 °C
Shin18_7	GAO/STO thin film	4 min	9,12 J/cm^2	1.00E-6 mbar	650 °C
Shin18_8	GAO/STO thin film	4 min	9,12 J/cm^2	2.00E-6 mbar	650 °C
Shin18_9	GAO/STO thin film	4 min	6.05 J/cm^2	1.00E-6 mbar	650 °C
Shin20_1	GAO/STO thin film	4 min	6.02 J/cm^2	1.50E-6 mbar	650 °C
Shin20_2	GAO/STO thin film	4 min	6.03 J/cm^2	2.00E-6 mbar	650 °C
Shin20_3	fell off heater	-	-	-	-
Shin20_4	GAO/STO thin film	4 min	6.14 J/cm^2	1.00E-6 mbar	650 °C
Shin23_5	fell off heater	-	-	-	-
Shin23_6	GAO/STO thin film	4 min	9.04 J/cm^2	2.00E-6 mbar	650 °C
Shin23_7	GAO/STO thin film	4 min	6.03 J/cm^2	1.00E-6 mbar	650 °C
Shin23_8	GAO/STO thin film	4 min	5.50 J/cm^2	1.00E-6 mbar	650 °C
Shin23_9	GAO/STO thin film	4 min	5.01 J/cm^2	1.00E-6 mbar	650 °C

Table 6.3: 4 minute deposited samples in order starting with the first high mobility sample (Shin12_6). Shin18_3 is marked with an * due to technical issues prolonging the time at 650 °Cwith 17 minutes before ablation.

A table of all conducting samples with charge carrier densities and mobilities is listed in table 6.4.

A table of all samples made for the purpose of thickness determination is listed in table 6.5.

Sample	Laser fluence	Pressure	n_s	μ
Shin12_6*	9.63 J/cm^2	1.00E-6 mbar	1.811 10^{15} cm^{-2}	70,774 cm^2/Vs
Shin12_6	-	-	1.23 10^{15} cm^{-2}	63,907cm^2/Vs
Shin18_1	9.22 J/cm^2	1.50E-6 mbar	1.11 10^{15} cm^{-2}	42,271 cm^2/Vs
Shin18_2	9.29 J/cm^2	2.00E-6 mbar	1.42 10^{15} cm^{-2}	25,694 cm^2/Vs
Shin18_4	3.1 J/cm^2	1.00E-6 mbar	n/a	n/a
Shin18_5	3.15 J/cm^2	1.50E-6 mbar	n/a	n/a
Shin18_6	3.17 J/cm^2	2.00E-6 mbar	n/a	n/a
Shin18_7	9,12 J/cm^2	1.00E-6 mbar	3.06 10^{15} cm^{-2}	6,421 cm^2/Vs
Shin18_8	9,12 J/cm^2	2.00E-6 mbar	1.48 10^{15} cm^{-2}	27,152 cm^2/Vs
Shin18_9	6.05 J/cm^2	1.00E-6 mbar	n/a	n/a

Table 6.4: Charge carrier densities and mobilities of 4 minute deposited samples with laser fluence and deposition pressure.

Sample	Comment	Deposition time	Laser fluence	Pressure	Temperature
Shin20_5	XRD/XRR	30 min	6.08 J/cm^2	1.00E-6 mbar	650 °C
Shin20_6	XRD/XRR	30 min	9.12 J/cm^2	1.00E-6 mbar	650 °C
Shin20_7*	XRD/XRR	30 min	9.23 J/cm^2	1.00E-6 mbar	650 °C
Shin20_8	XRD/XRR	30 min	9.23 J/cm^2	1.00E-6 mbar	650 °C
Shin20_9	XRD/XRR	30 min	6.14 J/cm^2	1.00E-6 mbar	650 °C
Shin23_1	blocked laser beam	-	-	-	-
Shin23_2	blocked laser beam	-	-	-	-
Shin23_3	XRD	30 min	3.21 J/cm^2	1.00E-6 mbar	650 °C
Shin23_4	XRD	30 min	3.21 J/cm^2	1.00E-6 mbar	650 °C

Table 6.5: 30 minute deposited samples for the purpose of x-ray crystallographic analysis.

Maybe include temperature in description and add charge carrier density and mobility. Maybe rearrange the order with increasing fluence.

6.2.2 Protocol

1. Prepare the heater by securing the substrate with silver paste on the omicron plate.
2. Check that
   (a) The heater is turned off in the PLD software.
   (b) The PLD is set to loading position.
   (c) The main and foreline valves are open and that the rough and bypass valves are closed.

    (d) The oxygen flow is off.

3. Load the substrate and relevant target(s) is necessary.
4. When the heater is correctly placed in the chamber, make sure that it is left to pump in 20-30 min to remove silver paste fumes.
5. Secure the heater from the laser:
    (a) Set the heater position to "Deposition" and move it away from the laser beam pathway.
    (b) Apply the shutter on the heater.
    (c) Block the laser beam path with an additional shutter in the beamline.
6. Setting up the laser:
    (a) Align the laser beam using mirrors mask and lens at the intended positions. Make sure the path is free from other masks or obstacles.
    (b) Change the laser energy in order to get the intended value. Measure the laser energy in front of the chamber with a laser meter. Note the acceleration voltage and the energy displayed on the laser, while it is running.
7. Oxygen flush: Make sure that the oxygen flow is set to 0 in the PLD software. Close the main valve (and keep all valves but the foreline valve closed as well) and open for the oxygen flow by flicking the contact. Set the oxygen flow to 0.2 and let the pressure in the chamber rise to 7.00E-2 mbar before setting the oxygen flow back to 0.
8. To restore the intended background pressure, carefully open the bypass valve slightly and close it once the turbo pump increase in current. Give the turbo pump time to process the gas and decrease the pressure to below E-3 mbar before opening the main valve. Open and close the valve 2-3 times until the valve can be fully opened without the current increasing above 2 A.
9. Open the main valve slowly and keep an eye on the turbo pump current to not increase above 2 A. Close the bypass valve as soon as the main valve has been opened.
10. Set the pressure (deposition pressure) manually using the Main valve and the Bypass valve, if necessary. For depositions with pressure below 2.00E-6 mbar it is necessary to close the oxygen inlet to maintain the low pressures.

11. Setting up the target for pre-ablation and deposition:
    (a) Set the target to "Center scan area" and start the target scan.
    (b) Remove the shutter in the beamline to clear the laser beam pathway.
    (c) Make sure the target is in motion and pre-ablate once the pressure has been stabilized on the deposition pressure value.
    (d) Make sure that the heater is moved away from the laser beam pathway and the heater shutter is on.
    (e) Pre-ablate for 10 minutes using the chosen laser energy and a frequency of 1 Hz.
    (f) Do not attempt to control the pressure during pre-ablation but leave it on the set settings.
12. Once the pre-ablation is finished, reestablish the pressure and begin the heat up of the heater. This is done in the PLD software: Set the temperature, press the ramp rate ("ramp on") and then the temperature. Maintain the pressure during the heat up by controlling the Main and Bypass valves continuously.
13. Wait 10 minutes when at deposition temperature before starting the deposition.
14. Deposition:
    (a) Check if the heater is adjusted to deposition X, Y and Z position.
    (b) Check if the target is at "Center scan area" and is scanning.
    (c) Check if the laser beam is blanked by the shutter in the beamline.
    (d) Check for obstacles that may block the laser beam.
    (e) Start the laser and let it stabilize for 1 minute before removing the shutter.
    (f) Start a timer for the deposition time.
    (g) Do not attempt to stabilize the pressure during deposition.
    (h) Stop laser by pressing the "?" and blank the laser beam with the shutter in the beamline.
    (i) Return to stabilize the pressure to deposition pressure and wait 5 minutes before starting cooldown.
    (j) Adjust the pressure during cooldown during the first 200-350 °Cand turn of the heater when there is at least 40 °Cbetween setpoint and real temperature.

(k) Leave when the pressure is stable or when below 250 °C.

(l) When the temperature is <50 °C, unload the sample, clean the omicron plate and leave the heater in the cupboard next to the fume hood.

6.3 Atomic force microscopy protocol

The atomic force microscope used in this project was a model from Bruker (Nanoscope V scanning) and displayed in Figure 6.21

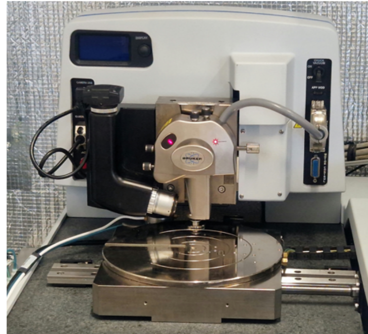

Figure 6.2: AFM of substrate used for deposition of R2 The substrate showed very distinct terraces with holes present in the surface structure.

In the case of substrate imaging: Clean the substrates with acetone and isopropanol for 2 minutes. In the case of deposited sample imaging: the samples were not further treated or cleaned due the risk of silver sticking to the surface and thereby contaminating the interface.

6.3.1 Protocol

1. Check if the correct AFM scanner head is connected or if this needs to be changed (use FASTSCAN scanner head)
2. If needed, change the tip to the FASTSCAN A AFM tip.
3. Setup the AFM
   (a) Choose "tapping in air" mode (when opening the nanoscope program)
   (b) Make sure that the probe is set to "FASTSCAN A"
   (c) Focus the tip
4. Place the sample close to the tip
5. Navigate the tip above the sample and carefully approach the surface, avoid crashing the tip into the surface as this may break the tip. Look for the edge of the sample and use this as

a hallmark for when the tip is close enough to the sample. Subsequently find a spot on the surface to further adjust the distance between tip and sample.

6. Locate where you want to image the sample
    (a) Image the corner(s) and center of the sample
7. Check the parameters before engaging.
    (a) Start by choosing a larger scan size (5-10 um).
    (b) Set the offset (X and Y) to 0.
    (c) Set the scan angle to 0.
    (d) Start with a scan rate of 3 Hz or larger.
    (e) Start with 256 samples/line (this may be increased to 1024 or 2048 for a higher image quality)
    (f) Adjust the feedback loop:
        i. Integral gain: 1.00
        ii. Proportional gain: 5.00
        iii. Amplitude setpoint will be at some value [nm]
8. Engage the tip and adjust the parameters to get a clear image (both height sensor, amplitude and phase)
9. Adjust the amplitude setpoint until you get a signal. Correct the feedback loop with the proportional gain and then the integral gain to reduce noise. Decrease the scan rate for a clearer signal if needed.
10. Adjust the scan angle to get the terraces vertically aligned.
11. Start recording an image (use 1024 samples/line or more to get a high-quality image). Make sure to select the directory correctly and name the image.
12. Click “Withdraw” to withdraw the tip from the sample and return to “navigate” to move the tip to a different location on the sample or to change sample.
13. When finished, go to “navigate” to remove the tip from the sample and remove the sample. If you are the last user of the AFM, remove the tip and place it back in its case. Close the program.

6.3.2 Substrate images

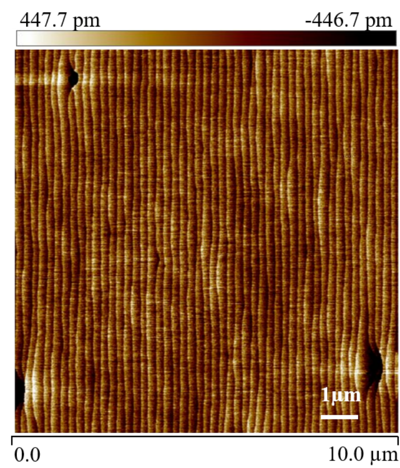

Figure 6.3: AFM of substrate used for deposition of R2 The substrate showed very distinct terraces with holes present in the surface structure.

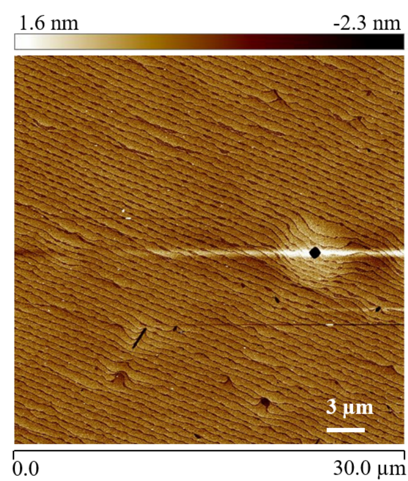

Figure 6.4: AFM of substrate used for deposition of Shin6_5 The substrate showed very distinct terraces with holes present in the surface structure.

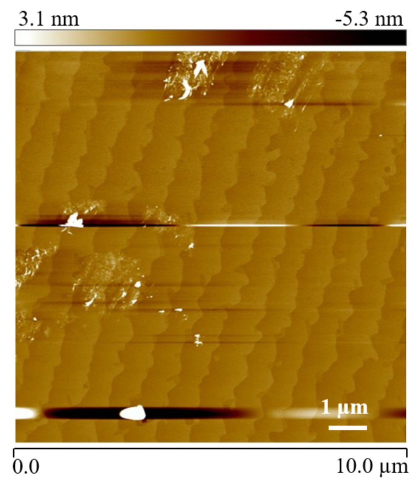

Figure 6.5: AFM of substrate used for deposition of Shin18_7 The substrate showed distinct terraces and no holes were detected.

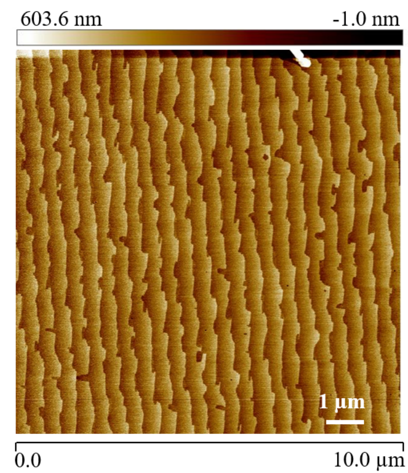

Figure 6.6: AFM of substrate used for deposition of Shin18_9 The substrate showed distinct terraces and no holes were detected.

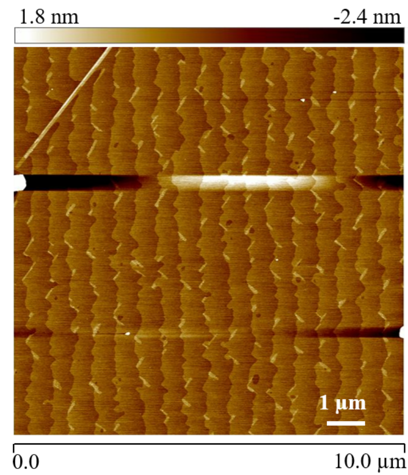

Figure 6.7: AFM of substrate used for deposition of Shin20_1 The substrate showed distinct terraces and no holes were detected. The small squares/lines present may be SrO and SrO+TiO_2 leftovers from surface termination.

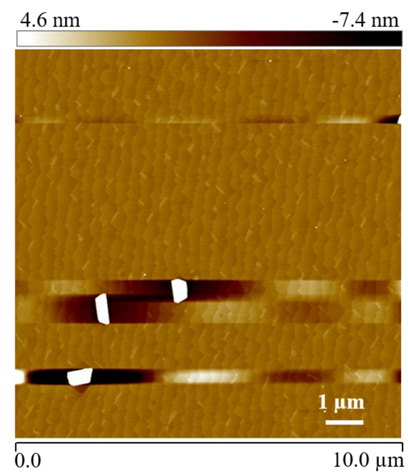

Figure 6.8: AFM of substrate used for deposition of Shin20_5 The substrate showed distinct terraces and no holes were detected. The small squares/lines present may be SrO and SrO+TiO_2 leftovers from surface termination.

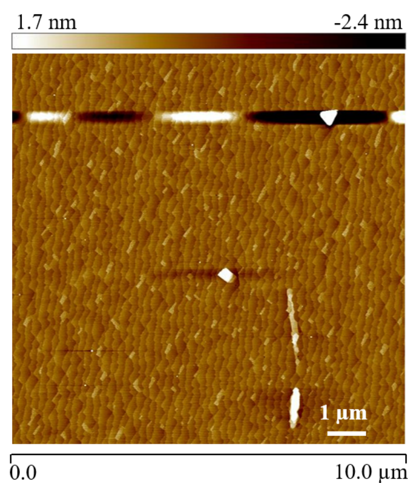

Figure 6.9: AFM of substrate used for deposition of Shin20_9 Deposition time: 30 minutes.The substrate showed distinct terraces and no holes were detected. The small squares/lines present may be SrO and SrO+TiO_2 leftovers from surface termination.

6.3.3 Sample images

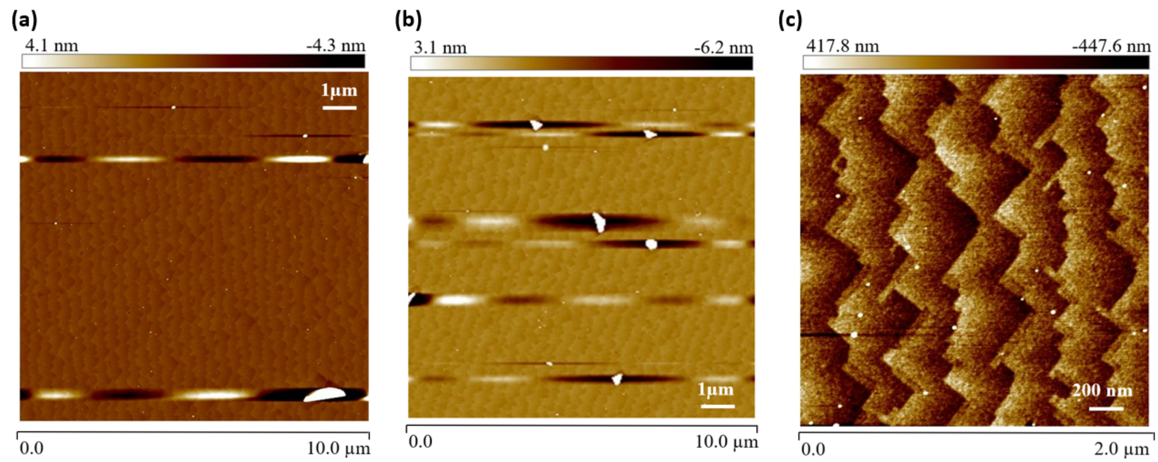

Figure 6.10: AFM of shin18_2 Deposition time: 4 minutes. Deposition pressure: 2.00 10^{-6} mbar. Fluence: 9 J/cm^2. a-c) AFM images in two sizes (10x10 and 2x2 μm) showing terraces.

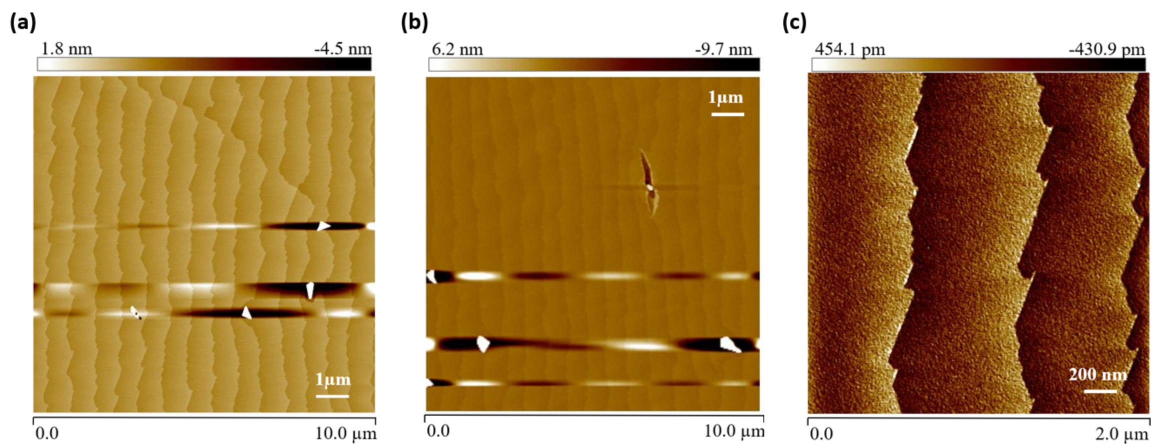

Figure 6.11: AFM of shin18_6 Deposition time: 4 minutes. Deposition pressure: 2.00 10^{-6} mbar. Fluence: 3 J/cm^2. a-c) AFM images in two sizes (10x10 and 2x2 μm) showing terraces.

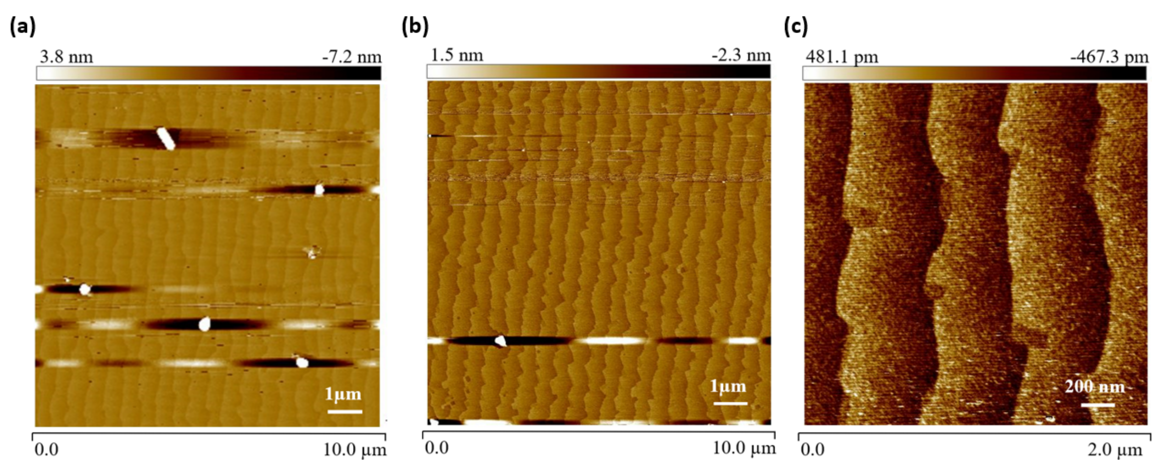

Figure 6.12: AFM of shin18_8 Deposition time: 4 minutes. Deposition pressure: 2.00 10^{-6} mbar. Fluence: 9 J/cm^2. a-c) AFM images in two sizes (10x10 and 2x2 μm) showing terraces.

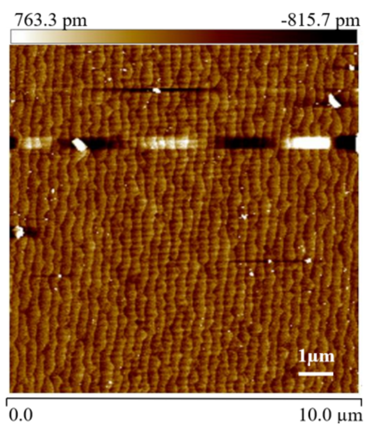

Figure 6.13: AFM of shin20_1 Deposition time: 4 minutes. Deposition pressure: 1.50 10^{-6} mbar. Fluence: 6 J/cm^2. 10x10 μm AFM image showing terraces.

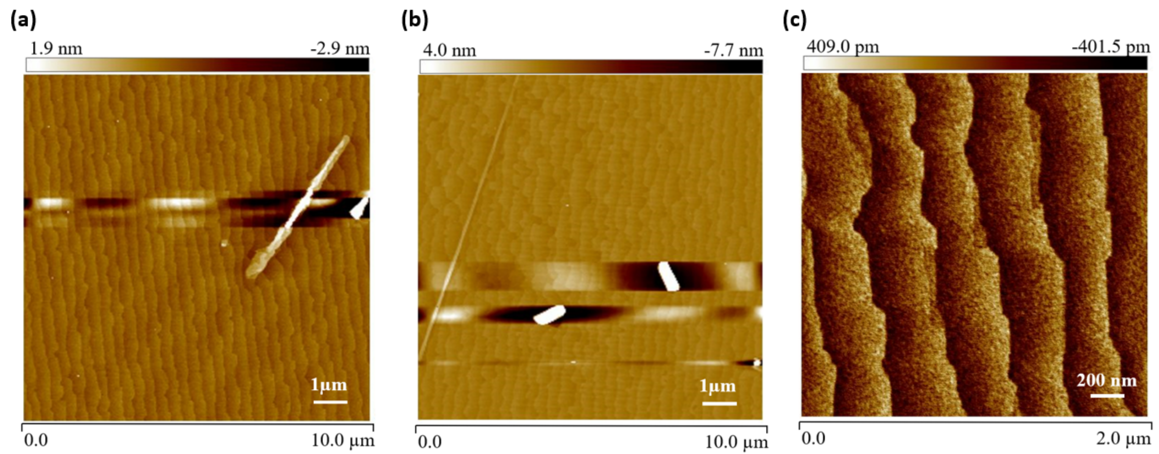

Figure 6.14: AFM of shin20_2 Deposition time: 4 minutes. Deposition pressure: 2.00 10^{-6} mbar. Fluence: 6 J/cm^2. a-c) AFM images in two sizes (10x10 and 2x2 μm) showing terraces.

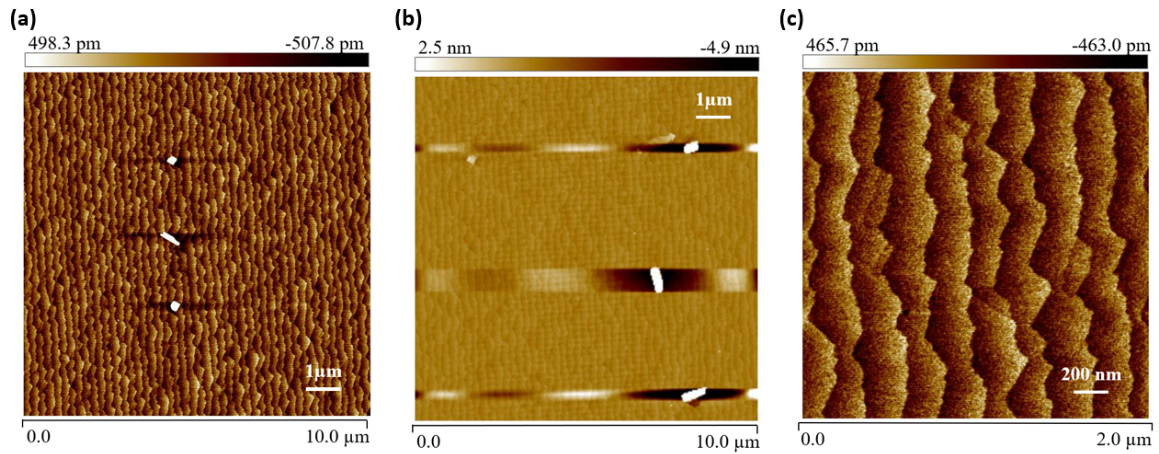

Figure 6.15: AFM of shin20_4 Deposition time: 4 minutes. Deposition pressure: 2.00 10^{-6} mbar. Fluence: 6 J/cm^2. a-c) AFM images in two sizes (10x10 and 2x2 μm) showing terraces.

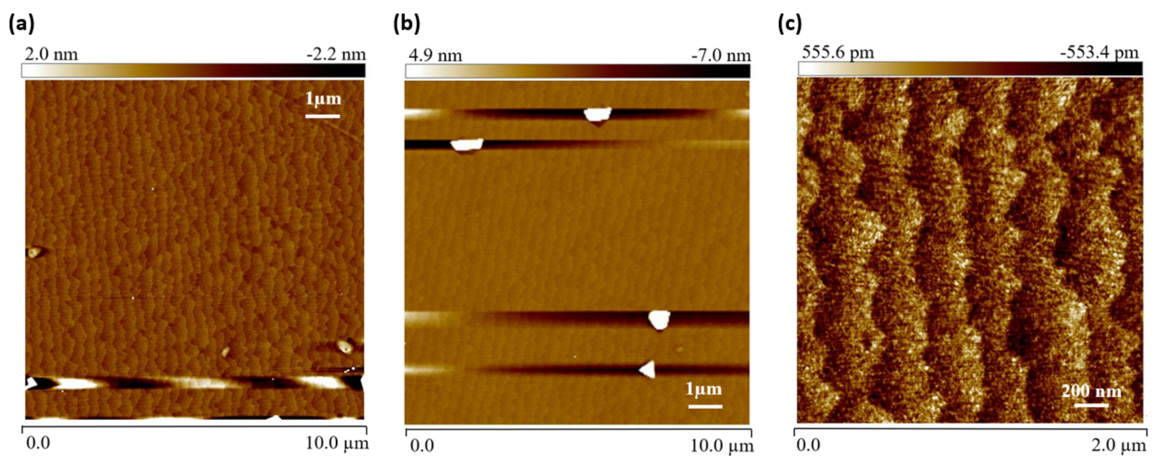

Figure 6.16: AFM of shin20_5 Deposition time: 30 minutes. Deposition pressure: 1.00 10^{-6} mbar. Fluence: 6 J/cm^2. a-c) AFM images in two sizes (10x10 and 2x2 μm) showing terraces.

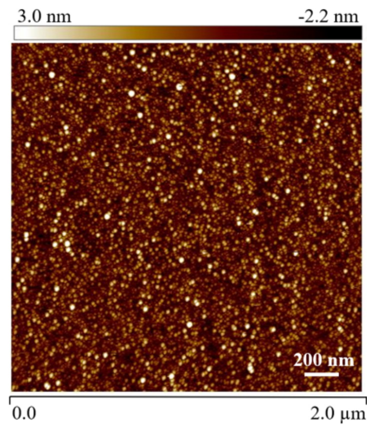

Figure 6.17: AFM of shin20_6 Deposition time: 30 minutes. Deposition pressure: 1.00 10^{-6} mbar. Fluence: 9 J/cm^2. 2x2 μm AFM image showing no visible terraces.

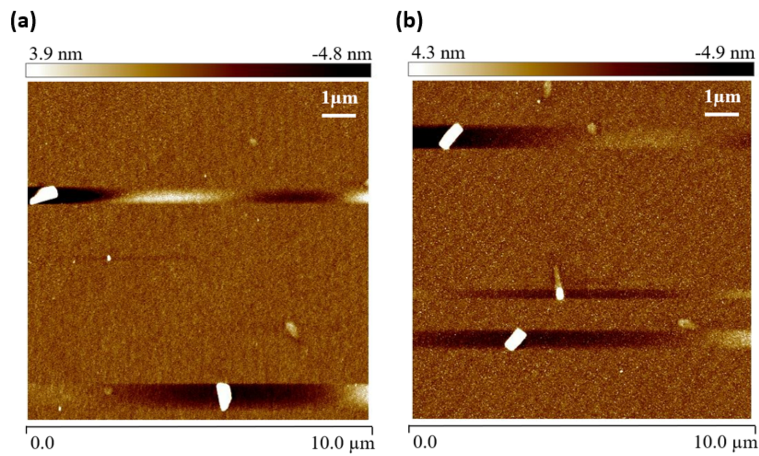

Figure 6.18: AFM of shin20_8 Deposition time: 30 minutes. Deposition pressure: 1.00 10^{-6} mbar. Fluence: 9 J/cm^2. a-b) Two 10x10 μm AFM images showing indistinct terraces.

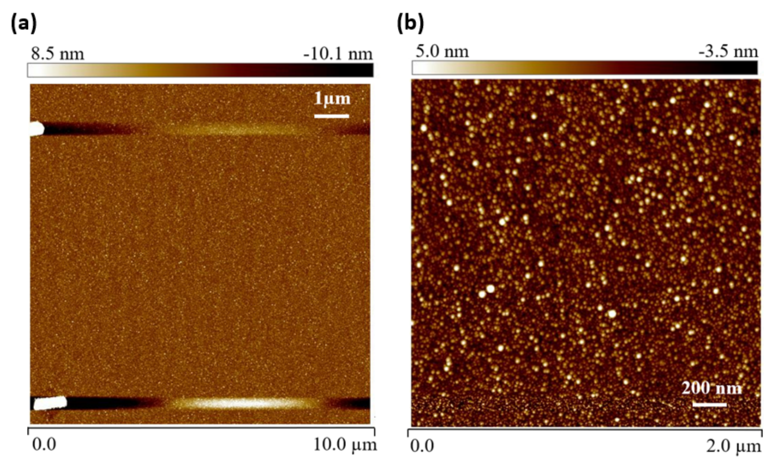

Figure 6.19: AFM of shin20_9 Deposition time: 30 minutes. Deposition pressure: 1.00 10^{-6} mbar. Fluence: 6 J/cm^2. a) 10x10 μm AFM image showing indistinct terraces. b) 2x2 μm AFM image where the terraces are no longer distinctive.

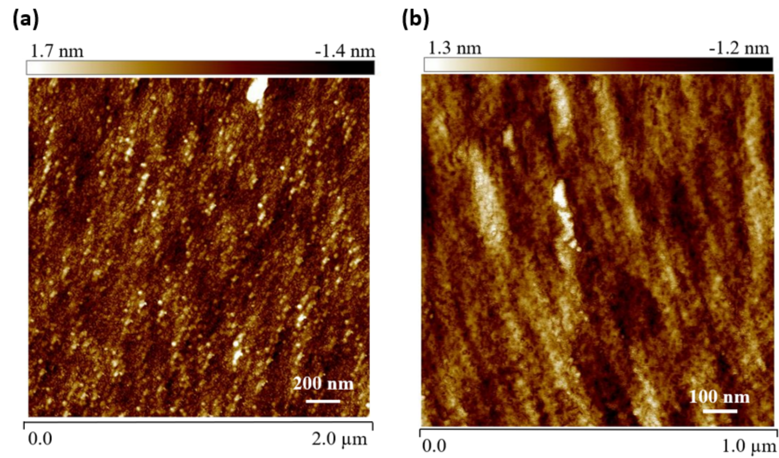

Figure 6.20: AFM of shin23_3 Deposition time: 30 minutes. Deposition pressure: 1.00 10^{-6} mbar. Fluence: 3 J/cm^2. a-b) 10x10 and 2x2 μm AFM images showing no visible terraces.

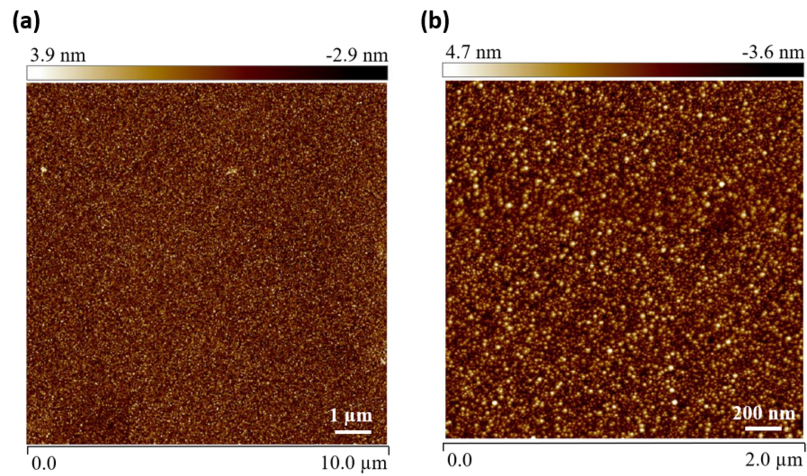

Figure 6.21: AFM of shin23_4 Deposition time: 30 minutes. Deposition pressure: 1.00 10^{-6} mbar. Fluence: 3 J/cm^2. a-b) 10x10 and 2x2 μm AFM images showing no visible terraces.

6.4 Scanning electron microscopy

6.4.1 Protocol

This protocol for cross-section SEM imaging has been provided by PhD student Raphael Anacleto.

1. Scribe the back side of your substrate with a scribing pencil.
2. Using the scratch in the substrate, press with precision pliers to direct fracture of the substrate.
3. When a non-conductive material is imaged, the electrons shot onto the sample surface don't have a path to the ground potential, causing them to accumulate on the surface. So, you must coat the analyzed surface with high-conductivity materials, in this case, 5 nm of Ag was used.
4. The sample was attached to a sample holder with the cross-section surface towards up (to the electron beam) and the thin film facing the carbon tape attached to the sample holder.
5. After that the samples was introduced to the SEM chamber vacuumed in the range of 10^{-7} mbar, and with conditions specified in the images made (working distance, potential etc.).

6.4.2 Images

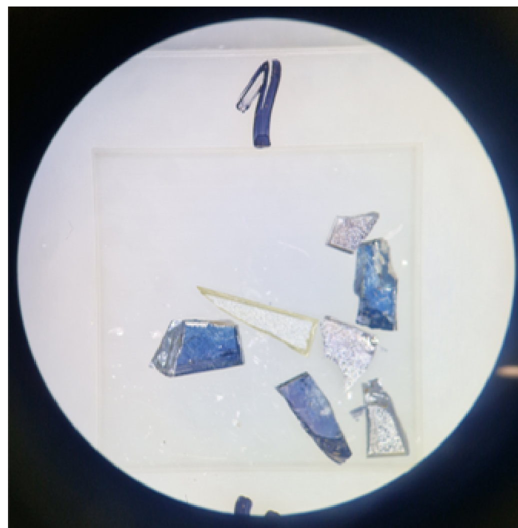

Figure 6.22: bla bla

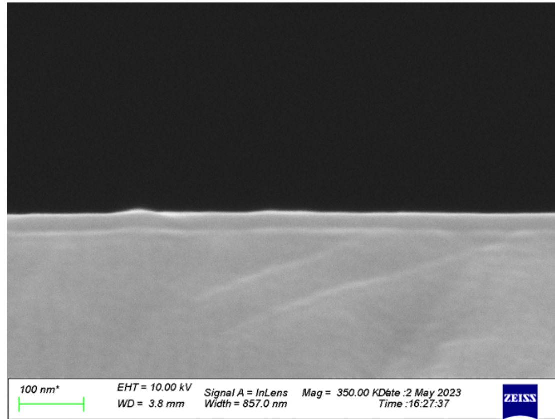

Figure 6.23: bla bla

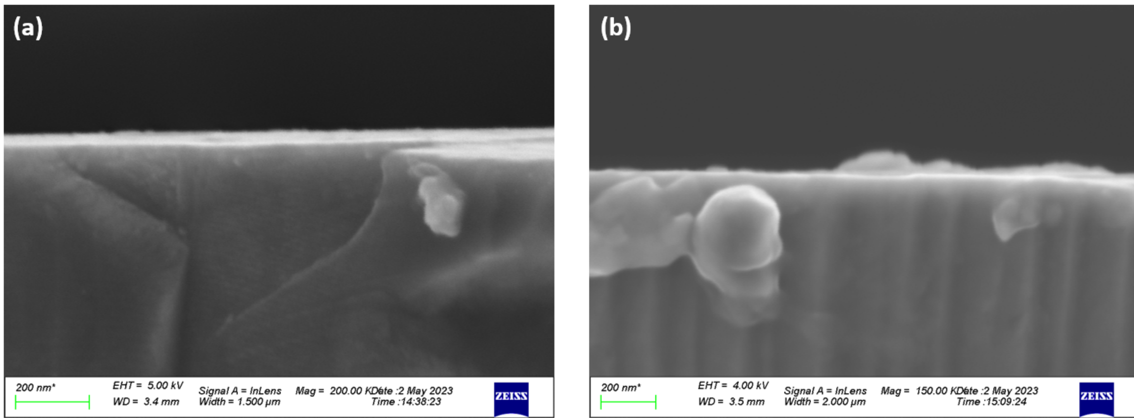

Figure 6.24: bla bla

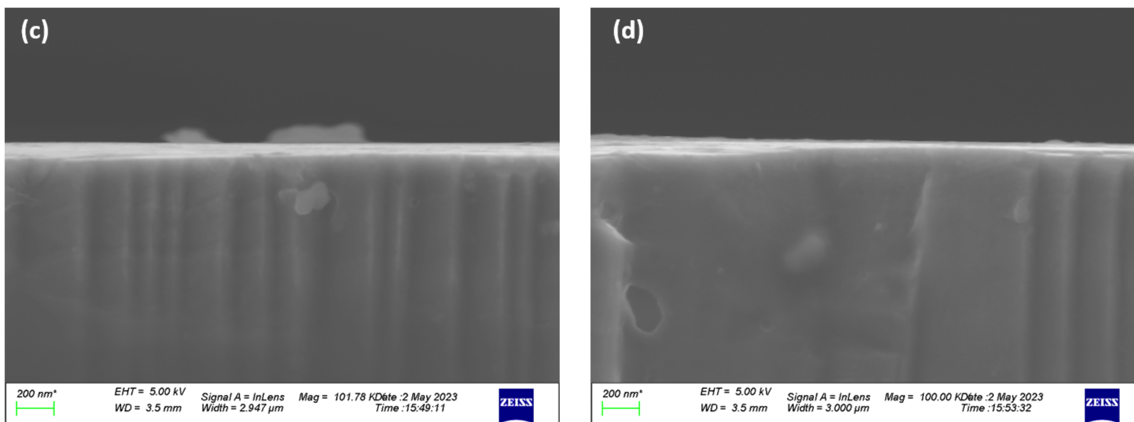

Figure 6.25: bla bla

6.5 X-ray crystallography

6.5.1 Protocol

1. Align the sample with the x-ray beam. This can be done manually or automatically.
2. Select the program you want to run.
   (a) For x-ray diffraction choose the $2\theta/2\theta$ scan.
   (b) For x-ray reflectometry choose $\omega/2\theta$ scan.
3. Make sure to align the x-ray beam with the STO substrate interface.
4. Chose scan rate and range.
5. Run scan.
6. When the scan is done, you can either treat the data in the Global fit software or use origin.

6.5.2 Supplementary data

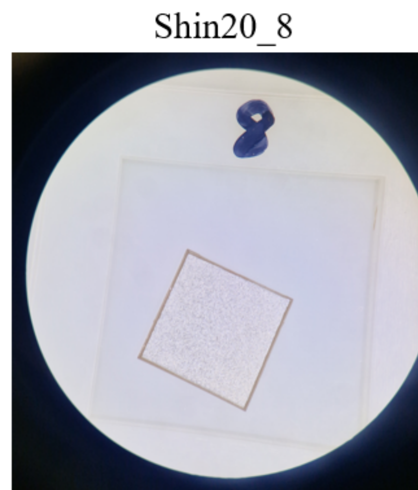

Figure 6.26: Shin20_8 Opical microscopy image of Shin20_8 post deposition.

Oxide	hkl	d [Å]	θ [rad]	2θ
STO	001	3.905	0.198	22.753
	002	1.952	0.405	46.472
GAO	004	1.977	0.400	45.845

Table 6.6: The calculated reference peak positions for STO (001 and 002) and GAO (004). hkl refers to Miller indices. d is the lattice constant for the designated plane. θ is the diffraction peak in radians. 2θ is the diffraction peak position in degrees. The values are calculated from using Bragg's law.

Fluence / Plane	**3 J/cm^2**		**6 J/cm^2**		**9 J/cm^2**	
Reference	**Shin23_3**	**Shin23_4**	**Shin20_5**	**Shin20_9**	**Shin20_6**	**Shin20_8**
001 STO (22.753)	22.673	22.664	22.666	22.678	22.614	22.646
002 STO (46.472)	46.376	46.376	46.357	46.375	46.330	46.371
004 GAO (45.845)	45.191	45.072	44.657	44.936	44.902	44.794

Table 6.7: Table giving a complete overview of the diffraction peak position for each of the six samples investigated by XRD.

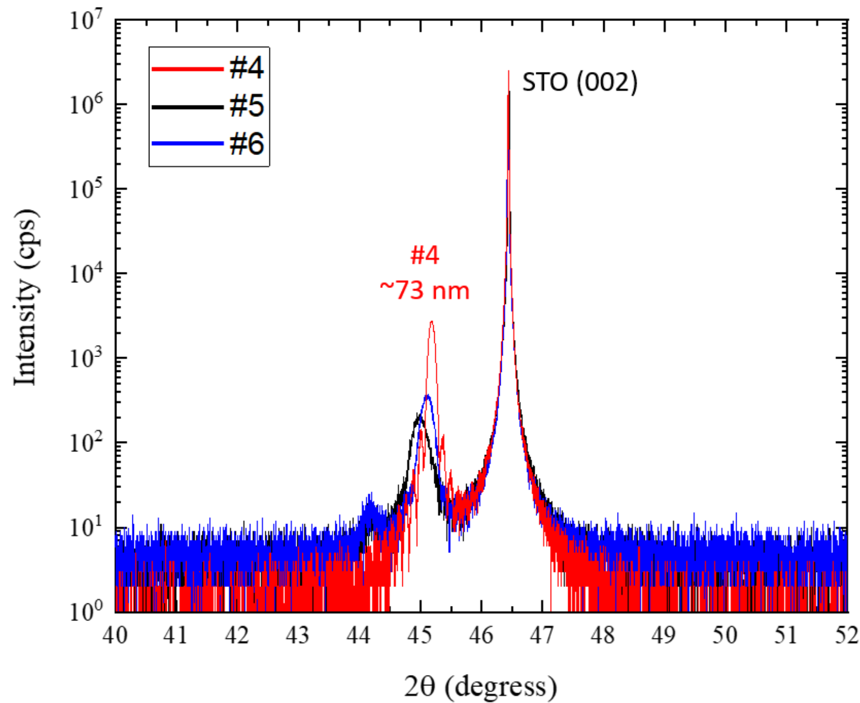

Figure 6.27: XRD data of thick thin films of GAO/STO $2\theta/2\theta$ scans of Shin7_4 (red), Shin7_5 (black) and Shin7_6 (blue). Shin7_4 showed Laue oscillations which were used to estimate the thickness of the thin film, depicted to be ∼73 nm. The data is presented as recieved and was conducted by Dr. Shinhee Yun.

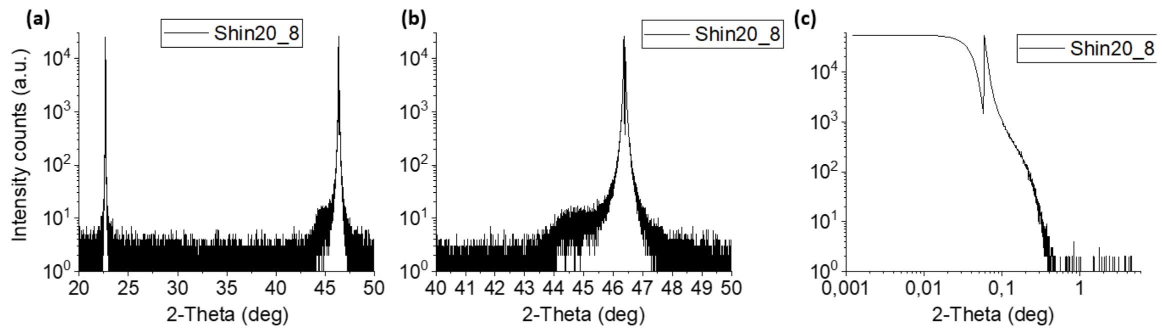

Figure 6.28: x-ray crystallography of shin20-8 Fluence: 9 J/cm^2, background pressure: 1.00E-06 mbar. a) XRD 20-50 2θ. b) XRD 40-50 2θ. a) XRR 0-2 2θ.

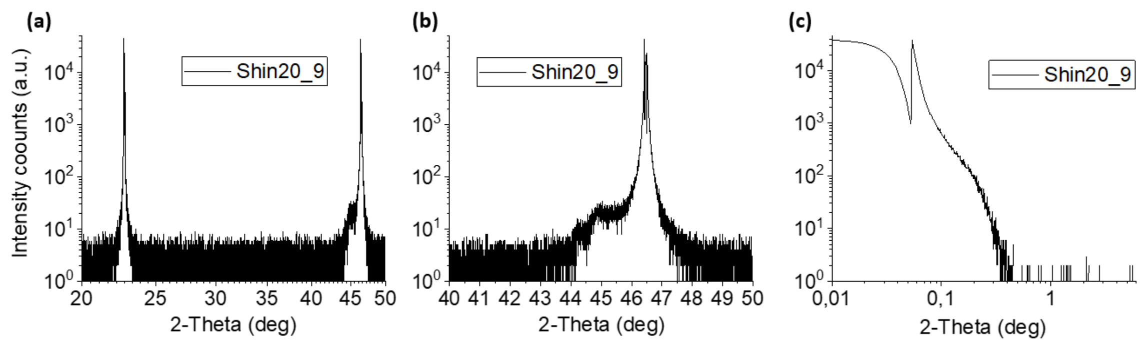

Figure 6.29: x-ray crystallography of shin20-9 Fluence: 6 J/cm^2, background pressure: 1.00E-06 mbar. a) XRD 20-50 2θ. b) XRD 40-50 2θ. a) XRR 0-2 2θ.

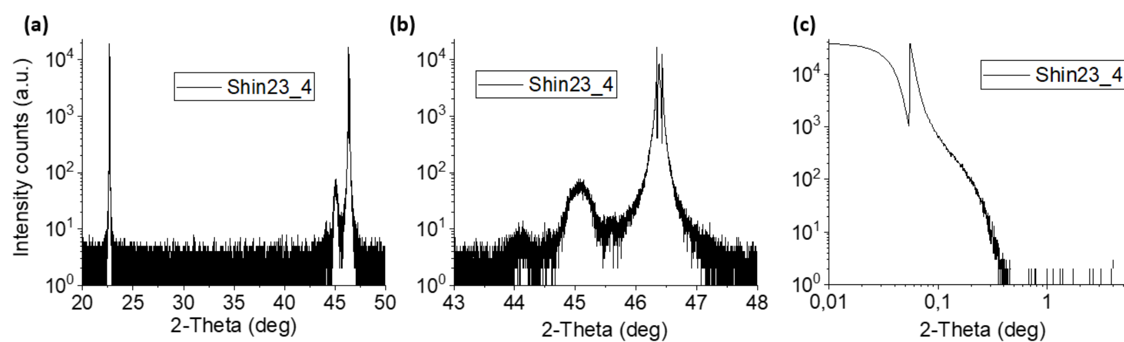

Figure 6.30: x-ray crystallography of shin23-4 Fluence: 3 J/cm^2, background pressure: 1.00E-06 mbar. a) XRD 20-50 2θ. b) XRD 43-48 2θ. a) XRR 0-2 2θ.

6.6 Electrical characterization

Figure 6.31: 16 Tesla Cryostat setup

6.6.1 Protocol

1. Prepare the sample by wire bonding it to a chip carrier. Perform 4 point-probe resistance measurements to both permutations (a and b) to check the bonds.

2. Place it in the sample holder for the cryostat. Gently place the sample holder (stick) in the sample insert and tighten the clam. Connect current source and voltage to the sample holder. Check the 4 point-probe resistance again to see that the sample is placed correctly, and all bonds are intact.

3. Open the valve connected to the turbo pump. Turn on the turbo pump and start pumping the system. Wait until the pressure is below $\sim$ 4E-05 mbar. CLOSE the valve and turn off the turbo pump.

4. The space where the sample is located has now been pumped and the second valve can be opened, opening up to the space containing the heating/cooling element and magnet.

5. Slowly insert the sample into the cryostat until it is all the way down. At this state, the temperature in the cryostat should be at 300K. If this is not the case, heat up the cryostat BEFORE lowering the sample.

6. Setup the MATLAB script for measurements.

7. Set the configuration to a/b and do a time sweep at 300K for R_a/R_b. Do this for both configurations (a and b).

8. Set the configuration to do a Hall measurement and set the magnet to go to -16 T. When at -16 T start the sweep from -16 T to 16 T at 300 K. Set the measurement to sweep between -16 T and 16 T, and 16 T and -16 T, at 300K, 250K, 200K, 150K, 100K, 50K, 25K, 20K, 15K, 10K, 5K and 2K.

9. Before starting the Hall measurement, if necessary, do an MR at 300K before starting to cool down.

10. At 2K, if necessary, do an MR at 2K before proceeding.

11. Measure the sheet resistance from 2K to 300K for configuration a.

12. If R of configuration of a and b differ much then cool down to 2K and measure the sheet resistance from 2K to 300K for configuration b as well.

13. When finished, heat up the cryostat. At 300K the sample can be pulled out from the cryostat and the second valve must be closed before pulling out the sample holder, to keep the vacuum intact. Take out the current and voltage wires.

14. Close the second valve, secure the sample holder stick so that it does not slip when the clamp is loosen. Open slightly for the nitrogen valve to remove the vacuum. Take out the sample holder and take out the sample.

15. Put back the sample holder in the insert and place back the clamp.

6.6.2 Suplementary Hall data

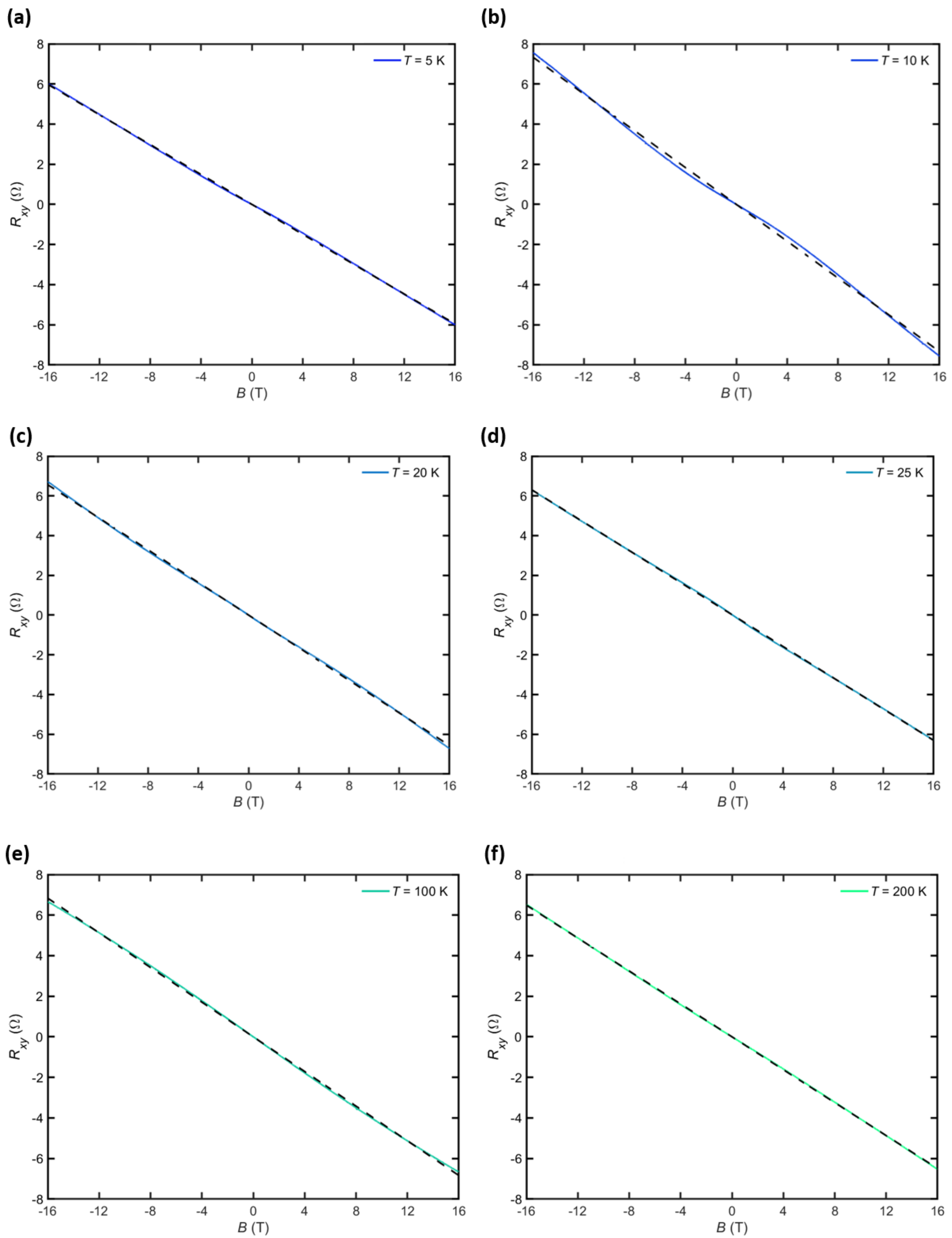

Figure 6.32: Shin12_6 Hall curves for temperatures T=5K, 10K, 20K, 25K, 100K and 200K.

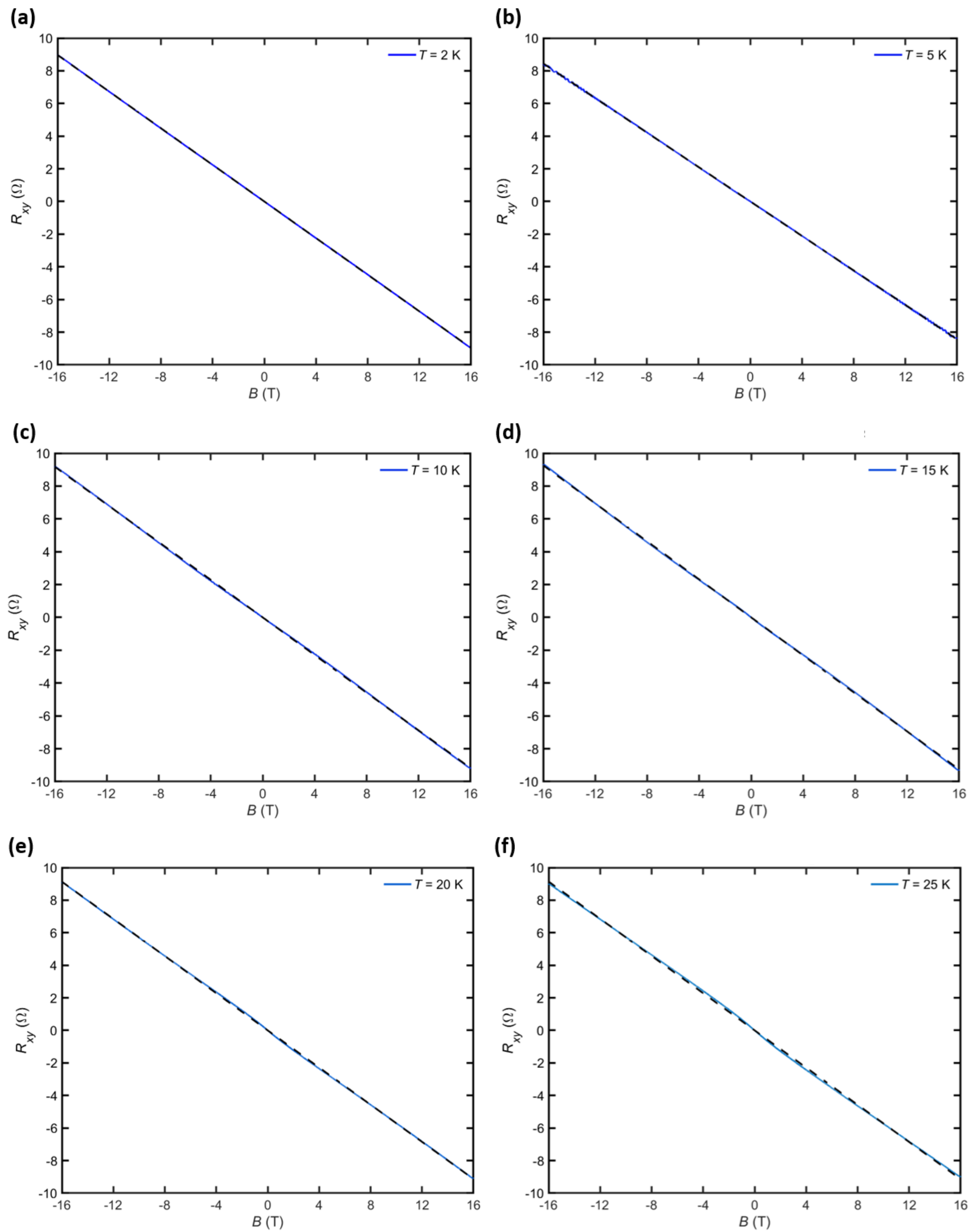

Figure 6.33: Shin18_1 Hall curves for temperatures T=2K, 5K, 10K, 15K, 20K and 25K

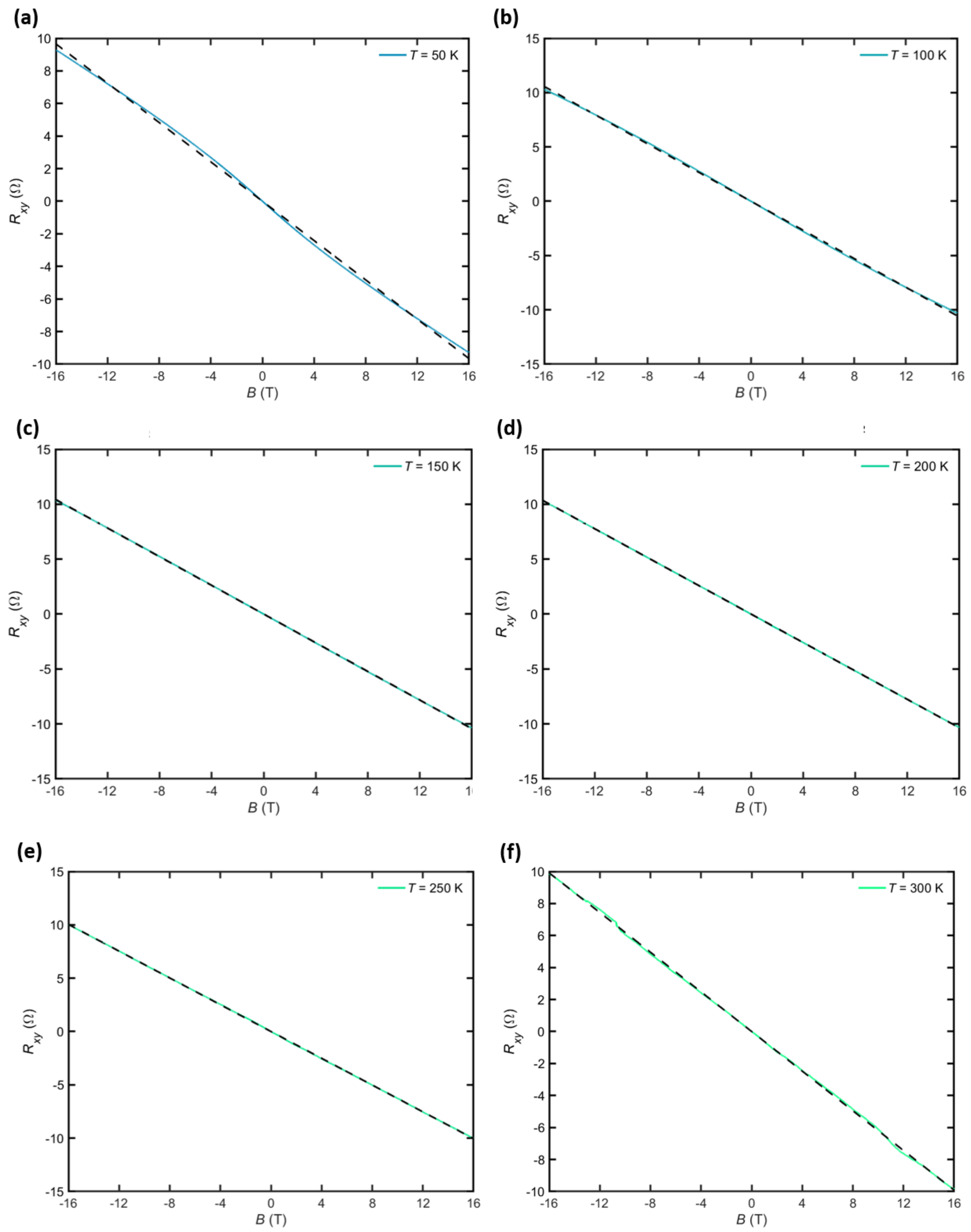

Figure 6.34: Shin18_1 Hall curves for temperatures T=50K, 100K, 150K, 200K, 250K and 300K.

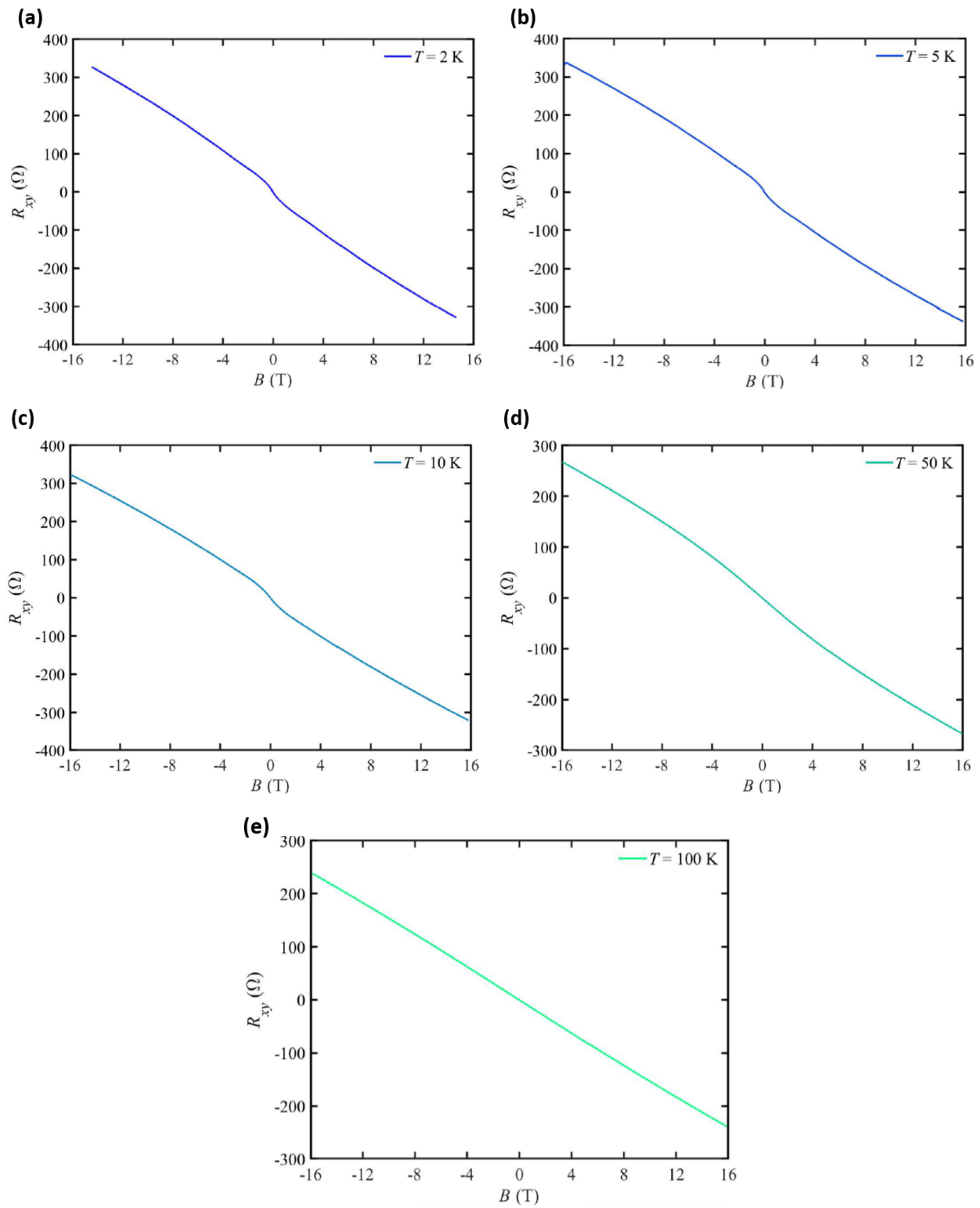

Figure 6.35: Shin18_7 Hall curves for temperatures T=2K, 5K, 10K, 50K and 100K.

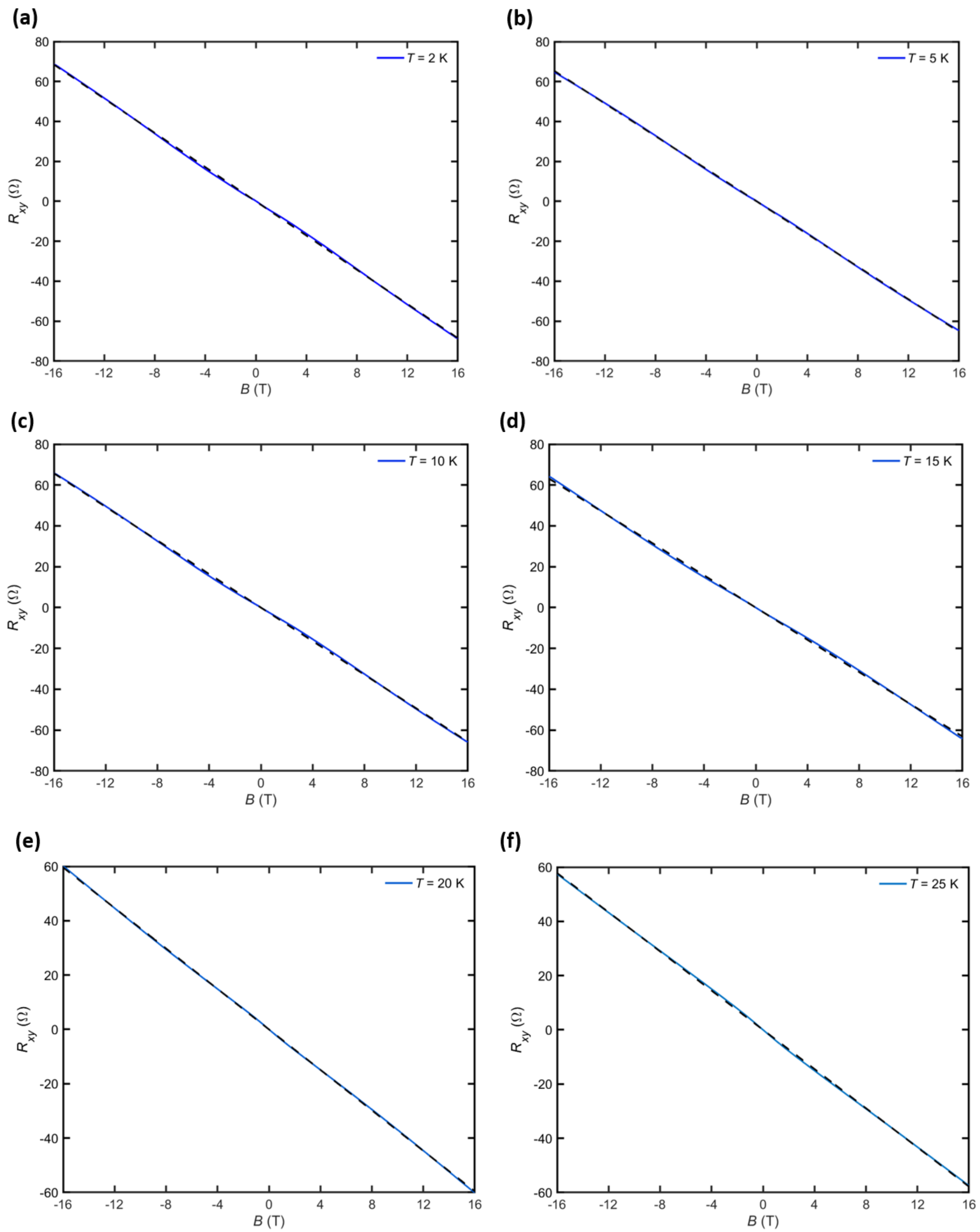

Figure 6.36: Shin18_8 Hall curves for T=2K, 5K, 10K, 15K, 20K and 25K

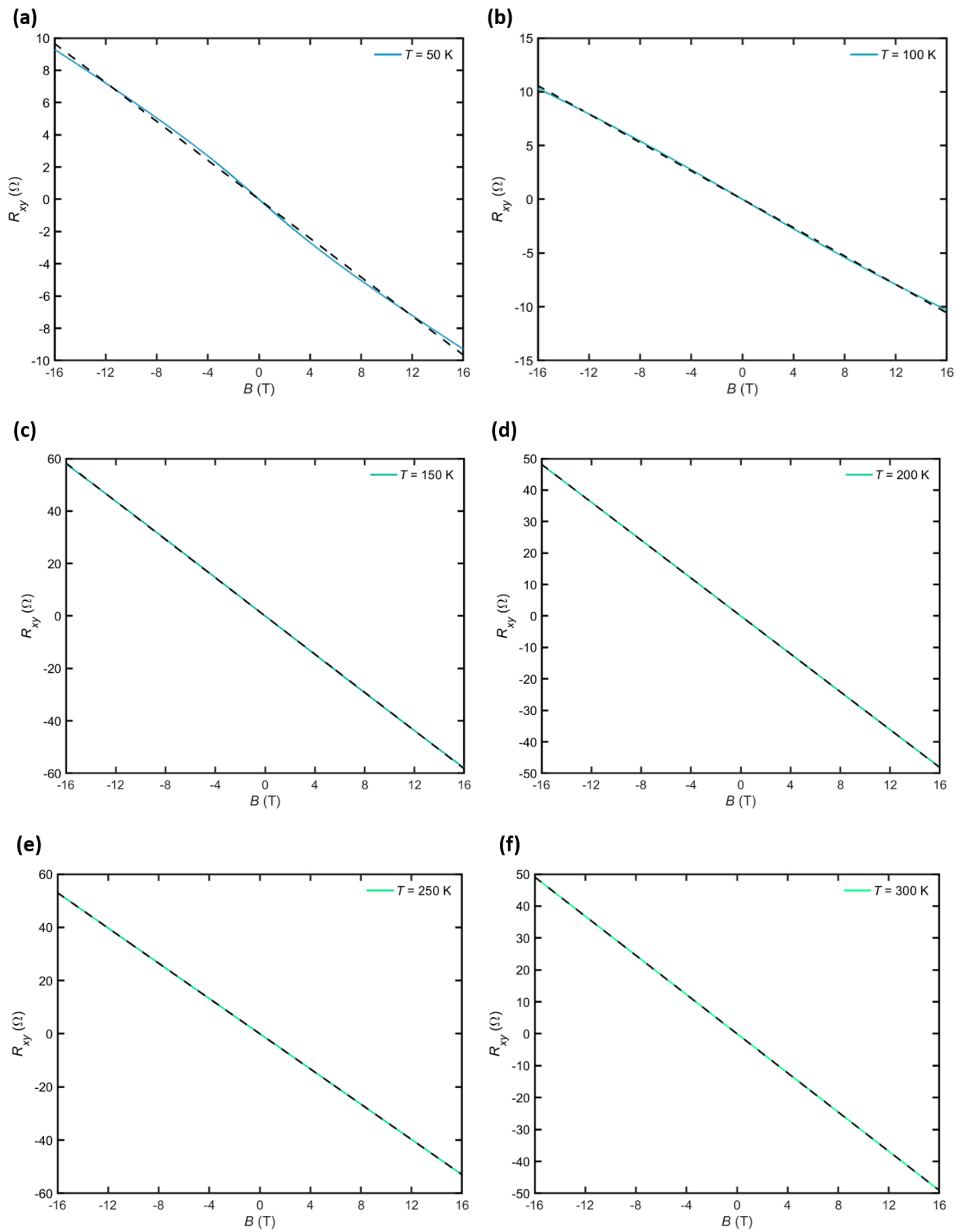

Figure 6.37: Shin18_8 Hall curves for temperatures T=50K, 100K, 150K, 200K, 250K and 300K.

6.7 Fluence and pressure dependency supplementary data

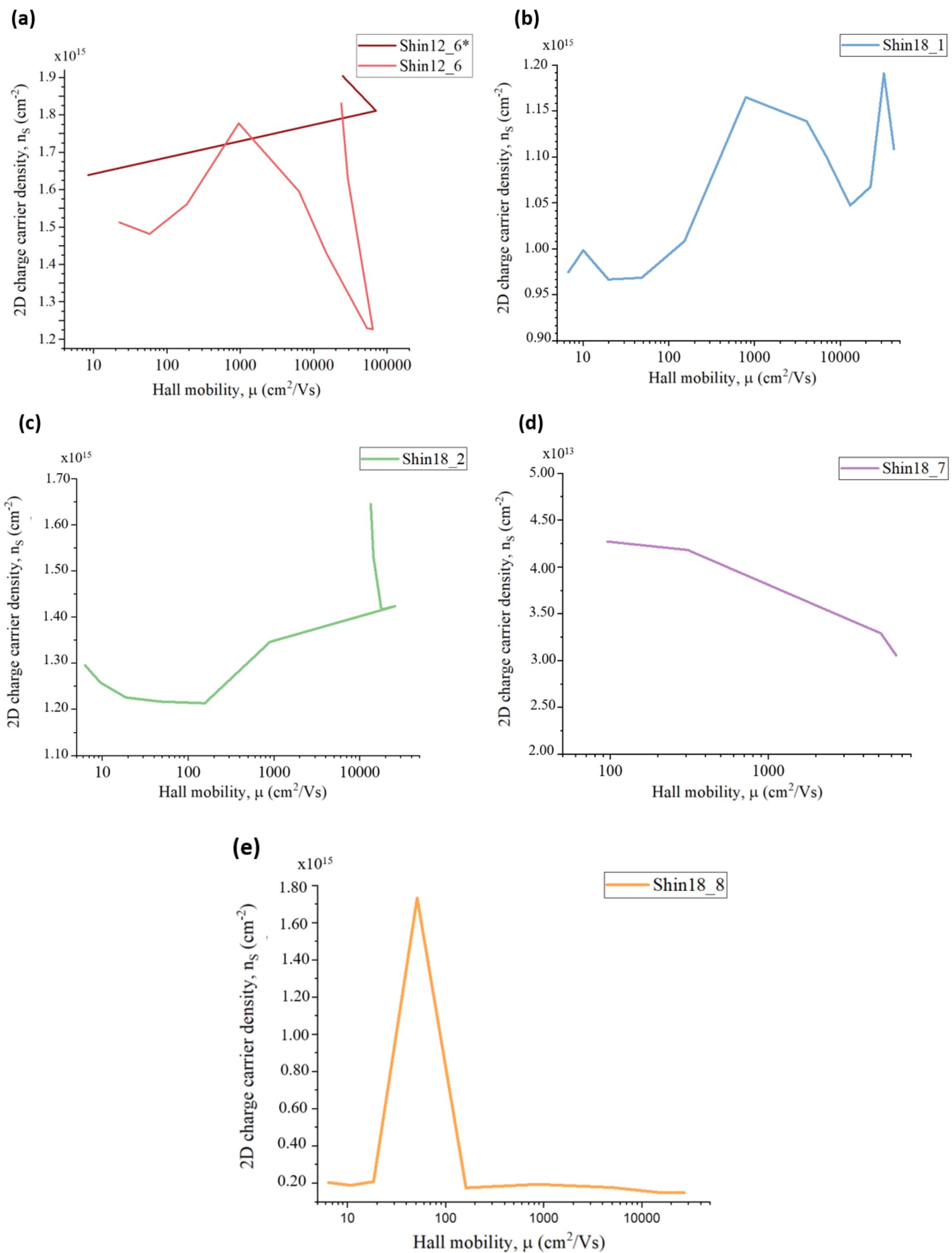

Figure 6.38: 2D Charge Carrier Densities as a function of Hall mobilities a) First and second measurement of Shin12_6. b) Shin18_1. c) Shin18_2. d) Shin18_7. e) Shin18_8.

6.8 Maintenance

6.8.1 Furnace room

Reorganization of the laboratory space and responsibility of training, procedures and maintenance of the tube furnace used for STO annealing.

6.8.2 Window polishing

The window that separates the beam line from the PLD vacuum chamber tends to decrease in transmission over time as ablated material accumulate on the inside of the window. The reduction in transmission will eventually impede the achievement of a high laser fluence. One potential solution to this issue is window polishing. At the time, there had not been established a protocol for window polishing. Therefore, an experiment was conducted using an old window with a low transmission of 54%. The window was polished using a diamond solution containing a solution of 5-chloro-2-methyl-4-isothiazolin-3-one and 2-methyl-2H-isothiazol-3-one (3:1). A cotton stick was used for polishing and pressure was applied while moving it in circular motions for a duration of 60 seconds. The transmission was subsequently measured. To assess the effect of the window on laser energy, measurements were performed with and without the window using a laser meter. The change in energy was used to calculate the transmission. The transmission was determined for two different acceleration voltages, namely 18kV and 21kV. When the transmission reached 70%, the polishing time was extended to 120 seconds, but later reduced back to 60 seconds.

After 10 minutes of polishing, the maximum transmission was achieved, beyond which it began to decline with continued polishing. This window polishing protocol has subsequently been employed for polishing vacuum windows as needed. The data obtained from this experiment and the window in question is depicted in Figure 6.39a-b.

6.8.3 Laser beam spot size management

The laser spot size was measured as a part of the laser beam optimization. The measured laser spot used for the depositions of GAO/STO is shown in Figure 6.40

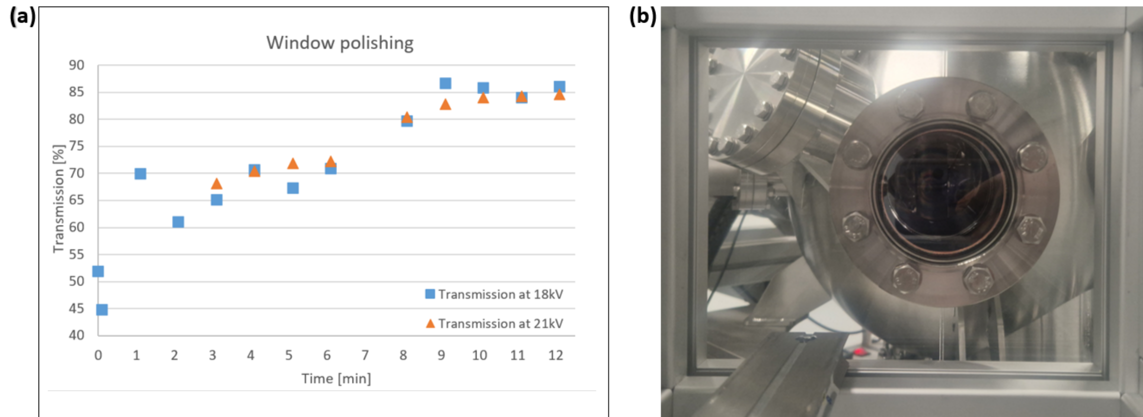

Figure 6.39: Window transmission optimization a) Window transmission as a function of polishing time. b) The window giving the laser pulses direct entrance to the PLD chamber.

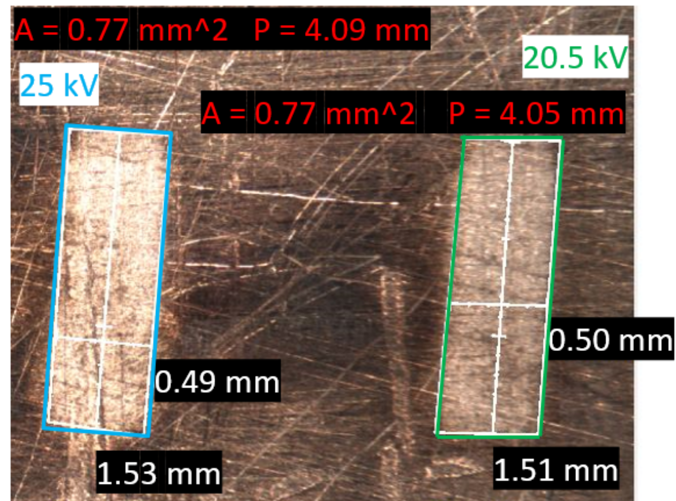

Figure 6.40: Laser spot size measurement The laser spot size was measured using two different laser acceleration voltages, 20.5kV and 25kV.

References

[1] Technologies that could transform how industries use energy | McKinsey.

[2] Energy Efficiency: The leading cause of energy demand peaking by 2033.

[3] High Mobility Material - an overview | ScienceDirect Topics.

[4] Global energy efficiency progress is accelerating, signalling a potential turning point after years of slow improvement - News.

[5] Po Dong, Young-Kai Chen, Guang-Hua Duan, and David T. Neilson. Silicon photonic devices and integrated circuits. *Nanophotonics*, 3(4-5):215–228, August 2014. Publisher: De Gruyter.

[6] H.S. Bennett, R. Brederlow, J.C. Costa, P.E. Cottrell, W.M. Huang, A.A. Immorlica, J.-E. Mueller, M. Racanelli, H. Shichijo, C.E. Weitzel, and Bin Zhao. Device and technology evolution for Si-based RF integrated circuits. *IEEE Transactions on Electron Devices*, 52(7):1235–1258, July 2005. Conference Name: IEEE Transactions on Electron Devices.

[7] Integrated circuit | Types, Uses, & Function | Britannica.

[8] Kaichen Zhu, Chao Wen, Areej A. Aljarb, Fei Xue, Xiangming Xu, Vincent Tung, Xixiang Zhang, Husam N. Alshareef, and Mario Lanza. The development of integrated circuits based on two-dimensional materials. *Nature Electronics*, 4(11):775–785, November 2021. Number: 11 Publisher: Nature Publishing Group.

[9] Humaira and Mamoona Asghar. *Limitation of Silicon Based Computation and Future Prospects*. March 2010. Pages: 561.

[10] Heike Riel. Quantum Computing Technology and Roadmap. In *ESSDERC 2022 - IEEE 52nd European Solid-State Device Research Conference (ESSDERC)*, pages 25–30, September 2022.

[11] Charles Kittel. *Introduction to solid state physics*. Wiley, Hoboken, NJ, 8th ed edition, 2005.

[12] M. Coll, J. Fontcuberta, M. Althammer, M. Bibes, H. Boschker, A. Calleja, G. Cheng, M. Cuoco, R. Dittmann, B. Dkhil, I. El Baggari, M. Fanciulli, I. Fina, E. Fortunato, C. Frontera, S. Fujita, V. Garcia, S. T.B. Goennenwein, C. G. Granqvist, J. Grollier, R. Gross, A. Hagfeldt, G. Herranz, K. Hono, E. Houwman, M. Huijben, A. Kalaboukhov, D. J. Keeble, G. Koster, L. F. Kourkoutis, J. Levy, M. Lira-Cantu, J. L. MacManus-Driscoll, Jochen Mannhart, R. Martins, S. Menzel,

T. Mikolajick, M. Napari, M. D. Nguyen, G. Niklasson, C. Paillard, S. Panigrahi, G. Rijnders, F. Sánchez, P. Sanchis, S. Sanna, D. G. Schlom, U. Schroeder, K. M. Shen, A. Siemon, M. Spreitzer, H. Sukegawa, R. Tamayo, J. van den Brink, N. Pryds, and F. Miletto Granozio. Towards Oxide Electronics: a Roadmap. *Applied Surface Science*, 482:1–93, 2019.

[13] Y. Tokura and N. Nagaosa. Orbital Physics in Transition-Metal Oxides. *Science*, 288(5465):462–468, April 2000. Publisher: American Association for the Advancement of Science.

[14] Ethan C. Ahn. 2D materials for spintronic devices. *npj 2D Materials and Applications*, 4(1):1–14, June 2020. Number: 1 Publisher: Nature Publishing Group.

[15] Y. Z. Chen, N. Bovet, F. Trier, D. V. Christensen, F. M. Qu, N. H. Andersen, T. Kasama, W. Zhang, R. Giraud, J. Dufouleur, T. S. Jespersen, J. R. Sun, A. Smith, J. Nygård, L. Lu, B. Büchner, B. G. Shen, S. Linderoth, and N. Pryds. A high-mobility two-dimensional electron gas at the spinel/perovskite interface of -Al2O3/SrTiO3. *Nature Communications*, 4:1371, 2013.

[16] Manuel Bibes and Agnes Barthelemy. Oxide Spintronics. *IEEE Transactions on Electron Devices*, 54, June 2007.

[17] Alekha Tyagi, Soma Banerjee, Jayesh Cherusseri, and Kamal K. Kar. Characteristics of Transition Metal Oxides. In Kamal K. Kar, editor, *Handbook of Nanocomposite Supercapacitor Materials I: Characteristics*, Springer Series in Materials Science, pages 91–123. Springer International Publishing, Cham, 2020.

[18] WILLIAM R. Frensley. Chapter 1 - Heterostructure and Quantum Well Physics. In Norman G. Einspruch and William R. Frensley, editors, *VLSI Electronics Microstructure Science*, volume 24 of *Heterostructures and Quantum Devices*, pages 1–24. Elsevier, January 1994.

[19] Ricci Erlandsen, Rasmus Tindal Dahm, Felix Trier, Mario Scuderi, Emiliano Di Gennaro, Alessia Sambri, Charline Kaisa Reffeldt Kirchert, Nini Pryds, Fabio Miletto Granozio, and Thomas Sand Jespersen. A Two-Dimensional Superconducting Electron Gas in Freestanding LaAlO $_3$$ /SrTiO $_3$$ Micromembranes. *Nano Letters*, 22(12):4758–4764, 2022.

[20] Ming-Shiu Tsai, Chi-Sheng Li, Shih-Ting Guo, Ming-Yuan Song, Akhilesh Kr Singh, Wei-Li Lee, and M.-W. Chu. Off-Stoichiometry Driven Carrier Density Variation at the Interface of LaAlO3/SrTiO3. *Scientific Reports*, 7(1):1770, May 2017. Number: 1 Publisher: Nature Publishing Group.

[21] Sumilan Banerjee, Onur Erten, and Mohit Randeria. Ferromagnetic exchange, spin-orbit coupling and spiral magnetism at the $LaAlO_3$$/$SrTiO_3$$ interface. *Nature Physics*, 9(10):626–630, August 2013.

[22] Kitae Eom, Hanjong Paik, Jinsol Seo, Neil Campbell, Evgeny Tsymbal, Sang Oh, Mark Rzchowski, Darrell Schlom, and Chang-Beom Eom. Oxide Two-Dimensional Electron Gas with High Mobility at Room-Temperature. *Advanced Science*, 9, April 2022.

[23] Yun-Yi Pai, Anthony Tylan-Tyler, Patrick Irvin, and Jeremy Levy. Physics of SrTiO3-based heterostructures and nanostructures: a review. *Reports on Progress in Physics*, 81(3):036503, February 2018. Publisher: IOP Publishing.

[24] Dennis Valbjørn Christensen, Felix Trier, Wei Niu, Yulin Gan, Yu Zhang, Thomas Sand Jespersen, Yunzhong Chen, and Nini Pryds. Stimulating Oxide Heterostructures: A Review on Controlling $SrTiO_3$$ -Based Heterointerfaces with External Stimuli. *Advanced Materials Interfaces*, 6(21):1900772, November 2019.

[25] Bharat Jalan, S. James Allen, Glenn E. Beltz, Pouya Moetakef, and Susanne Stemmer. Enhancing the electron mobility of SrTiO3 with strain. *Applied Physics Letters*, 98(13):132102, March 2011. Publisher: American Institute of Physics.

[26] Le Duc Anh, Shingo Kaneta, Masashi Tokunaga, Munetoshi Seki, Hitoshi Tabata, Masaaki Tanaka, and Shinobu Ohya. High-Mobility 2D Hole Gas at a SrTiO3 Interface. *Advanced Materials*, 32(14):1906003, 2020. _eprint: https://onlinelibrary.wiley.com/doi/pdf/10.1002/adma.201906003.

[27] A. Ohtomo and H. Y. Hwang. A high-mobility electron gas at the LaAlO3/SrTiO3 heterointerface. *Nature*, 427(6973):423–426, January 2004. Number: 6973 Publisher: Nature Publishing Group.

[28] Joseph A. Sulpizio, Shahal Ilani, Patrick Irvin, and Jeremy Levy. Nanoscale Phenomena in Oxide Heterostructures. *Annual Review of Materials Research*, 44(1):117–149, 2014. _eprint: https://doi.org/10.1146/annurev-matsci-070813-113437.

[29] Tausonite. https://www.mindat.org/min-3895.html.

[30] Shan-Lin Zhang, Hongqian Wang, Matthew Y. Lu, Ai-Ping Zhang, Liliana V. Mogni, Qinyuan Liu, Cheng-Xin Li, Chang-Jiu Li, and Scott A. Barnett. Cobalt-substituted SrTi0.3Fe0.7O3− :

a stable high-performance oxygen electrode material for intermediate-temperature solid oxide electrochemical cells. *Energy & Environmental Science*, 11(7):1870–1879, July 2018. Publisher: The Royal Society of Chemistry.

[31] Z. Zhong and Y. Lu. 11 - First-principle study of metal oxide thin films: Electronic and magnetic properties of confined d electrons. In Nini Pryds and Vincenzo Esposito, editors, *Metal Oxide-Based Thin Film Structures*, Metal Oxides, pages 245–261. Elsevier, January 2018.

[32] Rasmus Tindal Dahm and Ricci Erlandsen. Electrical characterisation of free-standing, superconducting LaAlO3/SrTiO3 micro-membranes. Master's thesis, University of Copenhagen, August 2019.

[33] R. C. Neville, B. Hoeneisen, and C. A. Mead. Permittivity of Strontium Titanate. *Journal of Applied Physics*, 43(5):2124–2131, May 1972. Publisher: American Institute of Physics.

[34] Wolter Siemons, Mark Huijben, Guus Rijnders, Dave H. A. Blank, Theodore H. Geballe, Malcolm R. Beasley, and Gertjan Koster. Dielectric-permittivity-driven charge carrier modulation at oxide interfaces. *Physical Review B*, 81(24):241308, 2010.

[35] J. H. Haeni, P. Irvin, W. Chang, R. Uecker, P. Reiche, Y. L. Li, S. Choudhury, W. Tian, M. E. Hawley, B. Craigo, A. K. Tagantsev, X. Q. Pan, S. K. Streiffer, L. Q. Chen, S. W. Kirchoefer, J. Levy, and D. G. Schlom. Room-temperature ferroelectricity in strained SrTiO3. *Nature*, 430(7001):758–761, August 2004. Number: 7001 Publisher: Nature Publishing Group.

[36] K. A. Müller and H. Burkard. SrTi${\mathrm{O}}_{3}$: An intrinsic quantum paraelectric below 4 K. *Physical Review B*, 19(7):3593–3602, April 1979. Publisher: American Physical Society.

[37] H. P. R. Frederikse and W. R. Hosler. Hall Mobility in $SrTiO_3$\$. *Physical Review*, 161(3):822, 1967.

[38] Dennis Valbjørn Christensen, Y. Frenkel, P. Schütz, Felix Trier, S. Wissberg, R. Claessen, B. Kalisky, A. Smith, Y. Z. Chen, and Nini Pryds. Electron Mobility in -Al2O3/SrTiO3. *Physical Review Applied*, 9(5), 2018.

[39] L. E. Orgel. 929. The effects of crystal fields on the properties of transition-metal ions. *Journal of the Chemical Society (Resumed)*, (0):4756–4761, January 1952. Publisher: The Royal Society of Chemistry.

[40] T. Sakudo and H. Unoki. Dielectric Properties of SrTi${\mathrm{O}}_{3}$ at Low Temperatures. *Physical Review Letters*, 26(14):851–853, April 1971. Publisher: American Physical Society.

[41] R. Bistritzer, G. Khalsa, and A. H. MacDonald. Electronic structure of doped ${d}^{0}$ perovskite semiconductors. *Physical Review B*, 83(11):115114, March 2011. Publisher: American Physical Society.

[42] A. D. Caviglia, S. Gariglio, C. Cancellieri, B. Sacépé, A. Fête, N. Reyren, M. Gabay, A. F. Morpurgo, and J.-M. Triscone. Two-Dimensional Quantum Oscillations of the Conductance at $LaAlO_3$\$/$SrTiO_3$\$ Interfaces. *Physical Review Letters*, 105(23):236802, 2010.

[43] Patrick Irvin, Joshua P. Veazey, Guanglei Cheng, Shicheng Lu, Chung-Wung Bark, Sangwoo Ryu, Chang-Beom Eom, and Jeremy Levy. Anomalous High Mobility in $LaAlO_3$\$/$SrTiO_3$\$ Nanowires. *Nano Letters*, 13(2):364–368, February 2013.

[44] Felix Trier. *Quantum and field effects of oxide heterostructures.* Department of Energy Conversion and Storage, Technical University of Denmark.

[45] P. Schütz, D. V. Christensen, V. Borisov, F. Pfaff, P. Scheiderer, L. Dudy, M. Zapf, J. Gabel, Y. Z. Chen, N. Pryds, V. A. Rogalev, V. N. Strocov, C. Schlueter, T.-L. Lee, H. O. Jeschke, R. Valentí, M. Sing, and R. Claessen. Microscopic origin of the mobility enhancement at a spinel/perovskite oxide heterointerface revealed by photoemission spectroscopy. *Physical Review B*, 96(16):161409, October 2017. Publisher: American Physical Society.

[46] F. Gunkel, S. Hoffmann-Eifert, R. A. Heinen, D. V. Christensen, Y. Z. Chen, N. Pryds, R. Waser, and R. Dittmann. Thermodynamic Ground States of Complex Oxide Heterointerfaces. *ACS Applied Materials & Interfaces*, 9(1):1086–1092, January 2017. Publisher: American Chemical Society.

[47] R.-S. Zhou and Robert L. Snyder. Structures and transformation mechanisms of the , and transition aluminas. *Acta Crystallographica Section B: Structural Science*, 47(5):617–630, 1991.

[48] Dennis Valbjørn Christensen. *Exploring magnetic and electronic properties in -Al2O3/SrTiO3.* Technical University of Denmark, 2018.

[49] Alexey Kalabukhov, Robert Gunnarsson, Johan Börjesson, Eva Olsson, Tord Claeson, and Dag Winkler. Effect of oxygen vacancies in the $SrTiO_3$\$ substrate on the electrical properties of the $LaAlO_3$\$/$SrTiO_3$\$ interface. *Physical Review B*, 75(12):121404, 2007.

[50] Yunzhong Chen, Nini Pryds, Josée E. Kleibeuker, Gertjan Koster, Jirong Sun, Eugen Stamate, Baogen Shen, Guus Rijnders, and Søren Linderoth. Metallic and Insulating Interfaces of Amorphous SrTiO$_3$\$-Based Oxide Heterostructures. *Nano Letters*, 11(9):3774–3778, September 2011.

[51] Naoyuki Nakagawa, Harold Y. Hwang, and David A. Muller. Why some interfaces cannot be sharp. *Nature Materials*, 5(3):204–209, January 2006.

[52] J. R. L. Mardegan, D. V. Christensen, Y. Z. Chen, S. Parchenko, S. R. V. Avula, N. Ortiz-Hernandez, M. Decker, C. Piamonteze, N. Pryds, and U. Staub. Magnetic and electronic properties at the -Al$_2$\$O$_3$\$/SrTiO$_3$\$ interface. *Physical Review B*, 99(13), April 2019.

[53] Joseph Falson, Yusuke Kozuka, Masaki Uchida, Jurgen H. Smet, Taka-hisa Arima, Atsushi Tsukazaki, and Masashi Kawasaki. MgZnO/ZnO heterostructures with electron mobility exceeding 1 × 106 cm2/Vs. *Scientific Reports*, 6(1):26598, May 2016. Number: 1 Publisher: Nature Publishing Group.

[54] Louise Samain, Aleksander Jaworski, Mattias Edén, Danielle M. Ladd, Dong-Kyun Seo, F. Javier Garcia-Garcia, and Ulrich Häussermann. Structural analysis of highly porous -Al2O3. *Journal of Solid State Chemistry*, 217:1–8, September 2014.

[55] D. V. Christensen and A. Smith. Is -Al2O3 polar? *Applied Surface Science*, 423:887–890, November 2017.

[56] Xiang-Hong Chen, Zhi-Xin Hu, Kuang-Hong Gao, and Zhi-Qing Li. High-mobility two-dimensional electron gas in \$\ensuremath{\gamma}\text{\ensuremath{-}}{\mathrm{Al}}_{2}{\mathrm{O}}_{3}/{\mathrm{SrTiO}}_{3}\$ heterostructures. *Physical Review B*, 105(20):205437, May 2022. Publisher: American Physical Society.

[57] Alla Chikina, Dennis V. Christensen, Vladislav Borisov, Marius-Adrian Husanu, Yunzhong Chen, Xiaoqiang Wang, Thorsten Schmitt, Milan Radovic, Naoto Nagaosa, Andrey S. Mishchenko, Roser Valentí, Nini Pryds, and Vladimir N. Strocov. Band-Order Anomaly at the -Al2O3/SrTiO3 Interface Drives the Electron-Mobility Boost. *ACS Nano*, March 2021. Publisher: American Chemical Society.

[58] F. Trier, D. V. Christensen, and N. Pryds. Electron mobility in oxide heterostructures. *Journal of Physics D: Applied Physics*, 51(29):293002, June 2018. Publisher: IOP Publishing.

[59] Steven H. Simon. *The Oxford Solid State Basics*. OUP Oxford, June 2013. Google-Books-ID: lSNoAgAAQBAJ.

[60] P. Schütz, F. Pfaff, P. Scheiderer, Y. Z. Chen, N. Pryds, M. Gorgoi, M. Sing, and R. Claessen. Band bending and alignment at the spinel/perovskite $-Al_2$\$$O_3$\$/SrTiO_3\$ heterointerface. *Physical Review B*, 91(16):165118, 2015.

[61] A. F. Zurhelle, D. V. Christensen, S. Menzel, and F. Gunkel. Dynamics of the spatial separation of electrons and mobile oxygen vacancies in oxide heterostructures. *Physical Review Materials*, 4(10):104604, October 2020. Publisher: American Physical Society.

[62] Dennis Christensen, Felix Trier, M. Soosten, G. Prawiroatmodjo, Thomas Jespersen, Yunzhong Chen, and Nini Pryds. Electric field control of the -Al2O3/SrTiO3 interface conductivity at room temperature. *Applied Physics Letters*, 109:021602, July 2016.

[63] E. Sawaguchi, A. Kikuchi, and Y. Kodera. Dielectric Constant of Strontium Titanate at Low Temperatures. *Journal of the Physical Society of Japan*, 17:1666, October 1962.

[64] Rui Su, Zhaojian Xu, Jiang Wu, Deying Luo, Qin Hu, Wenqiang Yang, Xiaoyu Yang, Ruopeng Zhang, Hongyu Yu, Thomas P. Russell, Qihuang Gong, Wei Zhang, and Rui Zhu. Dielectric screening in perovskite photovoltaics. *Nature Communications*, 12(1):2479, April 2021. Number: 1 Publisher: Nature Publishing Group.

[65] SHINKOSHA - SHINKOSHA Crystals for a bright future. https://www.shinkosha.com/english/.

[66] STEP substratehttps://www.shinkosha.com/english/product/epi_substrate/epi_substrate_10/.

[67] Breakable STO substrate. https://www.shinkosha.com/english/product/epi_substrate/epi_substrate_12.

[68] G. Koster, M. Huijben, and G. Rijnders. 2 - Oxide superlattices by PLD: A practical guide. In Nini Pryds and Vincenzo Esposito, editors, *Metal Oxide-Based Thin Film Structures*, Metal Oxides, pages 27–52. Elsevier, January 2018.

[69] Jorgen Schou, Bo Toftmann, and Salvatore Amoruso. Dynamics of a laser-produced silver plume in an oxygen background gas. 5448:110–120, September 2004. Conference Name: High-Power Laser Ablation V ADS Bibcode: 2004SPIE.5448..110S.

[70] D. Klement, M. Spreitzer, and D. Suvorov. Formation of a strontium buffer layer on Si(001) by pulsed-laser deposition through the Sr/Si(001)(2×3) surface reconstruction. *Applied Physics Letters*, 106(7):071602, February 2015. Publisher: American Institute of Physics.

[71] Alejandro Ojeda-G-P, Max Döbeli, and Thomas Lippert. Influence of Plume Properties on Thin Film Composition in Pulsed Laser Deposition. *Advanced Materials Interfaces*, 5(18):1701062, 2018. _eprint: https://onlinelibrary.wiley.com/doi/pdf/10.1002/admi.201701062.

[72] Angela De Bonis and Roberto Teghil. Ultra-Short Pulsed Laser Deposition of Oxides, Borides and Carbides of Transition Elements. *Coatings*, 10(5):501, May 2020. Number: 5 Publisher: Multidisciplinary Digital Publishing Institute.

[73] S. Amoruso. 6 - Plume characterization in pulsed laser deposition of metal oxide thin films. In Nini Pryds and Vincenzo Esposito, editors, *Metal Oxide-Based Thin Film Structures*, Metal Oxides, pages 133–160. Elsevier, January 2018.

[74] Ernst Meyer, Roland Bennewitz, and Hans J. Hug. Introduction to Scanning Probe Microscopy. In Ernst Meyer, Roland Bennewitz, and Hans J. Hug, editors, *Scanning Probe Microscopy: The Lab on a Tip*, Graduate Texts in Physics, pages 1–12. Springer International Publishing, Cham, 2021.

[75] Ernst Meyer, Roland Bennewitz, and Hans J. Hug. Force Microscopy. In Ernst Meyer, Roland Bennewitz, and Hans J. Hug, editors, *Scanning Probe Microscopy: The Lab on a Tip*, Graduate Texts in Physics, pages 47–107. Springer International Publishing, Cham, 2021.

[76] P. S. Liu and G. F. Chen. Chapter Nine - Characterization Methods: Basic Factors. In P. S. Liu and G. F. Chen, editors, *Porous Materials*, pages 411–492. Butterworth-Heinemann, Boston, January 2014.

[77] Tiago Almeida Silva, Jéssica Santos Stefano, and Bruno Campos Janegitz. Sensing Materials: Nanomaterials. In Roger Narayan, editor, *Encyclopedia of Sensors and Biosensors (First Edition)*, pages 212–230. Elsevier, Oxford, January 2023.

[78] Scanning electron microscope (SEM) | Definition, Images, Uses, Advantages, & Facts | Britannica, April 2023.

[79] Ernst Meyer, Roland Bennewitz, and Hans J. Hug. Introduction to Scanning Tunneling Microscopy. In Ernst Meyer, Roland Bennewitz, and Hans J. Hug, editors, *Scanning Probe Microscopy: The Lab on a Tip*, Graduate Texts in Physics, pages 13–45. Springer International Publishing, Cham, 2021.

[80] Tim Gruene, Julian J. Holstein, Guido H. Clever, and Bernhard Keppler. Establishing electron diffraction in chemical crystallography. *Nature Reviews Chemistry*, 5(9):660–668, September 2021. Number: 9 Publisher: Nature Publishing Group.

[81] M. Becht, F. Wang, J. G. Wen, and T. Morishita. Evolution of the microstructure of oxide thin films. *Journal of Crystal Growth*, 170(1):799–802, January 1997.

[82] Nassim Derriche, Simon Godin, Rysa Greenwood, Alejandro Mercado, and Ashley Nicole Warner. Reflection High-Energy Electron Diffraction.

[83] Shuji Hasegawa. Reflection High-Energy Electron Diffraction. page com139, October 2012. Book Title: Characterization of Materials ISBN: 9780471266969 Place: Hoboken, NJ, USA Publisher: John Wiley & Sons, Inc.

[84] Z. L. Wang. Studies of surface resonance waves in RHEED. *Philosophical Magazine B*, 60(5):617–626, November 1989.

[85] P. Schütz, F. Pfaff, P. Scheiderer, M. Sing, and R. Claessen. Monitoring non-pseudomorphic epitaxial growth of spinel/perovskite oxide heterostructures by reflection high-energy electron diffraction. *Applied Physics Letters*, 106(6):063108, February 2015. Publisher: American Institute of Physics.

[86] Łukasz Kokosza, Jakub Pawlak, Zbigniew Mitura, and Marek Przybylski. Simplified Determination of RHEED Patterns and Its Explanation Shown with the Use of 3D Computer Graphics. *Materials*, 14(11):3056, June 2021.

[87] Dawood Tafti and Christopher V. Maani. X-ray Production. In *StatPearls*. StatPearls Publishing, Treasure Island (FL), 2023.

[88] George F. Harrington and José Santiso. Back-to-Basics tutorial: X-ray diffraction of thin films. *Journal of Electroceramics*, 47(4):141–163, December 2021.

[89] Martin Berger, Qiao Yang, and Andreas Maier. X-ray Imaging. In Andreas Maier, Stefan Steidl, Vincent Christlein, and Joachim Hornegger, editors, *Medical Imaging Systems: An Introductory Guide*. Springer, Cham (CH), 2018.

[90] Younghak Kim, Sangkyun Ryu, and Hyoungjeen Jeen. Strain-effected physical properties of ferromagnetic insulating La 0.88 Sr 0.12 MnO 3 thin films. *RSC Advances*, 9:2645–2649, January 2019.

[91] Neil W. Ashcroft and N. David Mermin. *Solid State Physics*. Cengage Learning, New York, 1st edition edition, January 1976.

[92] P. M. Chaikin and T. C. Lubensky. *Principles of Condensed Matter Physics*. Cambridge University Press, Cambridge, 1995.

[93] H. M. Christen and G. Eres. Recent advances in pulsed-laser deposition of complex oxides. *Journal of Physics: Condensed Matter*, 20(26):264005, June 2008.

[94] D. V. Christensen, Y. Frenkel, Y. Z. Chen, Y. W. Xie, Z. Y. Chen, Y. Hikita, A. Smith, L. Klein, H. Y. Hwang, N. Pryds, and B. Kalisky. Strain-tunable magnetism at oxide domain walls. *Nature Physics*, 15:269–274, 2019.